

Quantum-dense metrology for subtraction of back-scatter disturbances in gravitational-wave detection

Von der QUEST-Leibniz-Forschungsschule
der Gottfried Wilhelm Leibniz Universität Hannover
zur Erlangung des Grades

DOKTOR DER NATURWISSENSCHAFTEN
Dr. rer. nat.

genehmigte Dissertation
von

Dipl.-Phys. Melanie Ast

geboren am 14. Januar 1985 in Wittmund

2017

Referent	Prof. Dr. rer. nat. Roman Schnabel Institut für Laserphysik und Zentrum für Optische Quantentechnologien Universität Hamburg
Korreferent	Prof. Dr. rer. nat. Karsten Danzmann Albert-Einstein-Institut, AEI Hannover: Max-Planck-Institut für Gravitationsphysik und Institut für Gravitationsphysik der Leibniz Universität Hannover
Tag der Disputation	13. Januar 2017

Kurzfassung

In interferometrischen Gravitationswellen (GW)-Detektoren werden hohe Laserleistungen von bis zu 100 kW verwendet um differentielle Armlängenänderungen in der Größenordnung von $10^{-20} \text{ m}/\sqrt{\text{Hz}}$ zu messen. Aufgrund der hohen Laserleistung ist Streulicht in den Detektoren unvermeidbar. Kleinste ungewollte Reflexionen (wenige zurückgestreute Photonen pro Sekunde) können die Sensitivität des Detektors beeinträchtigen wenn sie von vibrierenden Oberflächen in der Umgebung in die Interferometer Mode zurückgestreut werden. Um dies zu verhindern gibt es zwei wesentliche Ansätze (i) das Streulicht durch Verwendung von Optiken mit hoher Oberflächenqualität und Installation von Strahlfallen zu minimieren und (ii) die Isolation potenzieller Quellen für Rückstreuung von der Umgebung, um ihre Bewegung zu verringern.

In dieser Arbeit schlage ich ein neues Verfahren vor, um Streulicht induzierte Störungen in GW-Detektoren zu reduzieren. Das Verfahren ergänzt die bisherigen Ansätze und beruht auf der Modellierung und Subtraktion eines Streulichtstörsignals in der Datenbearbeitung. Ein zusätzliches Auslesen der Phasenquadratur des Ausgangsfeldes eines Interferometers liefert einen Referenzkanal für Streulicht induzierte Störungen der keine Signale aus differentiellen Armlängenänderungen enthält. In dem hier vorgeschlagenen Verfahren wird dieser Kanal zur Modellierung von Streulichtstörsignalen verwendet. Die Projektion des Streulichtstörsignals in der wissenschaftlich relevanten Amplitudenmessung wird bestimmt und von den Messdaten abgezogen um die Sensitivität der Messung zu verbessern. Das Verfahren wurde im Verlauf dieser Arbeit in einem Tischexperiment demonstriert.

Eine weitere wichtige Rauschquelle in GW-Detektoren ist das Quanten-Schrotrauschen, welches heutige fortgeschrittene GW-Detektoren im hohen Frequenzbereich ($\gtrsim 150 \text{ Hz}$) limitiert. Wie im GEO 600 Detektor demonstriert wurde, kann die Sensitivität in diesem Bereich durch die Verwendung von gequetschtem Licht verbessert werden. Diese relativ neue Technik hat sich bewährt und ist fester Bestandteil der geplanten Aufrüstung der gegenwärtigen Detektorgeneration und von Vorschlägen für zukünftige Detektoren wie z.B. das Einstein Teleskop (ET).

Im zweiten Teil meiner Arbeit demonstriere ich, dass das vorgeschlagene Verfahren zur Reduzierung von Streulichtstörsignalen vollständig kompatibel mit der Sensitivitätssteigerung eines Interferometers durch gequetschtes Licht ist. Um das gleichzeitige Auslesen beider Quadraturen unter dem Quanten-Schrotrauschen zu ermöglichen, und damit das Regime einer *quantendichten Messung* zu erreichen, werden zwei-Moden-gequetschte Zustände benötigt. Durch das Abziehen eines Streulichtstörsignals wird die Sensitivität einer Messung unterhalb des Quanten-Schrotrauschens erreicht, obwohl die Messung ursprünglich durch starkes klassisches Rauschen limitiert wurde.

Schlüsselbegriffe: Gravitationswellen-Detektion, gequetschtes Licht, Streulicht, zwei-Moden-gequetschtes Licht, quantendichte Messung

Abstract

Gravitational-wave detectors employ high laser powers of up to 100 kW in advanced Michelson interferometer topologies to sense differential arm length changes with strain sensitivities in the order of $10^{-23}/\sqrt{\text{Hz}}$. With such high light powers, stray light in the detectors is inevitable. Small unintended reflections can cause severe problems if they are back-scattered into the interferometer mode from moving surfaces in the environment. Just a few back-scattered photons per second produce measurable disturbances in the gravitational-wave strain channel. Standard mitigation techniques against back-scattering are (i) to reduce the amount of stray light by employing high surface quality optics and the installation of beam dumps and baffles in the setup and (ii) the isolation of potential back-scatter sources from the environment to reduce their motion.

In this work, I propose and demonstrate a new approach for the mitigation of back-scatter disturbances which is complementary to the existing mitigation techniques. The approach is based on the subtraction of disturbances in data post-processing and relies on the existence of a mathematical model for the back-scatter disturbance. In a proof of principle setup, I employ a split interferometer readout with balanced homodyne detection to achieve an additional readout of the orthogonal phase quadrature of the interferometer output field. The phase quadrature does not contain any strain information but provides a reference channel for back-scatter disturbances. The additional information from the phase quadrature measurement is used to fit an analytical model to the disturbance signal. From this model, the projection of the disturbance into the ‘scientific’ amplitude measurement is inferred and subtracted from the data to improve the sensitivity of the measurement.

Another important noise source in gravitational-wave detectors is quantum noise. Current advanced detectors are limited by quantum shot noise in the high frequency regime above about 150 Hz. As first demonstrated in the GEO 600 detector, the sensitivity in this regime can be further increased using squeezed states of light. This relatively novel technique has proven its use and is an inherent part of future upgrades and proposals for next generation gravitational-wave observatories such as the Einstein Telescope (ET).

In the second part of my work, I demonstrate that the proposed (back-scatter mitigation) concept is fully compatible with a squeezed light enhancement of an interferometer. Two-mode-squeezed states of light are required to enable simultaneous sub-shot-noise performance in both quadrature readouts, thereby entering the regime of *quantum-dense metrology*. Through the subtraction of a back-scatter disturbance, sub-shot-noise sensitivity is achieved in a measurement which was previously limited by strong classical excess noise.

Key words: Gravitational-wave detection, squeezed light, scattered light, two-mode-squeezing, quantum-dense metrology

Contents

1. Introduction	1
1.1. Gravitational-wave detection	1
1.2. Quantum noise and squeezed light enhancement	2
1.3. Scattered light in gravitational-wave detectors	5
1.4. Scope of the thesis	6
2. Basic quantum optics	9
2.1. Coherent states	9
2.2. Quadrature operators and the phasor picture	11
2.3. Squeezed states of light	13
2.4. Balanced homodyne detection	15
2.5. Two-mode-squeezing	16
3. Back-scatter disturbances and the approach for their subtraction	19
3.1. Distinguishing back-scatter disturbances from GW signals	19
3.2. Modeling back-scatter disturbances for their subtraction	21
3.2.1. The case of small amplitude motion	22
3.2.2. A broadband scatter shoulder from frequency up-conversion	22
3.3. Proof of principle setup	25
4. Quantum-dense metrology	27
4.1. The quantum-dense readout	27
4.2. Considering optical loss in quantum-dense metrology	29
5. Main parts of the experimental setup	32
5.1. Michelson interferometer with dual homodyne readout	33
5.2. Source for the two-mode-squeezed states	35
5.3. Quantum-dense readout	37
5.4. Data acquisition	39
6. Experimental demonstration of a dual homodyne readout for subtraction of back-scatter disturbances	43
6.1. Scatter sources with small amplitude motion	44
6.1.1. Experimental generation of the test signals	44
6.1.2. Stabilization of the dual homodyne readout	45
6.1.3. Post-processing	46
6.1.4. Subtraction of the scatter disturbance	48

6.1.5. Discussion	50
6.2. Broadband scatter shoulder	51
6.2.1. Experimental generation of the test signals	51
6.2.2. Stabilization of the dual homodyne readout	53
6.2.3. Post-processing of the scatter limited measurement data	54
6.2.4. Subtraction of the scatter disturbance	59
6.2.5. Discussion	61
6.3. Scatter shoulder with multiple round trips	62
6.3.1. Experimental generation of the test signals	63
6.3.2. Scatter limited measurement data	64
6.3.3. Modeling and post-processing	67
6.3.4. Subtraction of the scatter disturbance	71
6.3.5. Discussion	74
7. Application of quantum-dense metrology for subtraction of a back-scatter shoulder	75
7.1. Experimental setup	75
7.2. Measurement and post-processing	76
7.3. Subtraction of the scatter disturbance	78
7.4. Discussion	80
8. Summary and conclusion	83
Appendices	85
A. LabView program	87
B. Matlab scripts	91
C. Cancellation of lateral displacement noise of three-port gratings for coupling light to cavities	109
C.1. Introduction	109
C.2. Experimental setup	110
C.3. Measurement results	113
C.4. Conclusion	113
Bibliography	115
Acknowledgments	121
Utilized Resources	124
Curriculum Vitae	126
List of Publications	128

List of Figures

1.1. Schematic of a gravitational-wave detector	2
1.2. Quantum noise in a gravitational-wave detector.	4
1.3. Scattered light in gravitational-wave detectors	5
2.1. Phasor representation of a coherent state	12
2.2. The phasor picture	13
2.3. Squeezed fields	14
2.4. Balanced homodyne detector	15
2.5. Generation of two-mode-squeezed states	16
3.1. GW signal and scatter disturbance in the phasor picture	20
3.2. A scatter shoulder from frequency up-conversion	24
3.3. Dual readout for subtraction of back-scatter disturbances	25
4.1. Split single quadrature squeezed readout	27
4.2. Schematic setup for quantum-dense metrology	28
4.3. Comparison of QDM with a single quadrature squeezed readout	30
4.4. Optimal input squeezing in QDM	31
5.1. Schematic of the overall experimental setup	32
5.2. Photo of the table-top Michelson interferometer with dual homodyne readout	33
5.3. Photo of the two-mode-squeezed light source	35
5.4. Photo of the table-top Michelson interferometer with quantum-dense readout	38
5.5. Schematic of the locking procedure for the quantum-dense readout	39
5.6. Schematic sequence of data acquisition and processing	39
5.7. Performance of the data acquisition	40
6.1. Schematic of the experimental setup	43
6.2. Experimental generation of the test signals	44
6.3. Locking scheme for the dual homodyne readout	45
6.4. Analyzing the scatter disturbance in the phase quadrature data of BHD1	47
6.5. Subtraction of the scatter disturbance – simple peak	48
6.6. Subtraction of the scatter disturbance – peak with surrounding sideband structure	49
6.7. Experimental generation of the test signals	51

6.8. Injected GW signal	52
6.9. Locking scheme for the dual homodyne readout	53
6.10. Scatter limited data	54
6.11. Fitting the Doppler shift of the back-scattered light	56
6.12. Fitting the phase quadrature data	57
6.13. Projection of the scatter model in the amplitude quadrature	59
6.14. Results after subtraction of the scatter model	60
6.15. Experimental generation of the test signals	62
6.16. Scatter cavity in transmission	63
6.17. Scatter limited measurements for the 2 Hz disturbance	65
6.18. Scatter limited measurements for the 10 Hz disturbance	66
6.19. Cavity round trips	67
6.20. Projection of the scatter disturbance in the phase quadrature	69
6.21. Projection of the scatter disturbance in the amplitude quadrature	70
6.22. Results after subtraction of the scatter model for the 2 Hz disturbance	72
6.23. Results after subtraction of the scatter model for the 10 Hz disturbance	73
7.1. Setup for the quantum-dense interferometer readout	76
7.2. Quantum-dense measurement with back-scatter disturbance	77
7.3. Time domain data with fitted scatter model	78
7.4. Sensitivity improvement via quantum-dense metrology with data post-processing	79
A.1. LabView user interface	87
A.2. LabView block diagram part 1	88
A.3. LabView block diagram part 2	89
C.1. Michelson interferometers with arm resonators	110
C.2. Experimental setup	111
C.3. Individual diffraction orders	112
C.4. Combination of the $\pm 1^{\text{st}}$ diffraction orders	113

1. Introduction

In this thesis I present a new concept to improve the sensitivity of gravitational-wave (GW) detectors, employing a quantum-dense readout scheme. This Introduction gives a short overview on GW detection in general and describes two special noise sources in GW detectors which are targeted by the new scheme: quantum noise in the form of optical shot noise and stray light induced disturbances. The last section introduces the scope and structure of this thesis.

1.1. Gravitational-wave detection

In his revolutionary theory of general relativity (GR) Einstein introduced a completely new view on the gravitational force [1]. In his theory, gravity manifests as a property of space-time itself, namely its curvature. The basic idea of Einsteins theory was summarized by Wheeler with the following sentence: “*Matter tells space-time how to curve; space-time tells matter how to move.*” [2].

Gravitational waves were first predicted by Einstein in 1916 [3, 4]. They constitute a special solution of his field equations in the linearized, weak-field regime. Gravitational waves are quadrupole waves which describe periodic length changes, orthogonal to their direction of propagation. They are produced by accelerated masses, i.e. changes in the mass quadrupole moment of a source, and propagate at the speed of light. However, space-time is ‘stiff’, and only massive objects with high accelerations from cosmic events can produce measurable length changes on Earth. Since the interaction of gravitational waves with matter is extremely weak, they propagate through space nearly unattenuated. On one hand, this is advantageous because the information about the gravitational-wave source is nearly undisturbed. On the other hand, it makes their direct detection extremely challenging. Performing astronomy with gravitational waves opens up a completely new window into the universe, as previously almost all our information about cosmic events came to us through electromagnetic radiation.

The first indirect proof for the existence of gravitational waves was initiated by Hulse and Taylor through their discovery of a binary pulsar system [5]. Further analysis by Taylor and Weisberg showed that the system lost rotational energy in a manner consistent with energy loss through the radiation of gravitational waves as predicted by GR [6].

A century after the prediction of gravitational waves, their first direct detection was achieved by the advanced LIGO detectors in 2015 [7]. They observed the inspiral and merger of a binary black hole system, the first time such a system was detected.

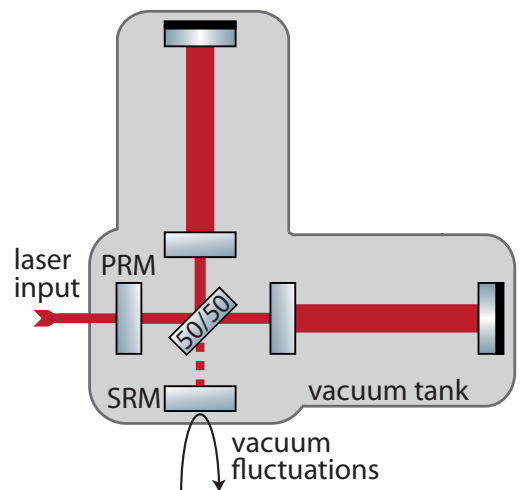
The advanced LIGO detectors are part of a global network of interferometric gravitational-wave detectors [8–11]. All of these detectors employ advanced Michelson interferometer topologies to measure tiny changes in the differential arm length. When a gravitational wave passes the detector, it periodically changes the lengths of the two detector arms. This produces a phase modulation of the light in each of the interferometer arms, which is exactly out of phase with respect to each other. By recombination of the laser light at the interferometer beam splitter, this phase modulation is turned into an amplitude modulation of the residual light in the interferometer output port which is then detected. The currently operating detectors reach relative strain sensitivities in the order of $10^{-23}/\sqrt{\text{Hz}}$ in a broad frequency range from about 30 Hz up to 2 kHz [12].

1.2. Quantum noise and squeezed light enhancement

When current GW detectors reach their design sensitivities, they will be close to being completely quantum noise limited [8]. Already, their sensitivity is limited by quantum shot noise above frequencies of about 150 Hz [12].

Quantum noise has its origin in the zero point fluctuations of the electromagnetic field and contributes to the detector noise in two different ways. A schematic of the typical advanced detector topology is depicted in Figure 1.1. As GW detectors are operated at, or at least close to, a dark fringe, all noise entering the interferometer from the laser input side is back-reflected towards the laser source. The interferometer acts as a highly-reflective mirror in this case. The quantum noise that couples into a measurement at the interferometer output can be attributed to the vacuum fluctuations which enter the interferometer through its dark port [13]. Inside the interferometer arms the vacuum fluctuations beat with the high power interferometer beam and lead to phase and amplitude fluctuations of the interferometer field. When the light returns from the end mirrors, the phase fluctuations of the field constructively interfere at the interferometer beam splitter and lead to amplitude fluctuations of the residual interferometer output light. The resulting statistical fluctuation of the output power is referred to as *quantum*

Figure 1.1: Schematic of a gravitational-wave detector. The schematic shows the typical advanced gravitational-wave detector topology with power recycling, signal recycling and arm cavities enclosed in a vacuum tank. Vacuum fluctuations enter the interferometer through its dark output port and contribute to the interferometer’s strain sensitivity through quantum shot noise and radiation pressure noise. PRM: power recycling mirror, SRM: signal recycling mirror.



shot noise.

Considering a simple Michelson interferometer without any additional cavities, the shot noise (SN) is frequency independent (white) noise which contributes to the linear strain sensitivity via [14]

$$h_{\text{SN}} = \frac{1}{L} \sqrt{\frac{\hbar c \lambda}{4\pi P}}. \quad (1.1)$$

Here, λ denotes the laser wavelength, L denotes the arm length of the interferometer and P denotes the circulating light power. The shot noise contribution for two different powers is depicted by the dashed lines in Figure 1.2. The parameters used for this plot are those of the advanced LIGO interferometers: $\lambda = 1064$ nm, $L = 4$ km, $m = 40$ kg and $P = 100$ kW. The shot noise scales with $1/\sqrt{P}$ which means that an increase in power lowers the relative shot noise contribution.

The second way in which quantum noise couples into the interferometric measurements is through *quantum radiation pressure noise* (RPN). The amplitude fluctuations of the interferometer field cause a statistical momentum transfer from the laser beam to the interferometer end mirrors of mass M . This in turn produces a statistical phase shift for the reflected light and therefore an additional amplitude fluctuation at the interferometer output. The amplitude fluctuations hitting the mirrors are white in frequency but the transfer function of the mirrors is that of a harmonic oscillator. Above its resonance frequency this results in a frequency dependent contribution of [14]

$$h_{\text{RPN}}(f) = \frac{1}{m f^2 L} \sqrt{\frac{\hbar P}{\pi^3 c \lambda}} \quad (1.2)$$

for the linear strain sensitivity of the interferometer. Here, $m = M/2$ denotes the reduced mass of the mirrors. The contribution of radiation pressure noise is depicted by the dotted lines in Figure 1.2. It scales with \sqrt{P} and falls off with $1/f^2$ due to the transfer functions of the suspended mirrors.

The overall quantum noise is given by the uncorrelated sum of the two contributions

$$h_{\text{QN}}(f) = \sqrt{h_{\text{SN}}^2(f) + h_{\text{RPN}}^2(f)} \quad (1.3)$$

and is shown by the solid red and blue lines in Figure 1.2. The shot noise dominates the high frequency regime and the radiation pressure noise is dominant at lower frequencies. For each frequency there is an optimal power where both contributions are of the same size. Combining these points leads to the so-called *standard quantum limit* (SQL) given in black [14]

$$h_{\text{SQL}}(f) = \frac{1}{\pi f L} \sqrt{\frac{\hbar}{m}}. \quad (1.4)$$

The sensitivity of currently operating gravitational-wave detectors is not yet limited by radiation pressure noise as other technical noise sources are still dominant in the low frequency regime [15]. An increase in light power is therefore still beneficial, in fact, the advanced detectors have not yet reached their design input power. Operating at such

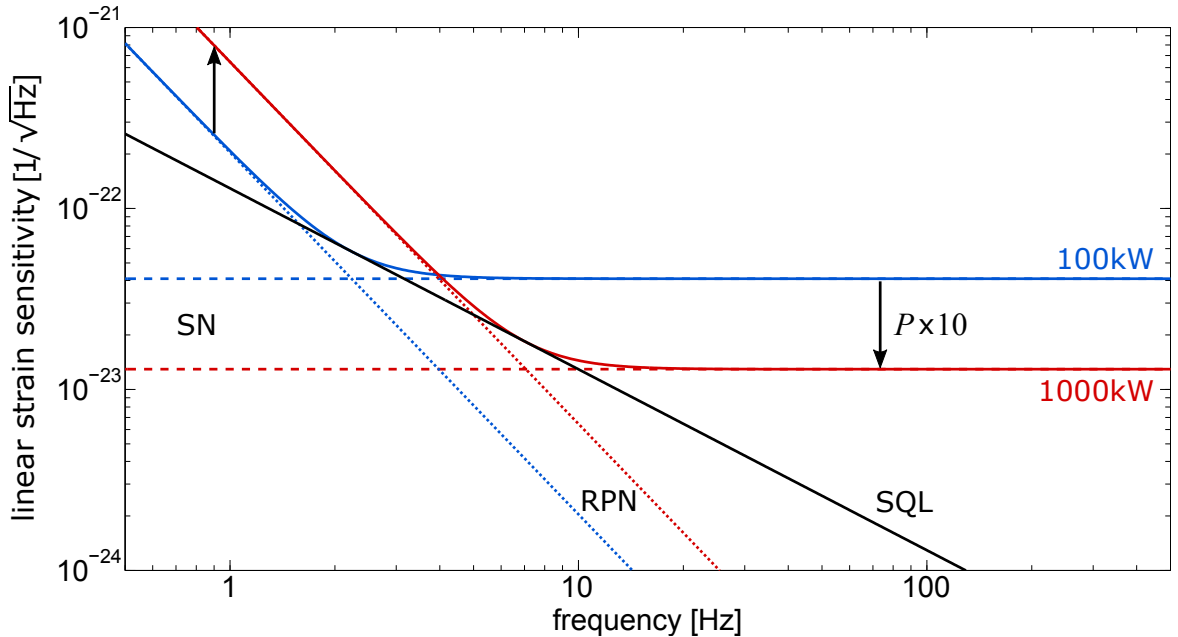


Figure 1.2.: Quantum noise in a gravitational-wave detector. The plot shows the shot noise (SN, dashed), radiation pressure noise (RPN, dotted) and the overall quantum noise contribution (solid) to the linear strain sensitivity of a Michelson interferometer for two different light powers. The parameters used here are those of the advanced LIGO detectors: $\lambda = 1064$ nm, $L = 4$ km, $m = 40$ kg and $P = 100$ kW. The resulting standard quantum limit (SQL) is shown in black.

high light powers is challenging and introduces problems, for example, thermal lensing in the substrates of transmissive optics or increased stray light in the detector.

An alternative approach for lowering the quantum shot noise in a GW detector was proposed by Caves in the early 1980's [16]. The vacuum state entering the interferometer dark port can be replaced by a so-called *squeezed state*. These states possess reduced (*squeezed*) quantum fluctuations in either their amplitude or their phase quadrature, at the cost of increased (*anti-squeezed*) fluctuations in the respective other quantity. Such states will be described in more detail in Section 2.3. The injection of a 10 dB squeezed state, which is aligned to decrease the phase fluctuations of the interferometer field, has the same effect on the interferometer's strain sensitivity as a tenfold increase in light power.

The application of squeezed states of light in a gravitational-wave detector was first demonstrated in the GEO 600 detector [17]. Stable long-term operation with a sensitivity improvement below the quantum shot noise was achieved in the frequency regime above ≈ 400 Hz [18]. Squeezing enhancement has also been successfully tested in the short term in the advanced LIGO detector in Hanford [19]. The technique has been intensively investigated and is intended as one of the next major upgrades for the advanced LIGO detectors [20, 21]. Squeezed light enhancement is also an inherent part of proposals for third generation GW observatories such as the Einstein Telescope (ET) [22].

1.3. Scattered light in gravitational-wave detectors

Scattered light is a longstanding problem in interferometric gravitational-wave detectors. The issue was already discovered in the first prototypes [23], and disturbances from back-scattered light were observed in all first generation detectors [24]. An overview of this topic is given in [25]. A possible scenario for the generation of such disturbances is schematically depicted in Figure 1.3. The typical detector topology is shown, with power recycling, signal recycling and arm cavities, enclosed in a vacuum tank. Light can be scattered out of the main interferometer beam, for example, due to micro roughness of mirror surfaces or imperfect anti-reflection coatings of transmissive optics. If such light interacts with vibrating surfaces in the environment, such as the walls of the vacuum tank, and is then back-scattered into the interferometer mode, it produced a spurious signal at the interferometer output. This spurious signal can not be distinguished from a signal generated by a differential arm length change with the *DC-readout* that is currently used.

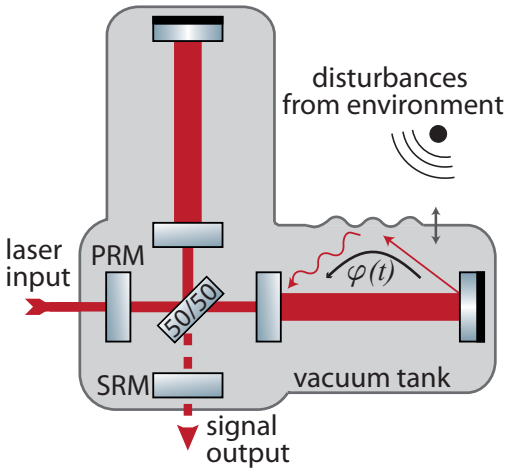


Figure 1.3: Scattered light in gravitational-wave detectors. The schematic shows the typical advanced gravitational-wave detector topology with power recycling, signal recycling and arm cavities, enclosed in a vacuum tank. Light is scattered out of the interferometer mode and becomes phase modulated by interaction with vibrating surfaces in the environment. Back-scattering into the interferometer mode produces a disturbance signal at the interferometer output.

There are two different types of back-scatter disturbances which play a role in gravitational-wave detectors [26]. Sources with small amplitude motion (much smaller than the laser wavelength) can produce disturbance signals if they move at frequencies that lie directly in the detectors sensitive band. The disturbance signal is then produced at the same frequency as the motion of the source. The second type originates from back-scatter sources with large amplitude motion of several wavelengths which typically move at much lower frequencies. In this case, fringe wrapping leads to frequency up-conversion and can produce very broadband disturbances, so-called ‘scatter shoulders’ or ‘scattering shelves’, which spoil the detectors sensitivity in the most interesting (low) frequency band.

The main approach for mitigation against back-scattering is of course to reduce the amount of stray light as far as possible. Optics with high surface qualities are employed and numerous beam dumps and baffles have been installed in the detectors to catch unintended reflections. Another mitigation technique is to reduce the motion of potential scatter sources by isolating them from the environment or actively damping their motion

to prevent any nonlinear coupling. An overview of these mitigation techniques can be found in [25]. A different approach for avoiding back-scatter disturbances from external optical benches was demonstrated in GEO 600 [27, 28]. Here, an optical phase shifter was applied to shift the frequency of the external beam, and therefore also the frequency of the back-scattered beam, out of the detectors sensitive band. A noise reduction of one order of magnitude was achieved with this technique.

Despite these extensive provisions, back-scatter disturbances have been a recurring issue in gravitational-wave detectors. For example, scattering shelves were observed in Virgo’s second science run during times with intense micro-seismic activity [29]. Here, light was back-scattered from an optical bench behind one of the interferometer end mirrors (WEB). These external benches are critical elements since they can directly back-scatter into the interferometer mode with only one scattering process. Back-scattering from such sources has been investigated in reference [30], for example. Also in advanced LIGO, increased noise was observed for frequencies below 20 Hz during high micro-seismic motion. Those disturbances originated from frequency up-conversion of back-scattered light from the output mode cleaner [15, 31].

With a future increase of the light power in GW detectors, the amount of stray light will also increase. Investigations showed that significantly improved mitigation schemes against back-scattered light will be required to extend the sensitive band of third generation GW detectors towards lower frequencies (< 10 Hz) [26].

1.4. Scope of the thesis

In the work presented here, I propose and demonstrate a new approach for the mitigation of back-scatter disturbances. This approach is concerned with the subtraction of back-scatter disturbances in data post-processing and is complementary to the existing mitigation techniques described in the last section.

The concept proposed here relies on the existence of an analytical model that describes the scatter disturbance. Through an additional readout of the phase quadrature of the interferometer signal, a GW signal free reference channel is obtained which contains information about the back-scatter disturbance. The additional information from the phase quadrature was already employed to identify back-scatter disturbances and discard corrupted measurement data (*vetoing*) [32, 33]. Here, this monitor for scatter disturbances is used to fit an analytical model to the disturbance signal. From the model, the projection of the disturbance into the ‘scientific’ amplitude measurement is inferred and subtracted from the amplitude quadrature data. This leads to an actual sensitivity improvement of the measurement. The approach is described in more detail in Chapter 3.

When applying this concept to gravitational wave detectors, an alternative to the existing DC-readout scheme is required in order to allow the additional phase quadrature measurement. In this work, I propose a split interferometer output with balanced homodyne readout as described in Section 3.3, this is denoted as *dual (homodyne) readout* throughout this thesis. A short description of balanced homodyne detection is given in

Section 2.4.

As squeezed light enhancement will be an inherent part of future gravitational-wave detection, it is important that a new readout scheme is compatible. A *quantum-dense readout* of a split interferometer output was shown to fulfill this requirement [33–35]. The readout relies on the application of so-called ‘two-mode-squeezed’ states of light. Chapter 2 introduces the basic background in quantum optics necessary for understanding squeezing and describes the relevant properties of the two-mode-squeezed states. *Quantum-dense metrology* is reviewed in Chapter 4, and an analysis of the scheme with consideration of optical loss in the interferometer is given in Section 4.2.

I performed several experiments to demonstrate the subtraction of back-scatter disturbances for different types of scatter sources, as well as the sub-shot noise enhancement of the readout in a proof of principle setup. The main parts of the experimental setup are described in Chapter 5. Chapter 6 summarizes the experiments which were carried out without the enhancement through two-mode-squeezed states and presents the results for the subtraction of the different back-scatter disturbances. The experiment described in Chapter 7 employed the quantum-dense readout for the subtraction of a broadband scatter shoulder. A sensitivity improvement of the scattered light limited measurement below the quantum shot noise was demonstrated. A nonclassical noise suppression of about 5 dB in both quadrature readouts was achieved over the whole measured spectrum.

A summary of my work and a conclusion can be found in Chapter 8. The LabView program and some key Matlab scripts I used in this work are given in Appendices A and B. In addition to my work on the subtraction of back-scatter disturbances, I performed an experiment on the cancellation of lateral displacement noise for 3-port gratings. The results of this experiment were published in *Optics Letters* [36] and the paper is included in Appendix C.

2. Basic quantum optics

This chapter provides the quantum mechanical background for the two-mode-squeezed states that were used in this work to achieve sub-shot-noise sensitivity in the interferometer readout. I will introduce the coherent states, the quadrature operators and the phasor picture which can be used to describe the electromagnetic field and the effect of squeezing. I will also briefly describe the principle of balanced homodyne detectors which were used throughout this work to perform the measurements of the amplitude and phase quadratures of the interferometer output field. The descriptions in this chapter are based on the treatment by Gerry and Knight [37].

2.1. Coherent states

In quantum optics, coherent states are used to describe the classical oscillatory behavior of the electromagnetic (EM) field, for example, of a single mode (monochromatic) laser beam as it is used in the experiments of this work. They can be derived by specifically searching for quantum mechanical states for which the expectation value of the electric field operator takes the form of the classical fields. The description of a single mode field is formally equivalent to the description of a harmonic oscillator where the electric and magnetic field amplitudes (\hat{q} and \hat{p}) play the roles of the canonical position and momentum. The corresponding Hamiltonian is given by

$$\hat{H} = \frac{1}{2} (\hat{p}^2 + \omega^2 \hat{q}^2) \quad (2.1)$$

and describes the energy contained in a single mode of the field at an angular frequency ω . For further descriptions it is useful to introduce the *annihilation* \hat{a} and *creation* \hat{a}^\dagger operators of the harmonic oscillator

$$\begin{aligned} \hat{a} &= \frac{1}{\sqrt{2\hbar\omega}} (\omega\hat{q} + i\hat{p}) \\ \hat{a}^\dagger &= \frac{1}{\sqrt{2\hbar\omega}} (\omega\hat{q} - i\hat{p}) \end{aligned} \quad (2.2)$$

with the commutator $[\hat{a}, \hat{a}^\dagger] = 1$. The time dependency of an arbitrary, not explicitly time dependent operator \hat{O} is determined by Heisenberg's equation

$$\frac{d\hat{O}}{dt} = \frac{i}{\hbar} [\hat{H}, \hat{O}] . \quad (2.3)$$

For the annihilation and creation operators follows

$$\begin{aligned}\hat{a}(t) &= \hat{a}(0) e^{-i\omega t} \\ \hat{a}^\dagger(t) &= \hat{a}^\dagger(0) e^{i\omega t} .\end{aligned}\tag{2.4}$$

With these operators the Hamiltonian can be rewritten as

$$\hat{H} = \hbar\omega \left(\hat{a}^\dagger \hat{a} + \frac{1}{2} \right) .\tag{2.5}$$

The term $\hat{a}^\dagger \hat{a}$ is called the *number operator* \hat{n} and can be associated with the number of photons with energy $\hbar\omega$ in the mode.

The electric field operator can also be expressed in terms of the annihilation and creation operators. For a single mode field at a frequency ω which propagates along the z-axis and is linearly polarized perpendicular to this axis it is given by

$$\hat{E} = \frac{i}{2} E_0 \left(\hat{a} e^{-ikz} - \hat{a}^\dagger e^{ikz} \right) \quad \text{with} \quad E_0 = \left(\frac{\hbar\omega}{\epsilon_0 V} \right)^{\frac{1}{2}} .\tag{2.6}$$

Here, $k = \frac{\omega}{c}$ denotes the wave number, ϵ_0 is the vacuum permittivity and V denotes the effective volume in which the field is enclosed. From Equation (2.6) it is obvious that the expectation value of the electric field operator describes a classical field for the eigenstates of the annihilation operator. These are called the *coherent states* which are commonly denoted

$$\hat{a} |\alpha\rangle = \alpha |\alpha\rangle \quad \text{with} \quad \alpha = |\alpha| e^{-i\varphi} .\tag{2.7}$$

The eigenvalues of these states are allowed to be complex since \hat{a} is not a Hermitian operator, i.e. $[\hat{a} \neq \hat{a}^\dagger]$. The ground state is given for $|\alpha=0\rangle$ and is called *vacuum state*. For the coherent states, the expectation value of the electric field operator takes the form

$$\langle \hat{E} \rangle = \frac{i}{2} E_0 \left(|\alpha| e^{-i(kz+\omega t+\varphi)} - |\alpha| e^{i(kz+\omega t+\varphi)} \right)\tag{2.8}$$

$$= E_0 |\alpha| \sin(kz + \omega t + \varphi)\tag{2.9}$$

which clearly describes the classical oscillatory behavior. Hereby, E_0 can be associated with the electric field ‘per photon’ and α describes the *coherent excitation*. In contrast to the classical description, the electric field possesses an uncertainty which can be quantified by the variance of the field operator for a coherent state

$$\Delta^2 \hat{E} = \langle \hat{E}^2 \rangle - \langle \hat{E} \rangle^2 = \frac{1}{2} E_0^2 .\tag{2.10}$$

The uncertainty is independent of the coherent excitation α and is therefore the same for all coherent states, even for the vacuum state. This uncertainty of the ground state corresponds to the so-called *vacuum fluctuations* of the field.

The power of the field, as measured by a photo detector, is proportional to the mean number of photons in the mode, i.e. to the expectation value of the number operator

$$\langle \hat{n} \rangle \equiv \langle \hat{a}^\dagger \hat{a} \rangle = |\alpha|^2 \equiv \bar{n} \quad \text{with variance} \quad \Delta^2 \hat{n} = \bar{n} .\tag{2.11}$$

Comparing the fluctuation of the photon number with its mean value yields the fractional uncertainty

$$\frac{\Delta \hat{n}}{\bar{n}} = \frac{1}{\sqrt{\bar{n}}} \quad (2.12)$$

which decreases with increasing \bar{n} . This means that for large photon numbers the relative uncertainty becomes smaller and smaller, approaching the classical scenario where the field is exactly defined.

2.2. Quadrature operators and the phasor picture

For further considerations, it is useful to introduce the so-called *quadrature operators*

$$\begin{aligned} \hat{X} &= \frac{1}{2} (\hat{a} + \hat{a}^\dagger) \\ \hat{P} &= \frac{1}{2i} (\hat{a} - \hat{a}^\dagger) \end{aligned} \quad (2.13)$$

and with $\hat{a} \equiv \hat{a}(0)$ and $\hat{a}^\dagger \equiv \hat{a}^\dagger(0)$, to describe the EM field. They are dimensionless operators and their commutator is given by $[\hat{X}, \hat{P}] = \frac{i}{2}$. In the literature, these operators are also commonly denoted with \hat{X}_1 and \hat{X}_2 or \hat{X} and \hat{Y} . In terms of the quadrature operators, the electric field operator can be expressed as

$$\hat{E}_x = 2E_0 \sin(kz) \left(\hat{X} \cos(\omega t) + \hat{P} \sin(\omega t) \right) . \quad (2.14)$$

\hat{X} and \hat{P} are Hermitian operators and therefore correspond to measurable quantities. They can be associated with the field's *amplitude quadrature* and *phase quadrature*. Their expectation values for a coherent state correspond to the real and imaginary parts of the coherent excitation α

$$\begin{aligned} \langle \hat{X} \rangle &= \text{Re}(\alpha) \\ \langle \hat{P} \rangle &= \text{Im}(\alpha) . \end{aligned} \quad (2.15)$$

According to Heisenberg's uncertainty relation for two arbitrary operators \hat{A} and \hat{B}

$$\Delta^2 \hat{A} \cdot \Delta^2 \hat{B} \geq \frac{1}{4} \left\langle i [\hat{A}, \hat{B}] \right\rangle^2 \quad (2.16)$$

the variances of the two quadratures have to obey

$$\Delta^2 \hat{X} \cdot \Delta^2 \hat{P} \geq \frac{1}{16} . \quad (2.17)$$

For a coherent state their variances are given by

$$\Delta^2 \hat{X} = \Delta^2 \hat{P} = \frac{1}{4} . \quad (2.18)$$

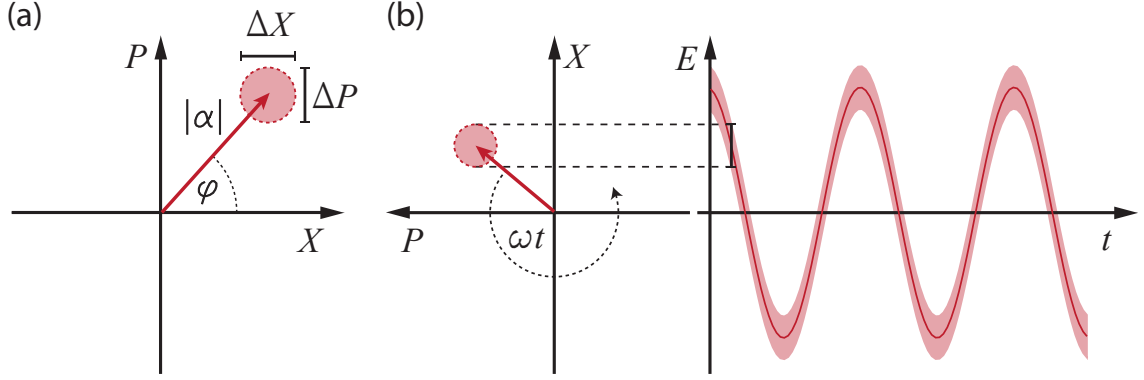


Figure 2.1.: Phasor representation of a coherent state. (a) A coherent state with excitation $\alpha = |\alpha|e^{i\varphi}$ can be represented in (co-rotating) quadrature space by an arrow or *phasor* of length $|\alpha|$ at an angle of φ to the X -axis. The inherent uncertainty of the coherent state is depicted by a circle whose diameter is given by the standard deviations $\Delta X = \Delta P$ of the quadrature operators. (b) The expectation value of the electric field for a coherent state is given by the projection of the phasor onto the X -axis. The uncertainty of the state in quadrature space leads to an uncertainty of the electric field which equally affects its amplitude and phase.

They minimize the uncertainty relation of Equation (2.17) and the uncertainty is equally distributed into the two quadratures. Furthermore, the variances are again independent of the coherent excitation α , i.e. they are the same as for the vacuum state.

The two quadratures of the field span a phase space in which a coherent state can be depicted as shown in Figure 2.1 (a). The coherent amplitude $\alpha = |\alpha|e^{i\varphi}$ is represented by an arrow or *phasor* with length $|\alpha| = \sqrt{\langle \hat{X} \rangle^2 + \langle \hat{P} \rangle^2}$ at an angle of $\varphi = \arctan(\frac{\langle \hat{P} \rangle}{\langle \hat{X} \rangle})$ to the X -axis. The uncertainty of the state in the two quadratures is indicated by a circle whose diameter is given by the standard deviations $\Delta X = \Delta P$ of the two the quadratures. A vacuum state with $\alpha = 0$ would be represented by an uncertainty circle at the origin in this picture.

The electric field of the state is proportional to the projection of the phasor onto the X -axis as shown in Figure 2.1 (b). The time evolution of the state corresponds to a rotation of the phasor with an angular frequency ω . The amplitude of the electric field is given by $|\alpha|$ and its phase shift is determined by the angle φ .

The phasor picture can be very useful to illustrate interferences between different fields or modulations of the field as depicted in Figure 2.2. It is convenient to display the phasor in a frame which is co-rotating at the *carrier frequency* ω of the mode such that only phase shifts and modulations of the field cause a rotation (or length change) of the phasors. Most of the time, the coordinate system is omitted completely since only relative phase shifts between different fields are relevant. The uncertainties have also been omitted in Figure 2.2 for more clarity. Note, that following Equation (2.12), the uncertainty circle is negligible compared to the length of the phasor anyways, for a strongly excited state. As depicted in Figure 2.2, phasors of different fields add like vectors

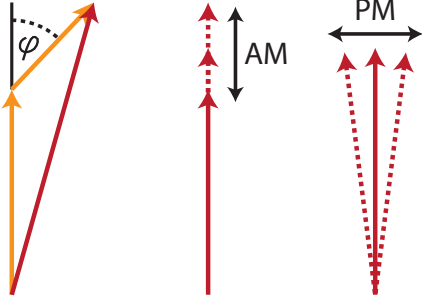


Figure 2.2: The phasor picture. Phasors of different fields (orange) add like vectors. A modulation of the length of the phasor corresponds to an amplitude modulation (AM) and a modulation of the direction corresponds to a phase modulation (PM) of the field. Modulations are often depicted by double arrows which indicate the change of the phasor.

(orange phasors) and modulations of the field cause changes of the length (*amplitude modulation*) or direction (*phase modulation*) of the phasor, which are commonly indicated by double arrows. For a small modulation index, i.e. the change of the arrow tip is small compared to the length of the phasor, a phase modulation can be approximated by an excitation of the phase quadrature, to first order.

2.3. Squeezed states of light

For a coherent state the uncertainty in the two orthogonal quadratures \hat{X} and \hat{P} is the same and it minimizes the uncertainty relation of Equation (2.17). A simultaneous reduction of the uncertainty in both quadratures is not possible. However, at the expense of an increased uncertainty in one quadrature a noise reduction along the orthogonal quadrature below the vacuum level is possible. This is exactly the case for the so-called *squeezed states*.

The squeezed states can be generated from the coherent states by applying the *squeezing operator*

$$\hat{S}(\xi) = e^{\frac{1}{2}(\xi^* \hat{a}^2 - \xi \hat{a}^{\dagger 2})} \quad \text{with} \quad \xi \equiv r e^{i\theta} \quad (2.19)$$

and with the *squeezing parameter* $0 \leq r < \infty$ and the *squeezing angle* $0 \leq \theta \leq 2\pi$. To compute the quadrature variances for a squeezed state $|\xi, \alpha\rangle = \hat{S}(\xi) |\alpha\rangle$ it is convenient to introduce the quadratures of the squeezed mode

$$\begin{aligned} \hat{X}_{\text{sqz}} &\equiv \hat{S}^\dagger(\xi) \hat{X} \hat{S}(\xi) \\ \hat{P}_{\text{sqz}} &\equiv \hat{S}^\dagger(\xi) \hat{P} \hat{S}(\xi) \end{aligned} \quad (2.20)$$

and a generalized quadrature operator

$$\begin{aligned} \hat{X}_\vartheta &\equiv \frac{1}{2} (\hat{a} e^{-i\vartheta} + \hat{a}^\dagger e^{i\vartheta}) \\ &= \hat{X} \cos \vartheta + \hat{P} \sin \vartheta \end{aligned} \quad (2.21)$$

with $\hat{X} \equiv \hat{X}_0$ and $\hat{P} \equiv \hat{X}_{\frac{\pi}{2}}$. Using the Baker-Campbell-Hausdorff lemma the quadratures of the squeezed mode can be rewritten as

$$\begin{aligned} \hat{X}_{\text{sqz}} &= \hat{X} \cosh r - \hat{X}_\theta \sinh r \\ \hat{P}_{\text{sqz}} &= \hat{P} \cosh r - \hat{X}_{\theta + \frac{\pi}{2}} \sinh r . \end{aligned} \quad (2.22)$$

For the special case of $\theta = 0$ these expressions further simplify

$$\begin{aligned}\hat{X}_{\text{sqz}} &= \hat{X} e^{-r} \\ \hat{P}_{\text{sqz}} &= \hat{P} e^{+r}\end{aligned}\tag{2.23}$$

and the variances of the squeezed quadratures are given by

$$\begin{aligned}\Delta^2 \hat{X}_{\text{sqz}} &= \frac{1}{4} e^{-2r} \\ \Delta^2 \hat{P}_{\text{sqz}} &= \frac{1}{4} e^{+2r}.\end{aligned}\tag{2.24}$$

This case ($\theta = 0$) corresponds to an *amplitude squeezed* state since the amplitude quadrature shows a reduced uncertainty, below that of a coherent state. The uncertainty in the orthogonal quadrature is increased by the same factor, such that the uncertainty relation of Equation (2.17) holds and is minimized for the squeezed states. The quadrature with the increased uncertainty is said to be *anti-squeezed*. For $\theta = \pi$ the situation is inverted and the state is called *phase squeezed*. The strength of the squeezing is determined by the squeezing parameter r .

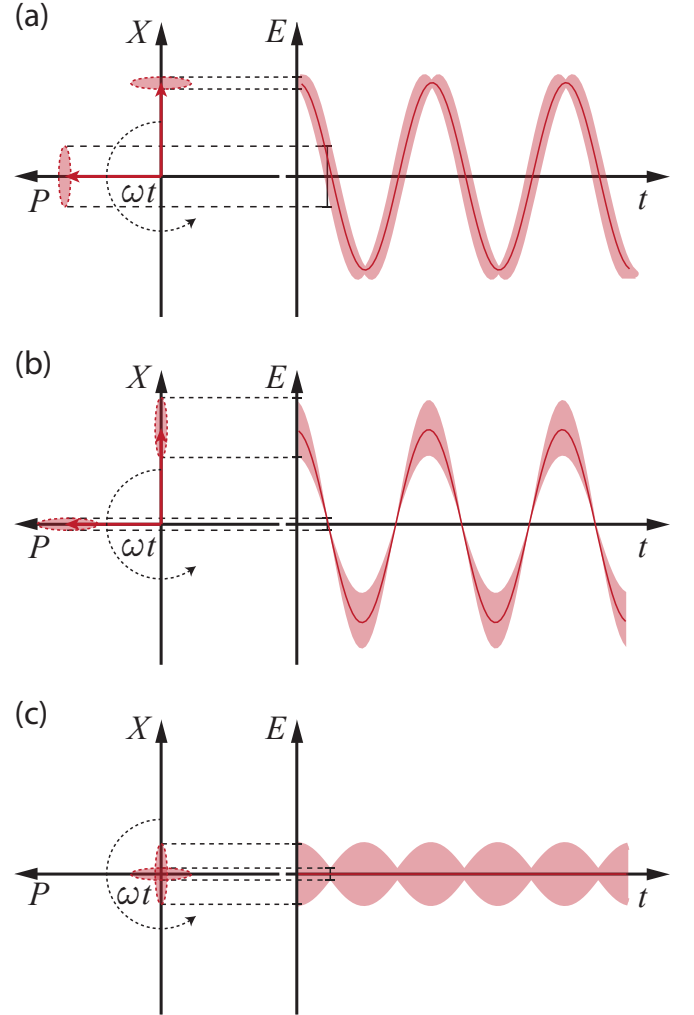


Figure 2.3: Squeezed fields. The plots show the time evolution of the electric field for (a) an amplitude squeezed state, (b) a phase squeezed state and (c) a squeezed vacuum state. The squeezed uncertainties are given by the ellipses on top of the phasors and their projection onto the X-axis leads to phase dependent noise for the electric field.

The effect on the electric field is illustrated in Figure 2.3. Since the uncertainty is no longer equally distributed in the two quadratures, the squeezing is indicated by ellipses whose widths and lengths are given by the standard deviation of the quadratures. The plots show the time evolution of the electric field as the projection of the rotating phasor into the amplitude quadrature X for (a) an amplitude squeezed state, (b) a phase squeezed state and (c) a squeezed vacuum state. The squeezing ellipse has a fixed orientation with respect to the phasor and its rotation leads to a phase dependent uncertainty of the electric field. For an amplitude squeezed state the length of the phasor has a reduced uncertainty and for a phase squeezed state the angle of the phasor is more precisely defined. Also for a squeezed vacuum state the uncertainty is phase dependent. The notion of amplitude or phase squeezing, however, only makes sense with respect to some bright reference field.

2.4. Balanced homodyne detection

A standard method to detect squeezed states of light is by employing *balanced homodyne detectors*. These detectors mix the squeezed state, or in general a weak signal field, with a strong local oscillator beam. A schematic of such a detector is shown in Figure 2.4. The local oscillator field interferes with the weak signal beam at a 50/50 beam splitter and both beam splitter outputs are being detected with photo detectors. The difference of the two photo currents yields the homodyne signal.

Let us assume a signal field \hat{s} and a strong local oscillator field \hat{b} which can be approximated by its expectation value $\langle \hat{b} \rangle = |\beta|e^{i\psi}$. The difference of the intensities at the two photo detectors is then given by

$$I_{\text{diff}} = |\beta| \langle \hat{s}e^{-i\psi} + \hat{s}^\dagger e^{i\psi} \rangle \quad (2.25)$$

or in terms of the generalized quadrature operator of Equation (2.21) and with $\vartheta \equiv \psi + \frac{\pi}{2}$

$$I_{\text{diff}} = 2|\beta| \langle \hat{X}_\vartheta \rangle \quad \text{with variance} \quad \Delta^2 I_{\text{diff}} = 4|\beta|^2 \Delta^2 \hat{X}_\vartheta . \quad (2.26)$$

The local oscillator field amplifies the signal and enables a direct measurement of an arbitrary quadrature and its variance. For an angle of $\vartheta = 0$ and $\vartheta = \frac{\pi}{2}$ a measurement of the amplitude and phase quadrature is realized, respectively.

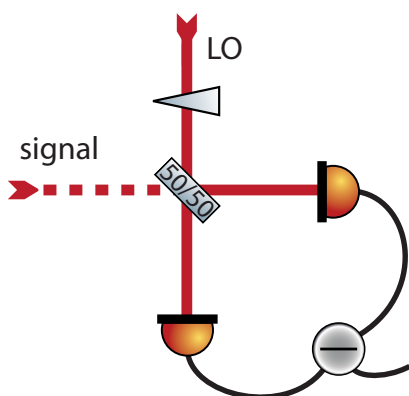
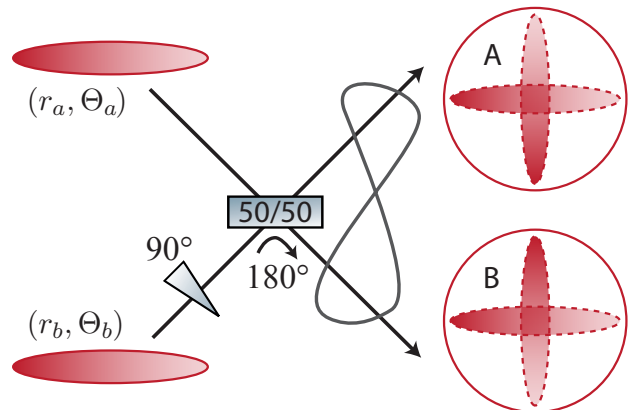


Figure 2.4: Balanced homodyne detector. A weak signal field is overlapped with a strong local oscillator field at a 50/50 beam splitter. Two photo detectors measure both beam splitter outputs and the difference of their photo currents yields the homodyne signal. The local oscillator amplifies the weak signal and enables a direct detection of the amplitude or phase quadrature of the signal beam.

2.5. Two-mode-squeezing

Two-mode-squeezed states were employed in this work to enhance the sensitivity of a split interferometer output. They can be generated experimentally by overlapping two squeezed states on a beam splitter with a relative phase shift of 90° , as illustrated in Figure 2.5. After the phase shift, one state is squeezed in the amplitude quadrature and the second one is squeezed in the phase quadrature. The resulting states in the two beam splitter outputs, individually, show increased noise in both quadratures but are entangled in the sense of the EPR-paradox.

Figure 2.5: Generation of two-mode-squeezed states. Two-mode-squeezed states can be generated by overlapping two squeezed modes on a 50/50 beam splitter with a relative phase shift of 90° . The output states show increased noise in both quadratures but are entangled in the sense of the EPR-paradox.



The two states are *entangled* in the sense of the Einstein-Podolsky-Rosen (EPR) paradox [38,39]. EPR postulated the existence of quantum mechanical systems where a measurement on a subsystem A allows a precise prediction of two orthogonal observables of a spatially separated subsystem B without disturbing system B. This means that with respect to each other the two subsystems can be arbitrarily well defined, which seemed to contradict Heisenberg's uncertainty principle. This is in fact not the case and it has been shown for a variety of different systems that these entangled states do exist [40,41].

A criterion to verify and to some extent quantify such entanglement in the continuous variable regime was established by Reid [42]. Considering two subsystems A and B with orthogonal observables $\hat{X}_{A,B}$ and $\hat{P}_{A,B}$, one can introduce so-called *conditional variances*

$$\begin{aligned}\Delta_{\text{cond}}^2 \hat{X} &\equiv \Delta^2 \hat{X}_B - \frac{\text{CoV}(\hat{X}_B, \hat{X}_A)^2}{\Delta^2 \hat{X}_A} \\ \Delta_{\text{cond}}^2 \hat{P} &\equiv \Delta^2 \hat{P}_B - \frac{\text{CoV}(\hat{P}_B, \hat{P}_A)^2}{\Delta^2 \hat{P}_A}\end{aligned}\quad (2.27)$$

with the *covariance* defined as $\text{CoV}(\hat{O}_1, \hat{O}_2) \equiv \langle \hat{O}_1 \hat{O}_2 \rangle - \langle \hat{O}_1 \rangle \langle \hat{O}_2 \rangle$. These variances correspond to the uncertainties with which the observables \hat{X}_B and \hat{P}_B can be predicted conditioned on a measurement outcome for \hat{X}_A and \hat{P}_A , respectively. If the product of the conditional variances is smaller than the limit which would be given by Heisenberg's uncertainty relation for the variances of subsystem A alone ($\Delta^2 \hat{X}_A \cdot \Delta^2 \hat{P}_A \geq \frac{1}{16}$), subsystems A and B are said to be entangled according to the EPR paradox. The *EPR-Reid*

criterion thus reads

$$\mathcal{E}^2 \equiv \Delta_{\text{cond}}^2 \hat{X} \cdot \Delta_{\text{cond}}^2 \hat{P} < \frac{1}{16} . \quad (2.28)$$

The exact value of \mathcal{E}^2 is hereby used to quantify the strength of the entanglement.

For the above described two-mode-squeezed states, let us consider two squeezed input modes a and b at the beam splitter. For an amplitude squeezed mode a and a phase squeezed mode b, the variances in the two quadratures are given by

$$\Delta^2 \hat{X}_{a,b} = \frac{1}{4} e^{\mp 2r_{a,b}} \quad \text{and} \quad \Delta^2 \hat{P}_{a,b} = \frac{1}{4} e^{\pm 2r_{a,b}} \quad (2.29)$$

with the respective squeezing parameters $r_{a,b}$. Combination of the two modes at the beam splitter leads to the two output modes A and B with quadrature components

$$\hat{X}_{A,B} = \frac{1}{\sqrt{2}} \left(\hat{X}_a \pm \hat{X}_b \right) \quad \text{and} \quad \hat{P}_{A,B} = \frac{1}{\sqrt{2}} \left(\hat{P}_a \pm \hat{P}_b \right) . \quad (2.30)$$

The variances at the two systems A and B are given by

$$\begin{aligned} \Delta^2 \hat{X}_A &= \Delta^2 \hat{X}_B = \frac{1}{2} \left(\Delta^2 \hat{X}_a + \Delta^2 \hat{X}_b \right) \\ \Delta^2 \hat{P}_A &= \Delta^2 \hat{P}_B = \frac{1}{2} \left(\Delta^2 \hat{P}_a + \Delta^2 \hat{P}_b \right) \end{aligned} \quad (2.31)$$

and the covariances reduce to

$$\begin{aligned} \text{CoV} \left(\hat{X}_B, \hat{X}_A \right) &= \frac{1}{2} \left(\Delta^2 \hat{X}_a - \Delta^2 \hat{X}_b \right) \\ \text{CoV} \left(\hat{P}_B, \hat{P}_A \right) &= \frac{1}{2} \left(\Delta^2 \hat{P}_a - \Delta^2 \hat{P}_b \right) . \end{aligned} \quad (2.32)$$

According to Equation (2.27) and with the variances of the initial squeezed states of Equation (2.29) the conditional variances take the form

$$\begin{aligned} \Delta_{\text{cond}}^2 \hat{X} &= \frac{e^{-r_a+r_b}}{4 \cosh(r_a+r_b)} \\ \Delta_{\text{cond}}^2 \hat{P} &= \frac{e^{+r_a-r_b}}{4 \cosh(r_a+r_b)} \end{aligned} \quad (2.33)$$

and their product is given by

$$\Delta_{\text{cond}}^2 \hat{X} \cdot \Delta_{\text{cond}}^2 \hat{P} = \frac{1}{16 \cosh^2(r_a+r_b)} < \frac{1}{16} . \quad (2.34)$$

In this idealized case, without considering any optical loss, two-mode-squeezed states fulfill the EPR-Reid criterion for all $r_{a,b} > 0$. They even show entanglement if only one of the input states is squeezed and the other one is a vacuum state, i.e. r_a or r_b is equal to zero.

In quantum-dense metrology we make use of this entanglement by sending one part of the two-mode-squeezed states into the interferometer and performing all our measurements with respect to the entangled reference state. The setup for this will be explained in more detail in Chapter 4.

3. Back-scatter disturbances and the approach for their subtraction

In this work, I employed a dual readout, i.e. a simultaneous readout of the phase and amplitude quadrature of an interferometer's output signal, to remove back-scatter disturbances from the scientifically interesting amplitude quadrature measurement data. The first two sections of this chapter are concerned with the relevant properties of back-scatter disturbances that allow us to distinguish them from GW signals and subtract them from the measurement data. The basic concept of the subtraction and two special types of back-scatter disturbances will be introduced in Section 3.2. Section 3.3 will give a short overview on the proof of principle setup which was used for the experimental demonstration of the new concept.

3.1. Distinguishing back-scatter disturbances from GW signals

In this section, I will illustrate how back-scatter disturbances can be distinguished from GW signals, or in general, signals from differential arm length changes in an interferometric GW detector. An easy way to see the difference between both types of signals is by looking at their representation in the phasor picture as shown in Figure 3.1.

A gravitational wave changes the lengths of the interferometer arms and only the phase of the light returning from the end mirrors is modulated. In Figure 3.1 (a), the red phasors depict the resulting modulated field in one interferometer arm. For a GW signal, the direction of the phasor changes at the modulation frequency, about a tiny angle, and its length remains approximately the same.

For the scatter disturbance the situation is different. In the scatter signal part of Figure 3.1 (a) the phasor on the left side shows again the resulting modulated field in the interferometer arm and the orange phasors on the right side illustrate how it is generated. As already described in the Introduction, back-scatter disturbances in GW detectors arise from unwanted reflections in the interferometric setup which interact with moving components in the environment, become phase modulated and are then back-scattered into the interferometer mode. Due to the additional path outside of the interferometer the back-scattered beam accumulates a phase shift φ with respect to the interferometer light and its phasor is therefore rotated by that angle. Coherently combining the back-scattered beam (short orange phasor) with the residual interferometer light (long orange phasor) leads to the resulting modulated field given by red phasor. Its phase is shifted by

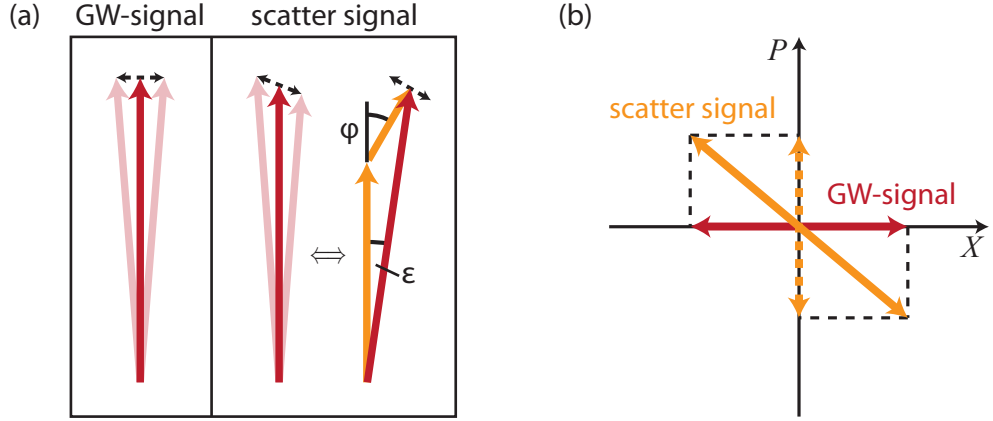


Figure 3.1.: GW signal and scatter disturbance in the phasor picture. (a) Generation of a scatter disturbance signal compared to a GW signal. The red phasors depict the resulting field in one interferometer arm. The orange phasors describe the situation where some light is scattered out of the interferometer mode, becomes phase modulated and is afterwards back-scattered into the interferometer mode. An additional phase shift φ for the back-scattered light leads to a rotation of the modulation in phase space. (b) Comparison of the GW signal and the scatter disturbance in the (dark) interferometer output. The dashed lines indicate the projection of the scatter signal into the amplitude (X) and phase (P) quadratures. In an amplitude quadrature measurement both signals would look the same but a phase quadrature measurement would reveal the scatter disturbance.

a constant angle ϵ that depends on the phase shift φ of the back-scattered light and the respective amplitudes of the residual interferometer light and the back-scattered beam. Note that the drawing is not to scale and the amplitude of the back-scattered light is strongly exaggerated. For a realistic GW detector scenario ϵ should always be negligible compared to φ . This constant rotation itself does not constitute a problem since it only causes a small dc-offset at the interferometer output. The disturbance signal is due to the resulting modulation (indicated in dashed black) of the recombined red phasor which is also rotated by an angle of approximately φ (because ϵ is tiny). The illustration on the left side in the scatter signal part of Figure 3.1 (a) shows that the modulation no longer constitutes a pure phase modulation of the recombined beam. Not only the direction of the phasor changes at the modulation frequency but also its length, which corresponds to an additional amplitude modulation.

In Figure 3.1 (b) the GW signal and the scatter disturbance are depicted as they appear in the interferometer output. Since GW detectors are normally operated at a dark fringe (or at least close to it), the carrier fields from the two arms cancel each other and only the tiny modulation signals remain. Throughout this thesis, the quadrature in which the GW signal (red) lies at the interferometer output is denoted the *amplitude* quadrature X because amplitude modulations are the measured quantity in all current GW detectors. The scatter signal (orange) is rotated in phase space with respect to the

GW signal. In an amplitude measurement, i.e. measuring the projection of the signals onto the X -axis, both signals shown here look exactly the same. However, an additional measurement of the phase quadrature (projection onto the P -axis) would solely show the scatter disturbance (dashed orange) and would therefore reveal the different origin of the two signals.

3.2. Modeling back-scatter disturbances for their subtraction

As discussed in Section 1.4, the additional information from a phase quadrature measurement has already been used to identify and discard corrupted measurement data [32,33]. In this work, I went one step further and used the phase quadrature data to find an analytical description for the scatter disturbance signal. The phase quadrature data is optimally suited for this purpose since it offers a reference measurement for the scatter disturbance which is free of any ‘scientific’ signals from real differential arm length changes. The model deduced in this way could then be subtracted from the amplitude measurement data to actually improve the measurement sensitivity in the affected frequency range.

If $\varphi(t)$ describes the relative phase shift of a back-scattered beam with respect to the interferometer mode in the respective arm, the projections of the resulting disturbance signal in the phase quadrature p and the amplitude quadrature x at the interferometer output are given by

$$p_{\text{sc}}(t) = A \cdot \cos \varphi(t) \quad (3.1)$$

$$x_{\text{sc}}(t) = A \cdot \sin \varphi(t) \quad (3.2)$$

with some signal amplitude A which depends on the interferometer transfer function and the intensity of the back-scattered beam. A was assumed to be constant and frequency independent throughout this work. The back-scatter signal is not exactly the same in both quadrature projections but it depends on the same parameters. If A and $\varphi(t)$ can be determined from the phase quadrature measurement, the projection of the scatter disturbance in the amplitude quadrature can easily be computed via Equation (3.2).

My approach to determine $\varphi(t)$ was to fit an analytical model to the phase quadrature measurement data which described the time dependent phase shift of the back-scattered light due to a certain motion of the scatter source.

The simplest example for an analytical description one can probably think of is a sinusoidal motion of the scatter source with constant parameters. The time dependent phase shift of the back-scattered light can then be modeled by

$$\varphi(t) = \varphi_0 + m \sin(2\pi f_m t + \phi_m) \quad (3.3)$$

with constant modulation depth m , frequency f_m and phase ϕ_m and a constant overall phase shift φ_0 which accounts for the total mean path length that the back-scattered

beam traveled outside the interferometer. Though this model is rather elementary, a scatter source like this can already lead to quite complex disturbance signals. In fact, it provides the basis for the description of all scatter disturbances that were investigated in this work. Two important examples will be introduced in the next subsections.

3.2.1. The case of small amplitude motion

For small amplitude motion of the scatter source, i.e. a modulation depth $m \ll 1$, the scattered light beam becomes modulated in its phase quadrature as depicted in the phasor diagram of Figure 3.1. To first order approximation Equations (3.1)-(3.2) with the time dependent phase shift of Equation (3.3) reduce to

$$p_{\text{sc}}(t) \approx \underbrace{A m \sin \varphi_0}_{A_p} \cdot \sin(2\pi f_m t + \phi_m) \quad (3.4)$$

$$x_{\text{sc}}(t) \approx \underbrace{A m \cos \varphi_0}_{A_x} \cdot \sin(2\pi f_m t + \phi_m) \quad (3.5)$$

where the dc parts have been left out. The projection of the scatter disturbance into the two quadrature measurements, in this case, leads to a simple sinusoidal signal. It has the same ‘shape’ in both projections and the two are either in phase or exactly out of phase. The signal amplitudes A_p and A_x differ for the two quadrature projections and the angle under which the signal appears in phase space at the output of the interferometer depends on the total mean phase shift φ_0 of the back-scattered beam with respect to the interferometer mode. In a spectrum, such a disturbance shows up as a monochromatic peak for both quadrature measurements. Disturbances of this type will be investigated in Section 6.1.

3.2.2. A broadband scatter shoulder from frequency up-conversion

This section is concerned with the case of a so-called ‘scatter shoulder’ that is produced by back-scatter sources with large amplitude motion ($m > 1$), as already mentioned in the Introduction and described, for example, in [23–25, 29]. Such a broadband disturbance can be generated via frequency up-conversion from a single source which is moving sinusoidally with constant parameters. Using the phase shift of Equation (3.3) in Equations (3.1) and (3.2) we obtain the analytical model for the projection of the scatter disturbance in the phase and amplitude quadratures

$$p_{\text{sc}}(t) = A \cdot \cos(\varphi_0 + m \sin(2\pi f_m t + \phi_m)) \quad (3.6)$$

$$x_{\text{sc}}(t) = A \cdot \underbrace{\sin(\varphi_0 + m \sin(2\pi f_m t + \phi_m))}_{\equiv \varphi(t)} \quad (3.7)$$

For large amplitude motion of the scatter source, we have to consider the case of deep modulation $m > 1$, where so-called ‘fringe wrapping’ occurs and upconverts low frequency motion to higher frequencies.

The model of Equations (3.6)-(3.7) is displayed in Figure 3.2 for a parameter set of $\varphi_0 = 0^\circ$, $m = 32.7$, $f_m = 5$ Hz, $\phi_m = 0^\circ$ and some arbitrary amplitude A . These parameters were chosen to be comparable to later measurement results. The used modulation depth corresponds to a total path length change of $m\lambda/\pi = 10.4\lambda$ for the scattered light. Figure 3.2(a) shows the modeled projections of the disturbance in the two orthogonal quadratures p_{sc} (blue) and x_{sc} (red) in time domain. To illustrate the effect of fringe wrapping, the motion of the scatter source itself is also plotted in dashed gray, for comparison. The time domain plot shows that in this case, the shape of the disturbance signal is different in the two quadratures while the signal amplitude is the same in both projections. This is the exact opposite of the case described in Section 3.2.2.

A good way to understand the resulting disturbance signal is via the Doppler shift of the back-scattered light. The frequency shift of the back-scattered light is proportional to the instantaneous velocity of the scatter source in the direction of beam propagation. In terms of $\varphi(t)$ it is given by $f_{ds}(t) = \dot{\varphi}(t)/2\pi$, which results in

$$f_{ds}(t) = m f_m \cos(2\pi f_m t + \phi_m) \quad . \quad (3.8)$$

The frequency shift is small around the turning points of the motion and the maximal frequency shift is reached when source passes the center of its motion. According to Equation (3.8), the maximum frequency component of the disturbance signal is given by $f_{ds}^{\max} = m f_m$ and for a modulation depth $m > 1$, this represents frequency up-conversion. Figure 3.2(b) shows the time-frequency behavior of the scatter model in a spectrogram. Due to the limited resolution both quadrature projections look the same in this plot and only the phase quadrature projection is shown here. The scatter disturbance appears as ‘arches’ that directly describe the time dependent frequency shift of the back-scattered light, as observed in a single-sided spectrum. The absolute value of the Doppler shift in Equation (3.8) is overlaid in gray.

In Figure 3.2(c) the (averaged) power spectral density (PSD) of the disturbance is shown in both quadrature projections. Here, the disturbance appears as the name-giving broadband shoulder. The averaged PSD was computed with Matlab’s ‘pwelch’ function, using a Hanning window spanning half the oscillation period of the scatter source ($\Delta t = 1/(2f_m)$) and an overlap of 50%. These settings were chosen to get a sufficient frequency resolution without reducing the shoulder to the harmonics of f_m by temporal averaging. The bump structure of the scatter shoulder results from the projection into the orthogonal quadratures because the different frequency components are being generated at different total distances from the interferometer. The clarity of this structure strongly depends on the length of the windowed data segments and their alignment with respect to the oscillation of the scatter source. Scatter disturbances of this type were used in all other experiments of Chapters 6 and 7.

Although the model described here is quite simple, it already reproduces the basic structure of typical disturbance signals as observed in GW detectors [23–25, 29].

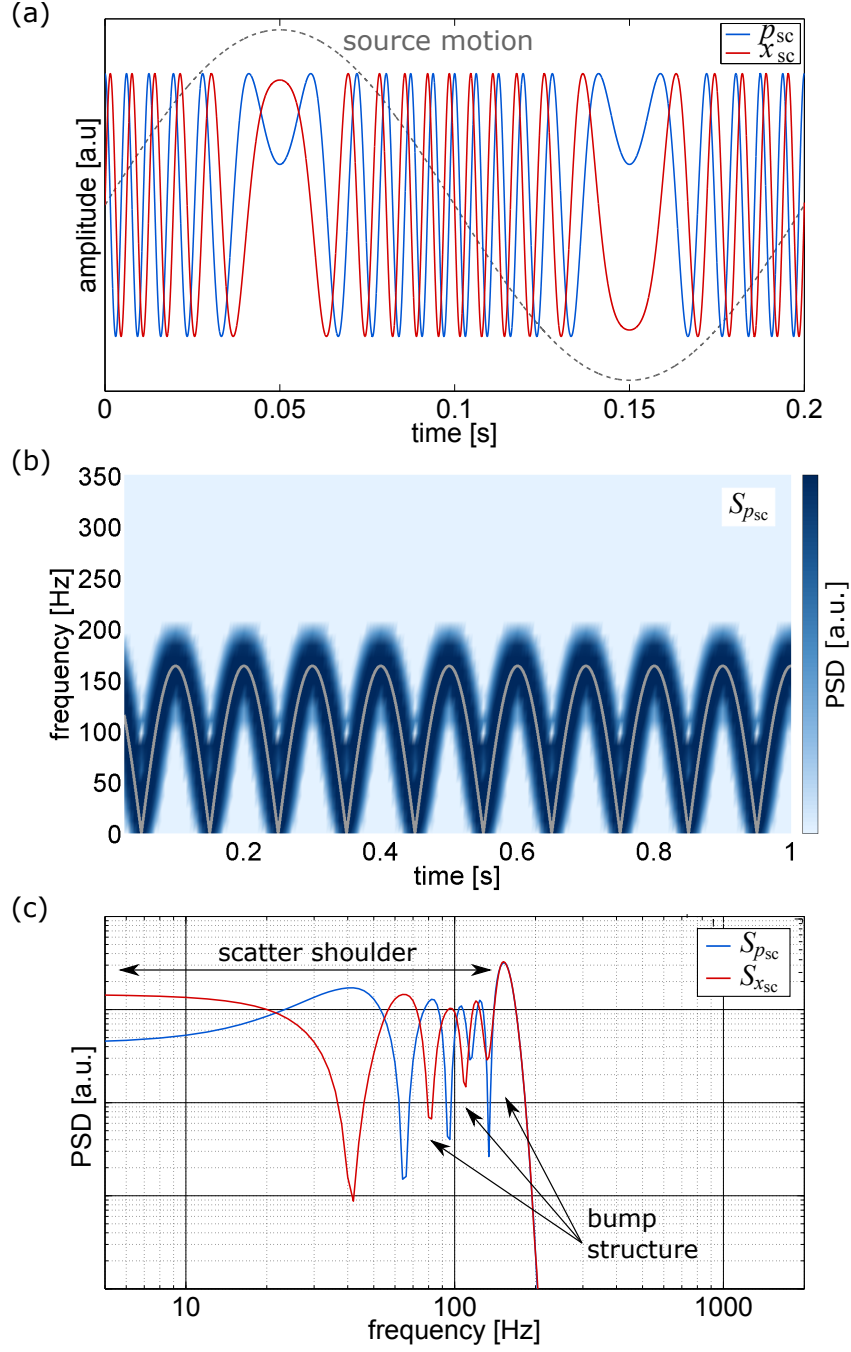


Figure 3.2.: A scatter shoulder from frequency up-conversion. The plots show a modeled disturbance signal from a sinusoidally moving scatter source with a large amplitude motion of several wavelengths. p_{sc} and x_{sc} denote the projections of the disturbance signal in the phase quadrature and amplitude quadrature. (a) Model in time domain illustrating the effect of fringe wrapping. (b) Spectrogram of the modeled disturbance. The ‘arches’ describe the time dependent Doppler shift f_{ds} for the back-scattered light as it appears in a single-sided spectrum. $|f_{ds}(t)|$ is overlaid in gray. (c) Averaged power spectral density (PSD) showing the name-giving broadband shoulder with the overlaid bump structure.

3.3. Proof of principle setup

For a proof of principle of the subtraction of back-scatter disturbances, I used a simplified optical setup as depicted in Figure 3.3. The setup in this form was employed in all experiments of Chapter 6. The sub-shot-noise enhancement of the readout will be explained in Chapter 4 and was applied in the experiment of Chapter 7.

I used a simple table-top Michelson interferometer to generate different test signals. For each setup (i) a GW like signal, due to a differential arm length change was produced by modulating one of the interferometer end mirrors and (ii) a back-scatter disturbance was injected through the other interferometer end mirror. The injected disturbances varied from a simple monochromatic peak in the spectrum ($m \ll 1$) to a broadband scatter shoulder with multiple round-trips for the back-scattered beam ($m > 1$). These signals and their experimental generation will be described in more detail in the respective sections of Chapter 6. In all experiments presented here, the interferometer was operated at a dark fringe and its output field was split at a 50/50 beam splitter to allow for a simultaneous measurement of the two quadratures. Two balanced homodyne detectors (BHD1&2) were used to measure the split output signal. As described in Section 2.4, these detectors employed strong external local oscillator fields which enabled a direct readout of the amplitude and phase quadratures. The readout quadratures were determined by the phases of the local oscillator beams with respect to the signal beams. Here, ‘0°’ corresponded to an optimal readout of the GW-like signal. The readout scheme in this form will be denoted as *dual (homodyne) readout* throughout this thesis.

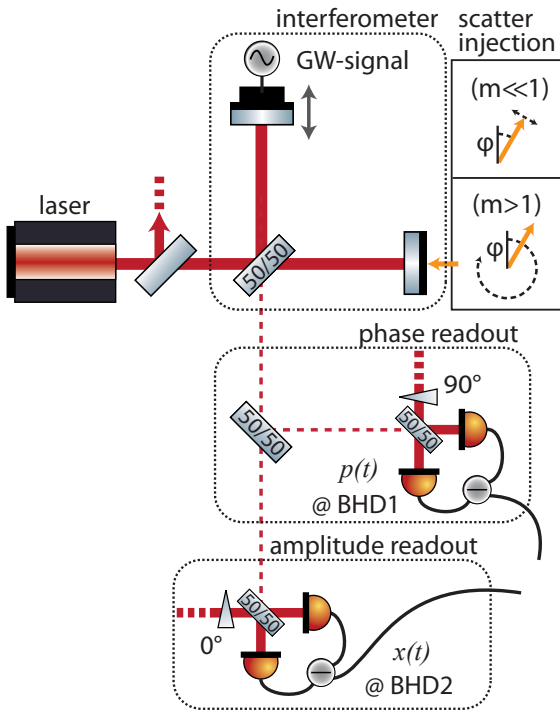


Figure 3.3: Dual readout for subtraction of back-scatter disturbances.

In a Michelson interferometer we distinguish two different types of signals (i) a GW-like signal due to a differential arm length change and (ii) a back-scatter disturbance from interference of a modulated external beam with the interferometer mode. The angle φ describes the relative phase shift between the back-scattered beam and the interferometer mode in the respective arm. For the dual readout, the interferometer output is (equally) split into two parts. Two balanced homodyne detectors (BHD1&2) read out the orthogonal amplitude $x(t)$ and phase quadrature $p(t)$ of the interferometer signal. The amplitude quadrature readout contains the GW-like signal and the phase quadrature readout provides a reference measurement of the back-scatter disturbance.

Note, that the balanced splitting of the interferometer output field in the setup presented here has the consequence that the signal power in the scientifically relevant amplitude quadrature readout is halved. In a regime where an interferometer is limited by classical excess noise, this is not a problem because the noise power is also halved at the respective detector. In the shot noise limited regime, however, the signal-to-noise-ratio is decreased by a factor of 2 due to the splitting. In general other splitting ratios could be considered for implementation in gravitational-wave detectors, compromising between loss for the scientific signal and signal-to-shot-noise-ratio in the scatter monitor.

4. Quantum-dense metrology

In this chapter I will show how the dual readout can be enhanced to sub-shot-noise performance in both quadrature measurements, thereby entering the regime of *quantum-dense metrology* (QDM) [33]. The simultaneous readout of the two signal quadratures in the proposed setup requires splitting of the interferometer’s output light and thus reduces the signal-to-(squeezed-)shot-noise ratio in the ‘scientific’ amplitude quadrature readout. In QDM this can be partially compensated for because the optical loss for the respective squeezed state is also reduced. This effect will be discussed in Section 4.2.

4.1. The quantum-dense readout

The dual readout of Section 3.3 can be enhanced to sub-shot-noise sensitivity in both quadrature readouts by using two-mode-squeezed states of light. A single quadrature squeezed scheme [16–18] as described in Section 1.2, is not applicable with the split interferometer output described in Section 3.3. The situation is depicted in Figure 4.1. The beam splitter in the interferometer output opens an additional vacuum port and therefore reduces the squeezing at the amplitude readout (BHD2). For balanced splitting the maximally achievable non-classical noise suppression in the amplitude readout is a factor of 2, corresponding to about 3 dB of squeezing. Additionally, the orthogonal quadrature of the interferometer output is anti-squeezed, which significantly reduces the extractable information about the disturbance.

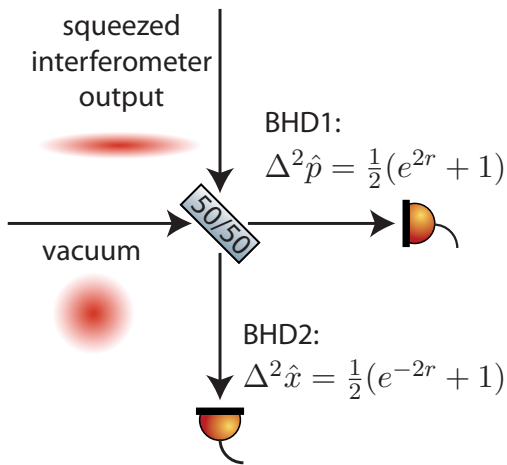


Figure 4.1: Split single quadrature squeezed readout. For a single (amplitude) quadrature squeezed interferometer readout, splitting the output field introduces an additional vacuum port. For balanced splitting and the variance of a vacuum state being normalized to unity, the minimal variance achievable in the amplitude quadrature readout becomes $\Delta^2 \hat{x} = 1/2$. This corresponds to about 3 dB of squeezing. The variance in the phase quadrature readout is dominated by anti-squeezing, which significantly reduces the extractable information about potential disturbance signals.

The scheme I am going to discuss here was experimentally demonstrated in [33–35] and constitutes a case of so-called ‘quantum-dense metrology’ (QDM). The term QDM refers to the increased measurement information from the second quadrature readout and indicates the close analogy to quantum-dense coding in quantum information science. QDM employs entangled, two-mode-squeezed states of light (see Section 2.5) in a Mach-Zehnder configuration with the Michelson interferometer in one of its arms, as depicted in Figure 4.2. Two squeezed states are being overlapped at a 50/50 beam splitter with a relative phase shift of 90° to create the entanglement. One part of the resulting two-mode-squeezed state is being reflected at the interferometer dark port and picks up the interferometer signal. A GW signal and a scatter disturbance signal are indicated in the drawing by the red and orange phasors, corresponding to their representation in Figure 3.1.

The second part of the two-mode squeezed state serves as a reference and is sent directly to the 50/50 beam splitter in the interferometer output. Recombination of the two entangled parts with the right phase relation brings the initial squeezed states back. In the two beam splitter outputs, two balanced homodyne detectors (BHD1&2) measure the phase and amplitude quadratures of the interferometer signal. The measurements correspond to a projection of the respective fields onto the indicated axes. Neglecting optical loss, the variances of the phase and amplitude quadratures at the respective detectors (BHD1&2) correspond exactly to the squeezed variances of the two squeezed

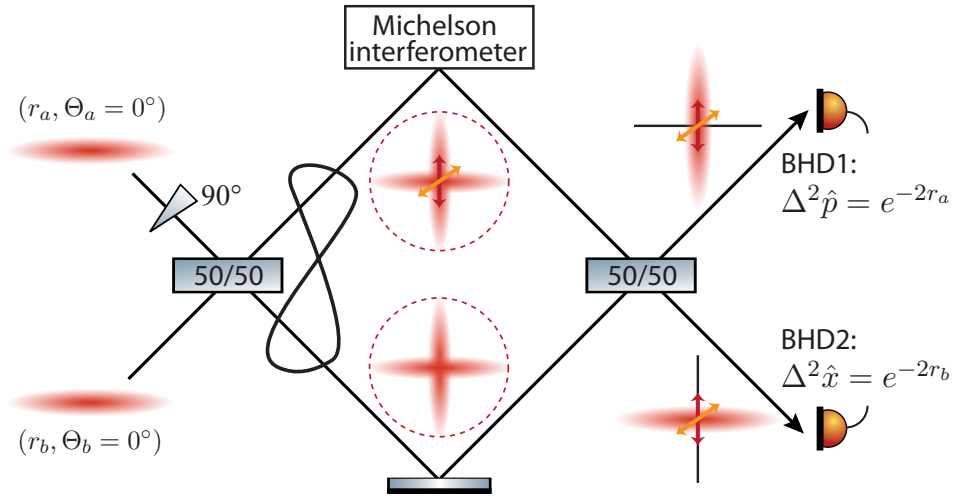


Figure 4.2.: Schematic setup for quantum-dense metrology. Two squeezed states are being overlapped at a 50/50 beam splitter with a relative phase shift of 90° , thereby creating entanglement. One output state is being reflected at the dark port of a Michelson interferometer while the other one is sent directly to a second 50/50 beam splitter in the interferometer output. Recombination of the two entangled states enables simultaneous sub-shot-noise measurement of the amplitude x and phase quadrature p of an interferometer signal (indicated by the red double-headed arrows). $r_{a,b}$ and $\Theta_{a,b}$ denote the squeezing parameters and squeezing angles of the respective states.

input states and a sub-shot-noise measurement of both orthogonal signal quadratures can be realized.

4.2. Considering optical loss in quantum-dense metrology

As discussed in the last section, in QDM the shot noise reduction in the amplitude measurement does not degrade due to the 50/50 splitting of the interferometer output. Interestingly, if we take into account optical losses in the interferometer path, we can even gain squeezing strength with respect to a single quadrature squeezed readout as proposed by Caves and used in GEO 600 [16–18]. This effect can partly compensate for the halved signal power in the amplitude detector of the dual readout which was discussed in Section 3.3. The considerations in this section were published in a paper which presents the results of Chapter 7 [43]. They were not further investigated experimentally in this work. As discussed in the last section, in QDM the shot noise reduction in the amplitude measurement does not degrade due to the 50/50 splitting of the interferometer output. Interestingly, if we take into account optical losses in the interferometer path, we can even gain squeezing strength with respect to a single quadrature squeezed readout as proposed by Caves and used in GEO 600 [16–18]. This effect can partly compensate for the halved signal power in the amplitude detector of the dual readout which was discussed in Section 3.3. The considerations in this section were published in a paper which presents the results of Chapter 7 [43]. They were not further investigated experimentally in this work.

The advantage in QDM is that only one of the entangled beams suffers from loss inside the interferometer path while the loss in the second path can be kept relatively low. Depending on the initial squeezing strength available, for a certain range of optical loss, the signal-to-(squeezed-)shot-noise ratio is reduced by less than a factor of 2 (down to a factor of 1.5) due to the splitting of the interferometer signal. For high optical loss, however, the imperfect cancellation of anti-squeezing dominates, leading to even larger factors.

In the GEO 600 scenario with a single quadrature squeezed state and no splitting of the interferometer output [16] the squeezed variance of the amplitude quadrature at the photo detector is given by

$$\Delta^2 \hat{x}_{\text{SQZ}}(r, \eta_{\text{ifo}}) = 1 - \eta_{\text{ifo}} + e^{-2r} \eta_{\text{ifo}} \quad (4.1)$$

with the squeezing parameter r , the path efficiency η_{ifo} and the variance of a vacuum state being normalized to unity. For QDM, let us consider again the setup given in Figure 4.2 and assume an idealized case where the squeezed input states are pure and the loss in the second path outside the interferometer can be neglected. The variance of

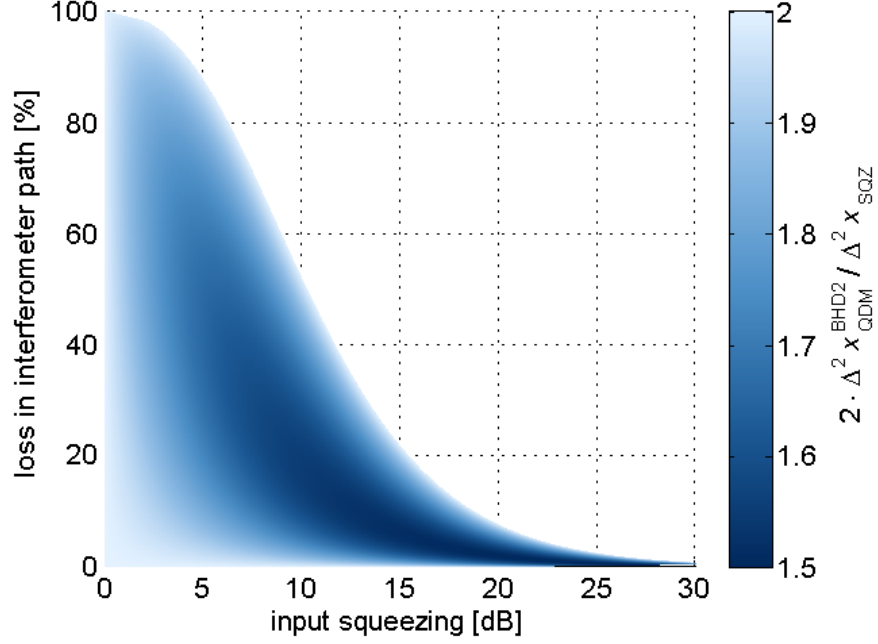


Figure 4.3.: Comparison of QDM with a single quadrature squeezed readout. The plot shows the ratio of the quantum noise variances for the amplitude measurements in the respective scenarios, depending on the loss inside of the interferometer path and the input squeezing strength. The ratio was scaled with a factor of two, accounting for the halved signal power in QDM. For QDM we assumed the idealized case with pure squeezed states as input at the first beam splitter and no loss in the path of the second entangled state, outside the interferometer. The region where the variance in QDM ($\Delta^2 \hat{x}_{\text{QDM}}^{\text{BHD2}}$) becomes larger than the one for the single quadrature squeezed readout ($\Delta^2 \hat{x}_{\text{SQZ}}$) has been cut off for clarity. This plot was taken from the publication in [43].

the amplitude quadrature at the amplitude detector BHD2 then reads

$$\begin{aligned} \Delta^2 \hat{x}_{\text{QDM}}^{\text{BHD2}}(r, \eta_{\text{ifo}}) &= \frac{1}{2}(1 - \eta_{\text{ifo}}) + \frac{1}{4}e^{-2r}(\sqrt{\eta_{\text{ifo}}} + 1)^2 \\ &+ \frac{1}{4}e^{+2r}(\sqrt{\eta_{\text{ifo}}} - 1)^2 . \end{aligned} \quad (4.2)$$

The plot in Figure 4.3 shows the ratio of the two variances depending on the optical loss inside the interferometer path ($100 \cdot (1 - \eta_{\text{ifo}})$) and the input squeezing strength in dB ($10 \cdot \log_{10}(e^{2r})$). The ratio is scaled with a factor of 2, accounting for the splitting of the signal power in QDM. The blue colored region shows the regime where we gain squeezing strength in QDM with respect to the single quadrature squeezed case, i.e. we lose less than a factor of 2 in signal-to-(squeezed)-shot-noise ratio. The region where the anti-squeezing dominates the variance has been cut off because it is practically not relevant. In the presence of high optical loss, high squeezing values are only disadvantageous since they increase the influence of phase noise [44–46]. This is true for a single quadrature squeezed readout, as well as for QDM.

The plot shows that optical loss needs to be considered when we want to quantify

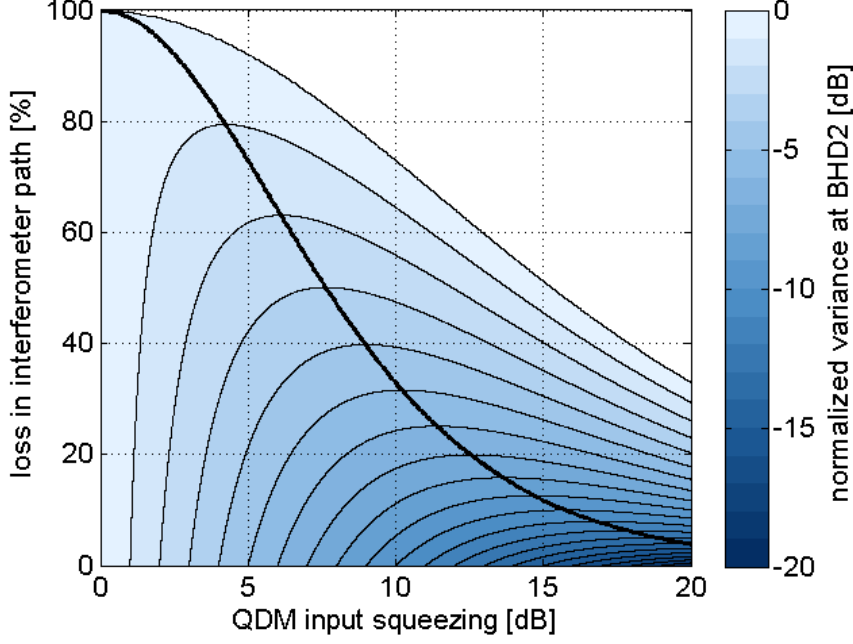


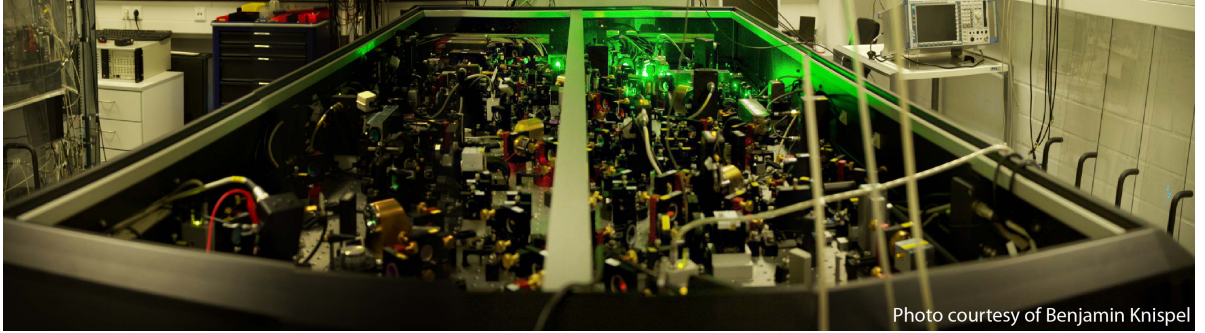
Figure 4.4.: Optimal input squeezing in QDM. The plot shows the regime in which sub-shot-noise sensitivity is achieved at the amplitude quadrature detector (BHD2) in QDM, depending on the optical loss inside the interferometer path. Overlaid in black is the optimal value for the input squeezing strength according to Equation (4.3).

the signal-to-(squeezed-)shot-noise ratio in QDM with respect to a single quadrature squeezed readout. For realistic detector scenarios, like for example 10 dB of input squeezing and 25% loss [20, 47], it will most likely decrease by less than a factor of 2. For the idealized case considered here, these parameters would lead to a factor of about 1.58.

Another point that might be interesting for an actual implementation of QDM in gravitational-wave detectors is the following. For the single quadrature readout, ignoring phase noise, higher squeezing values are always better, i.e. lead to a lower variance at the photo detector, independently of optical loss. In QDM however, depending on the optical loss (in the interferometer path) there is always an optimal value for the input squeezing strength

$$r_{\text{QDM}}^{\text{opt}}(\eta_{\text{ifo}}) = \frac{1}{4} \ln \left(\frac{(\sqrt{\eta_{\text{ifo}}} + 1)^2}{(\sqrt{\eta_{\text{ifo}}} - 1)^2} \right) , \quad (4.3)$$

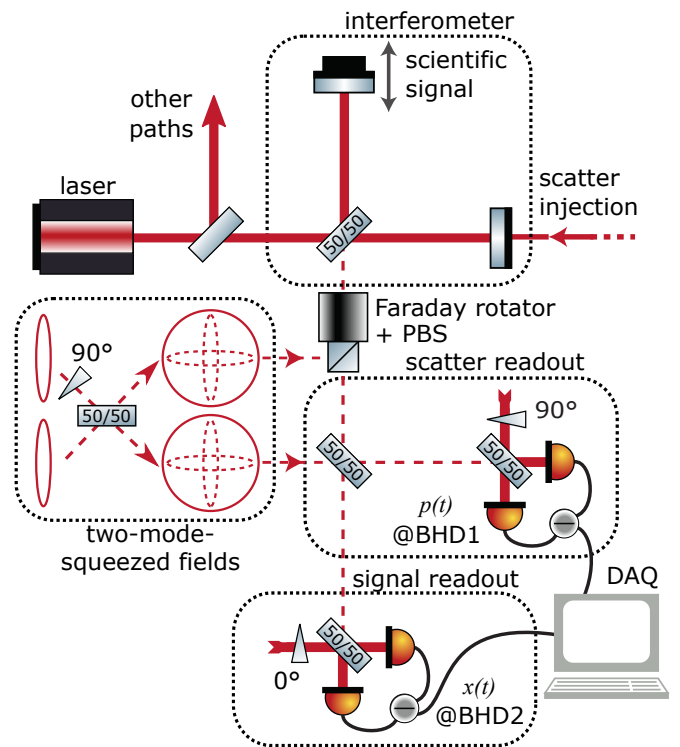
due to the imperfect cancellation of the anti-squeezing. This can easily be derived by setting the derivative of Equation (4.2) with respect to r to zero. Note that this still refers to the idealized case which considers pure input states and no loss in the reference path. The colored contour plot in Figure 4.4 shows the regime in which sub-shot-noise sensitivity is achieved at the amplitude detector (BHD2) in QDM. Overlaid in black is the optimal value for the input squeezing strength according to Equation (4.3).



5. Main parts of the experimental setup

In this chapter I will describe the main parts of the experimental setup. Parts that were specific for the different experiments will be described in the respective sections of Chapters 6 & 7. A simplified schematic of the complete setup is shown in Figure 5.1. I employed a continuous wave Nd:YAG laser source at 1064 nm with an output power of 2 W. The light was split to supply the different parts of the experiment. A table-top Michelson interferometer was used to generate different test signals and will

Figure 5.1: Schematic of the overall experimental setup. A continuous wave Nd:YAG laser source at 1046 nm with an output power 2 W was split to supply the different parts of the experiment. A Michelson interferometer was used to generate different test signals. Its output was equally split and two balanced homodyne detectors (BHD1&2) were used to simultaneously measure the orthogonal amplitude $x(t)$ and phase quadratures $p(t)$ of the interferometer's output field. In the experiment of Chapter 7 the readout was enhanced with two-mode-squeezed states of light to reach the sub-shot-noise regime of quantum-dense metrology. DAQ: data acquisition system.



be described in Section 5.1, as well as the dual readout of the orthogonal signal quadratures. The source for the two-mode-squeezed states will be discussed in Section 5.2 and their implementation in a quantum-dense readout is presented in Section 5.3. A data acquisition system was implemented to allow for data post-processing and will be described in Section 5.4.

5.1. Michelson interferometer with dual homodyne readout

A photograph of the table-top Michelson interferometer with the dual readout is shown in Figure 5.2. The paths of the relevant beams for this section are highlighted in red, the dashed parts show paths where no bright carrier field was present (except for control beams). First of all, the light coming from the laser (upper right corner) was spa-

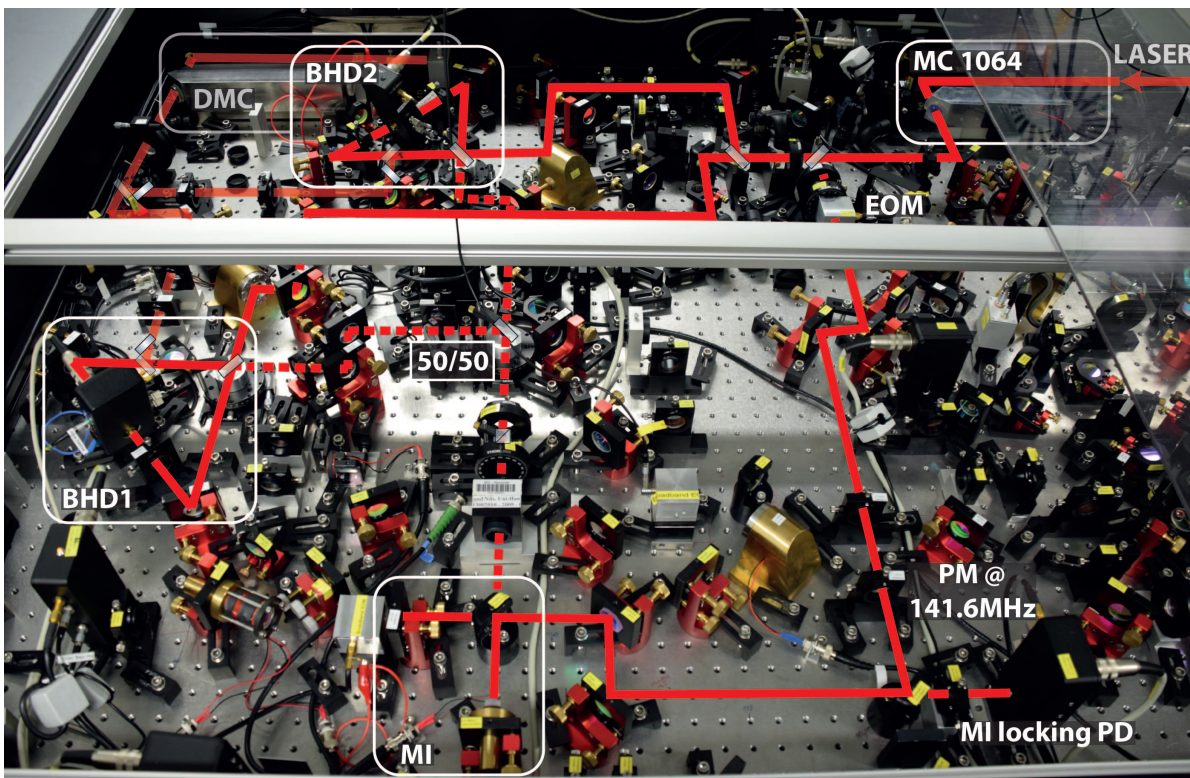


Figure 5.2.: Photo of the table-top Michelson interferometer with dual homodyne readout. MC: mode cleaner, EOM: electro-optic modulator, PM: phase modulation, PD: photo detector, MI: Michelson interferometer, BHD: balanced homodyne detector, DMC: diagnostic mode cleaner.

tially filtered to get a clean TEM00 mode, using a three mirror ‘mode cleaning cavity’ (MC1064). Behind the mode cleaning cavity, the beam was split to provide the input field of the Michelson interferometer (MI) and the local oscillators for the two balanced homodyne detectors (BHD1&2) of the dual readout.

The Michelson interferometer, in the bottom part of the picture, had an arm length of about 7 cm and an input power of about 10 mW. The transfer function of the interferometer was white over the relevant frequency range of about 5 kHz around 5.2 MHz. Apart from the intentionally introduced scatter disturbances, optical shot noise was limiting the measurement sensitivity. One arm of the interferometer was slightly longer than the other arm ($\Delta L \approx 1.5$ cm) to allow for locking the interferometer to a dark fringe via the Schnupp modulation technique [48]. This technique requires a phase modulation (PM) on the interferometer input field which is partly converted into an amplitude modulation by recombination of the beams at the interferometer beam splitter, due to the macroscopic arm length difference. A phase modulation at 141.6 MHz was imprinted on the input beam with a resonant electro-optic modulator (EOM). The error signal was acquired with a resonant photo detector (PD) in reflection of the interferometer and used to adjust the position of one of the interferometer end mirrors (south arm in the photo) with a piezoelectric element.

With the interferometer I was able to produce different test signals. GW-like signals, due to a differential arm length change, could be generated by modulating the same interferometer end mirror that was also used for locking the interferometer. These signals were used as references that should stay unaffected by the post-processing of the data. The scatter disturbance signals were produced in the second interferometer arm by injecting a modulated beam in different ways through the partially transmissive ($R \approx 98\%$) second end mirror. I used audio band test signals that were shifted to the MHz regime before injection into the interferometer and demodulated again before data acquisition. This was done mainly because there was no squeezing measurable in the used setup for sideband frequencies below about 3 MHz due to the employed control scheme (see Section 5.2). Additionally, acoustic disturbances from the environment could be avoided by operating in this frequency regime. The exact generation of the different test signals will be described in more detail in the respective sections of Chapters 6 & 7.

The output field of the interferometer was split at a 50/50 beam splitter and two balanced homodyne detectors (BHD1&2) with local oscillator powers of about 10 mW measured its amplitude and phase quadratures (8 mW for the experiments of Sections 6.2 and 6.3). Both detectors used custom made photo diodes with high quantum efficiencies $\gtrsim 99\%$ that were aligned close to the Brewster angle to minimize reflections and maximize detection efficiency. The readout quadratures were determined by the phases of the local oscillator with respect to the interferometer signal beam as described in Section 2.4. For stabilization of the two detectors to the respective quadratures some additional control fields were required. The locking scheme for the full quantum-dense readout will be explained in Section 5.3. The experiments in Chapter 6 used simplified control schemes which will be described in the corresponding sections.

To achieve good visibilities at the beam splitters of BHD1&2, all beams could be directed via flip mirrors to a so-called ‘diagnostic mode cleaner’ (DMC), a three mirror

ring cavity shown in the upper left corner of the photograph in Figure 5.2. By optimally aligning all beams to the cavity mode also the mode overlap of the different beams with respect to each other was optimized. The paths are depicted slightly transparent to indicate that they were not in use when measurements were being performed.

The setup in this configuration, without sub-shot-noise enhancement, was used in the experiments of Chapter 6.

5.2. Source for the two-mode-squeezed states

For the transition to quantum-dense metrology we need entangled, two-mode-squeezed states. The source for these states, used in this work, was described and characterized in reference [49]. The setup of the source was part of the PhD theses of S. Steinlechner and J. Bauchowitz [35, 50]. A photograph of the experimental setup is depicted in Figure 5.3. The laser source is shown in the bottom left corner of the photo. After isolation against back-reflections, a phase modulation at 124.1 MHz was imprinted on the beam with an electro-optic modulator (EOM1). The modulation was used to stabilize the lengths of the two mode cleaning cavities MC 1064 and MC 532 and the cavity used for second harmonic generation (SHG) via the Pound-Drever-Hall (PDH) technique [51].

The beam was then split in three parts. The first one was directed to the mode cleaning cavity MC 1064 which was already mentioned in the last section and provided the local oscillators for the Michelson interferometer and the dual readout. The sec-

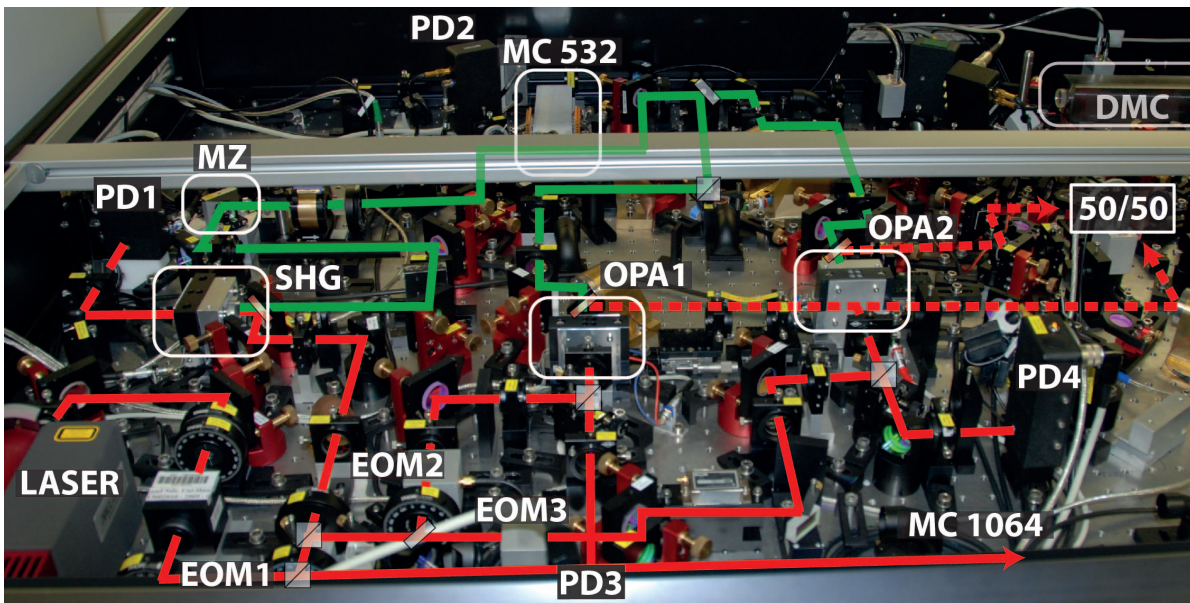


Figure 5.3.: Photo of the two-mode-squeezed light source. EOM: electro-optic modulator, PD: photo detector, MZ: Mach-Zehnder interferometer, SHG: second harmonic generation, MC: mode cleaner, OPA: optical parametric amplifier, DMC: diagnostic mode cleaner

ond one was sent to the SHG to produce the pump field at 532 nm, required for the squeezed light generation. The SHG used a magnesium oxide doped lithium niobate crystal ($\text{MgO}:\text{LiNbO}_3$) as non-linear medium and its temperature was stabilized by peltier elements to maintain phase matching conditions. The power of the 532 nm beam (green in the picture) was stabilized with a small Mach-Zehnder interferometer (MZ) and its spatial mode was cleaned, using another three mirror filter cavity (MC 532), before it was split and sent to the two squeezed light sources OPA1&2. The pump fields each had a power of about 60 mW and were injected from the back sides, through the out-coupling mirrors of the respective cavity.

The squeezed states were generated via optical parametric down-conversion in a non-linear crystal [47, 52, 53]. OPA1&2 used periodically poled potassium titanyl phosphate (PPKTP) as non-linear medium which has a higher effective non-linearity than lithium niobate and allows for more stable phase matching at lower temperatures due to its periodic poling (quasi-phasematching) [54–56]. Both crystals were temperature stabilized as well to ensure optimal conversion between the pump and the fundamental fields. OPA1 was a ‘monolithic’ source where the cavity was formed directly by the coated surfaces of the crystal and OPA2 was ‘hemilithic’ which means that the cavity was formed by one crystal surface and a separate out-coupling mirror. The monolithic design generally allows for lower intracavity loss, and therefore higher squeezing values, but the hemilithic design was useful to achieve simultaneous resonance for the two OPA cavities. In both OPAs one crystal surface had a highly-reflective (HR) coating for both wavelengths and the out-coupling surface/mirror had a reflectivity of 90% for the fundamental wavelength (1064 nm) and 20% for the second harmonic field (532 nm).

The third part of the initial, split field was split again and served as control beams for OPA1&2. Both beams were phase modulated with two electro-optic modulators (EOM2&3) at 47.8 MHz and 32.5 MHz, respectively. They had a power of about 1 mW and were injected into OPA1&2 from the front sides, through the HR coatings. The PDH error signals for stabilizing OPA1&2 on resonance were detected in reflection with the photo detectors PD3&4. For the monolithic source (OPA1) the laser frequency was actuated to resonate in the cavity and the cavity length of the hemilithic source (OPA2) was adjusted with its piezo actuated out-coupling mirror to obtain simultaneous resonance. Error signals for the stabilization of the pump fields’ phases with respect to the control beams at the fundamental wavelength were obtained by shifting the phases of the electronic demodulation at PD3&4 by 90° . The pump phases were stabilized on deamplification for the fundamental field by adjusting the (microscopic) position of piezo actuated mirrors in the respective pump fields’ paths. Due to technical noise from the laser source that coupled in through the control beams of OPA1&2, there was no squeezing detectable for sideband frequencies below about 3 MHz in this setup. Therefore, all measurements in this work were performed in a higher frequency regime around 5 MHz where the measurements were shot-noise limited. Implementation of a quantum-dense readout in GW detectors would require a coherent control scheme, as it is used in GEO 600 [57, 58], to avoid the coupling of technical laser noise into the squeezed beam at frequencies in the detectors’ sensitive band.

The squeezed output fields at 1064 nm (dashed paths) were separated from the re-

flected pump fields via dichroic beam splitters (DBS) and sent to a 50/50 beam splitter to generate the entangled, two-mode-squeezed fields. To optimize the contrast between the two fields, one beam splitter output could be directed via a flip mirror to another diagnostic mode cleaner (DMC) shown in the upper right corner of the picture. The stabilization of the relative phase shift between the two squeezed states and the implementation of the entangled output beams in the dual readout will be described in the next section.

The setup was shown to produce strong entanglement with an EPR-value of $\mathcal{E}^2 = 0.039$ according to Equation (2.28) [49]. For this measurement, both squeezed light sources were stably operated with detected squeezing values of about 10 dB and the two-mode-squeezed states were measured with two balanced homodyne detectors closely behind the 50/50 beam splitter that created the entanglement.

5.3. Quantum-dense readout

To reach the sub-shot-noise regime of quantum-dense metrology (QDM), the two-mode-squeezing was implemented in the dual readout of Section 5.1 as depicted in the photograph of Figure 5.4. The squeezed beams from OPA1&2 (dashed red) enter the picture from the right side together with a single sideband (SSB) at 80 MHz (light blue). Note that the photo of the two-mode-squeezed light source in Figure 5.3 was taken from the opposite side of the table. To describe the locking procedure, the whole setup is also schematically depicted in Figure 5.5.

The two squeezed fields were overlapped on a 50/50 beam splitter to create the entangled, two-mode-squeezed states. In each output of the beam splitter 1% of power was picked off and detected with a combined photo detector ①. The difference of the two photo currents provided an error signal for stabilization of the relative phase shift between the two squeezed fields to the required 90° . The phase shift was adjusted with a piezo actuated mirror in the path of OPA1.

One of the entangled beams was sent to the Michelson interferometer (MI) and reflected at its dark port via a combination of a Faraday isolator and a polarizing beam splitter (PBS). The second entangled state was sent directly to the 50/50 beam splitter in the output of the interferometer.

For stabilization of the relative phase shift for the recombination of the two entangled beams, a single-sideband (SSB) at 80 MHz was used. The SSB was produced with an acousto-optic modulator (AOM) and a pick-off from the laser's main beam. It was overlapped with the first entangled state through an HR mirror, before it entered the interferometer. The beat note at 80 MHz between the SSB and the combined control fields from the squeezed light sources was measured in reflection of the HR mirror, using a resonant photo detector ②. After demodulation at 80 MHz it served as an error signal to stabilize the relative phase between the SSB and the first entangled state to an arbitrary angle. The two fields recombined with the second entangled state at the 50/50 beam splitter in the interferometer output. A pick-off of 1% was taken at each beam splitter output again and detected with another combined photo detector

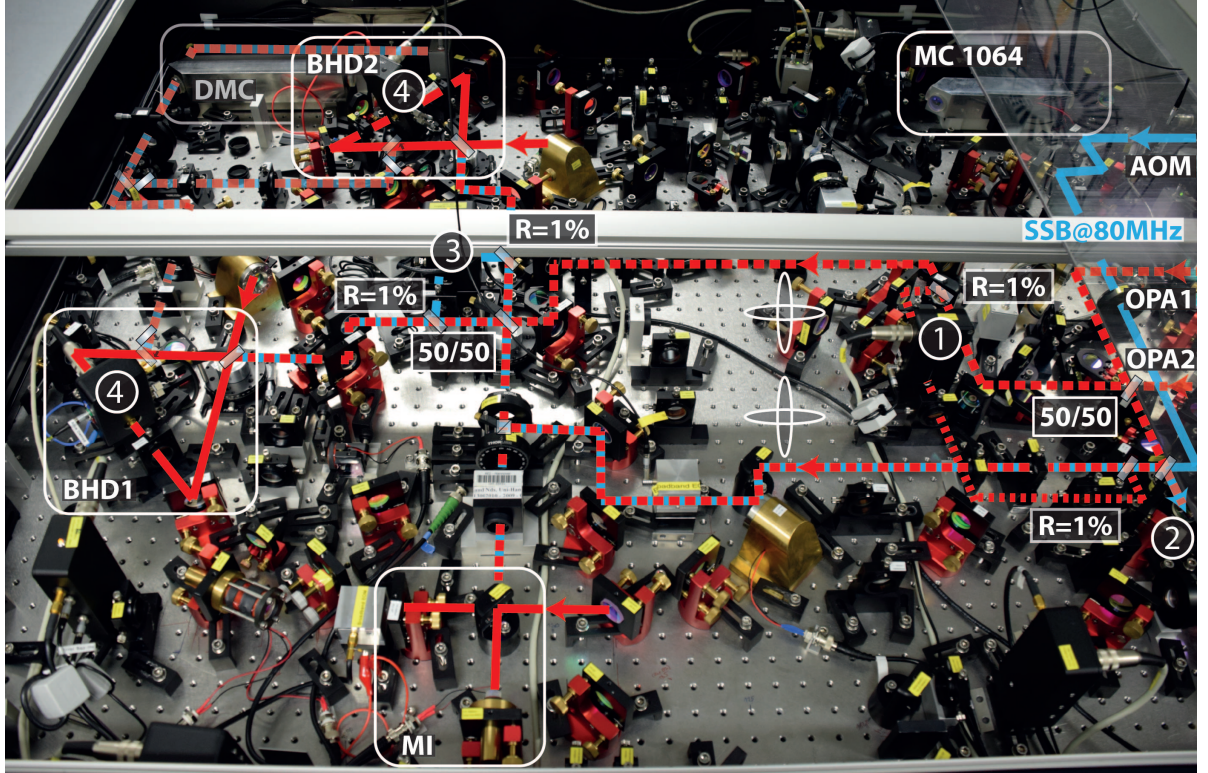


Figure 5.4.: Photo of the table-top Michelson interferometer with quantum-dense readout. MC: mode cleaner, AOM: acousto-optic modulator, OPA: optical parametric amplifier, R: power reflectivity, PD: photo detector, MI: Michelson interferometer, BHD: balanced homodyne detector, DMC: diagnostic mode cleaner.

③. By taking the difference of the two photo currents, the beat note between the SSB and the control beams of the first entangled state canceled out and only the beat note between the SSB and the second entangled state remained. Electronic demodulation at 80 MHz led to an error signal for stabilization of the relative phase shift between the two entangled states. Depending on the phase of the demodulation, their relative phase shift could be stabilized to an arbitrary value. After locking the balanced homodyne detectors (BHD1&2) to measure the orthogonal quadratures, the phase of the electronic local oscillator was tuned to recover optimal squeezing at both detectors.

The quadrature angle of the two BHDs was stabilized with the help of the two phase modulated control beams of OPA1&2. Since the OPAs were locked on deamplification, they produced amplitude squeezing related to their respective control fields and the squeezed quadratures were exactly aligned with the direction where the phase modulation vanished. Demodulation of the homodyne signals at the respective frequencies allowed for locking the readout quadratures to the initial squeezed quadratures of OPA1&2 using phase shifters in the paths of the optical local oscillators ④.

At last, the orthogonal quadratures measured at BHD1&2 needed to be aligned with respect to the interferometer signal such that GW-like signals from differential arm

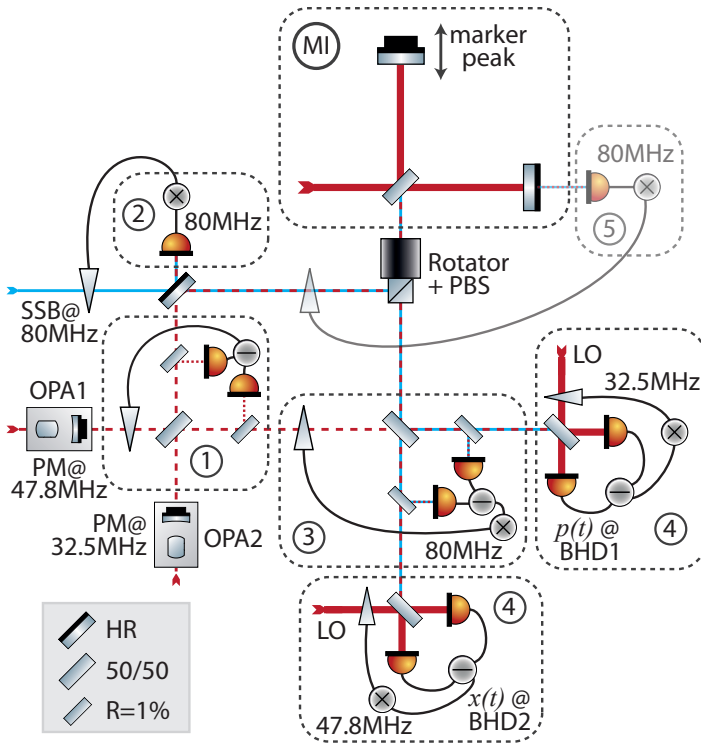


Figure 5.5: Schematic of the locking procedure for the quantum-dense readout. The quantum-dense readout was stabilized with the help of a SSB at 80 MHz and the two phase modulated control beams of OPA1&2 at 47.8 MHz and 32.5 MHz, respectively. The four steps of the locking procedure are described in the main text. Step five shows a possibility to stabilize the readout quadratures with respect to the interferometer signal. MI: Michelson interferometer, PBS: polarizing beam splitter, HR: high-reflectivity mirror, OPA: optical parametric amplifier, SSB: single sideband, PM phase modulation, BHD: balanced homodyne detector.

length changes were optimally aligned in the amplitude detector (BHD2) and vanished in measurements at the phase quadrature detector (BHD1) accordingly. This part was not electronically stabilized but adjusted by shifting the phase of the first entangled beam to minimize a marker peak in the spectrum of BHD1. The marker peak was generated by modulating one interferometer end mirror with a piezo actuator.

In principle this last degree of freedom could also be stabilized using the 80 MHz SSB like it was done in the QDM setup of [33–35]. Its beat note with the bright interferometer mode is much stronger than the one with the weak control beams coming from the squeezed light sources and can be detected behind one of the interferometer end mirrors ⑤. This lock was omitted here for practical reasons.

5.4. Data acquisition

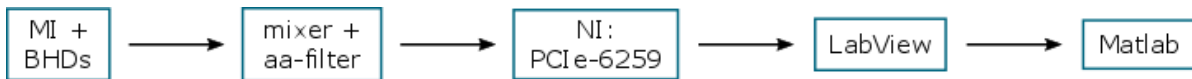


Figure 5.6.: Schematic sequence of data acquisition and processing.

For the post-processing of the measurement data from the two orthogonal quadratures I implemented a data acquisition system (DAQ) as it is schematically depicted in Figure

5.6. As already explained before, all measurements in this work have been performed in the MHz range due to technical noise at low frequencies. Therefore, as a first step for the data acquisition, the measurement data from the two balanced homodyne detectors were electronically mixed down at a frequency of about 5 MHz and filtered with a 9-pole low pass filter at a passband frequency of 3 kHz to avoid aliasing. The resulting audio band signals were acquired with a PCIe-6259 card from National Instruments (NI).

I wrote a LabView program to process the experimental measurement data. A screenshot of the user interface and the corresponding block diagram are shown in Figures A.1 to A.3 of the Appendix. The program was used to save the raw time domain data of the two input channels for BHD1&2 to text files, including information like e.g. the sample rate in the header of the file. Also, the power spectrum of the two channels was computed and displayed for tunable resolution bandwidth (RBW) and averaging factor. This was employed to adjust the quadrature angle of the two homodyne detectors as mentioned in the last section. There were two different ‘save modes’ available: (i) saving the data length required for a given resolution bandwidth (RBW) and number of averages (to reproduce the displayed spectrum) and (ii) saving the data length required for a given measurement time. The program was buffering the data, so that the saved data corresponded to what was visible in the live spectrum before hitting the stop button. I implemented an additional feature that enabled me to play a sound file and save the measurement data during the time while the file was playing. The sound output of the PC (via external speakers) was fed as an external modulation into an Agilent 33500B series wave form generator and used to generate a GW-like signal in some of the

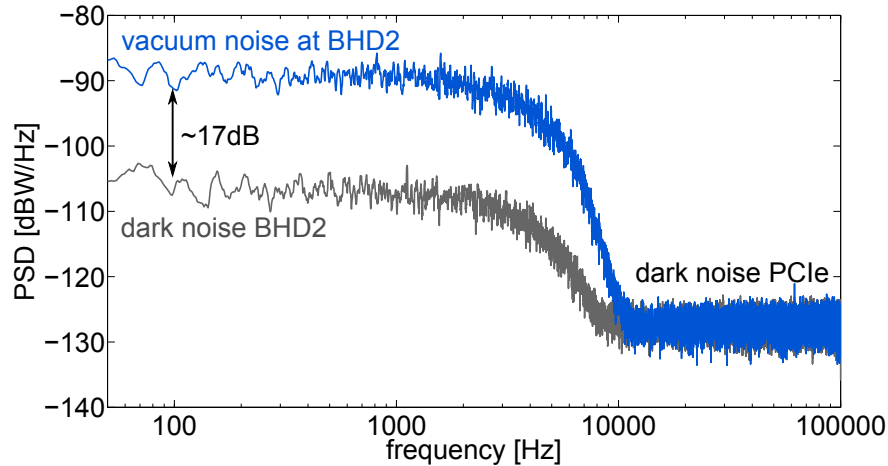


Figure 5.7.: Performance of the data acquisition. The plot shows the power spectral density (PSD) of vacuum noise measured at BHD2 and transferred through the DAQ chain (blue). The noise was mixed down at 5.25 MHz and filtered against aliasing with a low pass filter at 3 kHz. The measured vacuum noise was suppressed below the dark noise of the PCIe card for frequencies above ≈ 10 kHz. The biggest dark noise contribution in the measurement frequency regime was given by the dark noise of BHD2 (gray). It lay about 17 dB below the measured vacuum noise level.

experiments. Synchronizing the injection of the sound signal and the data taking was important to be able to produce good reference measurements which contained only the GW-like signal, while the scattered light was blocked in the setup. The post-processing for subtraction of the back-scatter disturbances was done in Matlab and will be described in the respective sections of Chapters 6 & 7.

Throughout this work, the data were sampled at a frequency of $f_s = 200$ kHz. Figure 5.7 shows the power spectral density of a vacuum noise measurement at BHD2 (blue) which served as a (white) signal of typical size. The vacuum noise level lay about 40 dB above the dark noise of the PCIe card in the frequency range relevant for the measurements and it was suppressed below the dark noise of the PCIe card for frequencies above about 10 kHz (and therefore also above the Nyquist frequency $f_{ny} = \frac{1}{2}f_s$). The limiting dark noise for the measurements was given by the dark noise of the balanced homodyne detectors. It is shown in gray in Figure 5.7 and lay about 17 dB below the measured vacuum noise level.

6. Experimental demonstration of a dual homodyne readout for subtraction of back-scatter disturbances

In this chapter I will present some experiments that I performed as a proof of principle for the subtraction of back-scatter disturbances. The setup for all these experiments was the one described in Section 5.1 and used no entangled-light enhancement. A schematic is shown again in Fig. 6.1. Sections 6.1 to 6.3 describe experiments for different types of back-scatter disturbances varying from a simple monochromatic peak in the spectrum to broadband scatter shoulders with multiple round-trips for the scattered light beam. Apart from the scatter disturbances, optical shot noise was the limiting noise source in all experiments of this chapter.

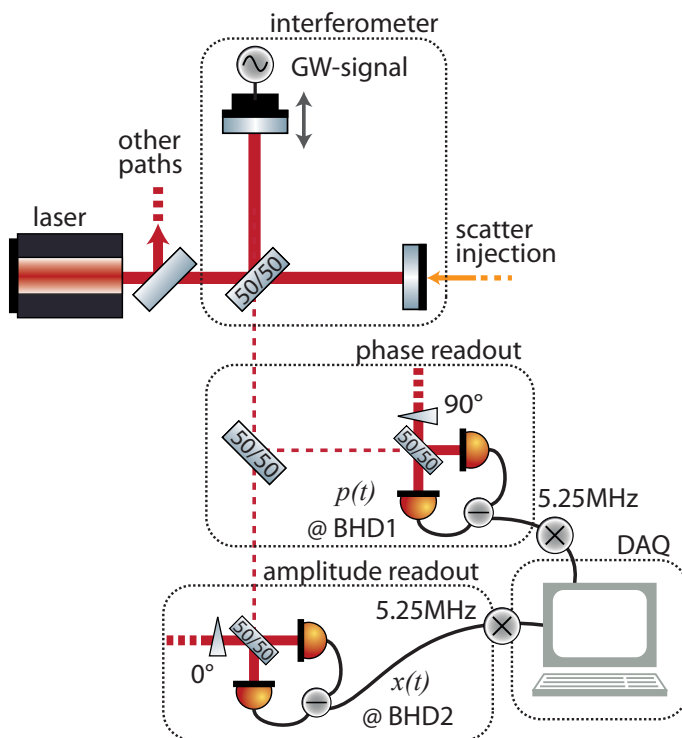


Figure 6.1: Schematic of the experimental setup. A Michelson interferometer was employed to generate two different types of signals (i) a GW-like signal due to a differential arm length change and (ii) a back-scatter disturbance from interference of a modulated external beam with the interferometer mode. The interferometer output was (equally) split into two parts. Two balanced homodyne detectors (BHD1&2) read out the orthogonal amplitude $x(t)$ and phase quadratures $p(t)$ of the interferometer signal. DAQ: data acquisition system.

6.1. Scatter sources with small amplitude motion

In this section I will start with the most simple example for a scatter disturbance, a monochromatic peak in the spectrum as it was already used in the demonstration of quantum-dense metrology [33]. In a second step, the disturbance will become slightly more complex by imprinting an additional low frequency phase modulation on the peak. The additional phase modulation led to a surrounding sideband structure and gave the scatter disturbance a distinct time-frequency behavior.

The experimental generation of the test signals, including a GW-like signal as a reference, will be described in Section 6.1.1. The locking scheme for stabilization of the dual homodyne readout in this experiment was different from the one shown in Section 5.3 and will be described in Section 6.1.2. In Section 6.1.4 I will show that both types of disturbances could be fully subtracted using the post-processing of Section 6.1.3. The resulting sensitivity was increased to the shot noise level over the whole frequency range.

6.1.1. Experimental generation of the test signals

As already mentioned, I employed a table-top Michelson interferometer to generate two different types of test signals. A photo of the setup is shown in Figure 6.2 where the interferometer beam is given in red.

A GW-like signal due to a differential arm length change was produced by modulating one of the interferometer end mirrors with a piezo actuator (north arm in the picture).

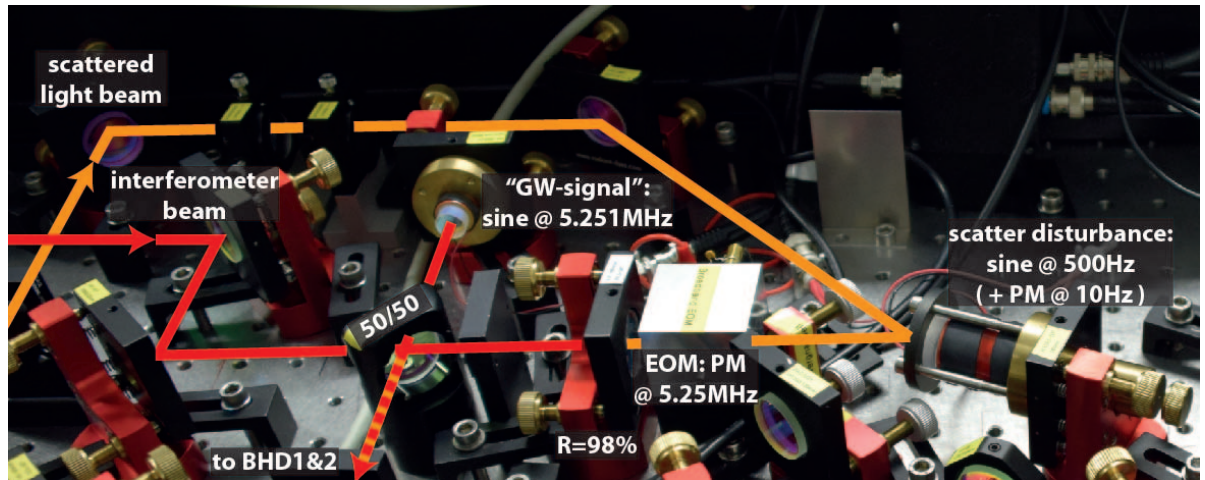


Figure 6.2.: Experimental generation of the test signals. The photo shows the table-top Michelson interferometer that was used to generate the test signals (red beam). A GW-like signal, due to a differential arm length change, was produced by modulating one piezo actuated interferometer end mirror (north arm). The scatter disturbance was generated with an external beam (orange) that was injected through the second interferometer end mirror, which had a reduced power reflectivity of $R = 98\%$. PM: phase modulation, EOM: electro-optic modulator, BHD: balanced homodyne detector.

The piezo actuator was driven with a sinusoidal signal at 5.251 MHz. After demodulation with 5.25 MHz during data acquisition, this resulted in a monochromatic peak at 1 kHz. The peak was also used as a marker to adjust the quadrature angles for the measurements at BHD1&2 with respect to the interferometer signal, as described in Section 6.1.2.

For the generation of the scatter disturbance, an external beam was used which was picked off the main beam in front of the interferometer (orange beam). It was injected through the second interferometer end mirror (east arm in the picture) which had a reduced power reflectivity of $R = 98\%$. An external beam was used because this made it easier to produce sufficiently large disturbance signals in this table-top setup. On its path, the beam was first modulated with an audio band disturbance signal, via a piezo actuated mirror. As already mentioned, two different signals were used: (i) a pure sinusoidal modulation at 500 Hz, leading to another monochromatic peak in the spectrum and (ii) a sinusoidal 500 Hz signal whose phase was additionally modulated at 10 Hz with different modulation depths, leading to different sideband structures. The resulting signals were shifted by 5.25 MHz with an electro-optic modulator (EOM) before they were injected in the interferometer. The Michelson interferometer was stabilized to a dark fringe and its (dashed) output beam was sent to the two balanced homodyne detectors BHD1&2 of the dual readout. The data were acquired as described in Section 5.4 and the post-processing was done in Matlab, as described in Section 6.1.3.

6.1.2. Stabilization of the dual homodyne readout

This experiment used a simplified locking scheme for the stabilization of the dual homodyne readout, employing solely the 80 MHz single sideband (SSB) which was introduced in Section 5.3. The scheme is depicted in Figure 6.3. The SSB was reflected at the

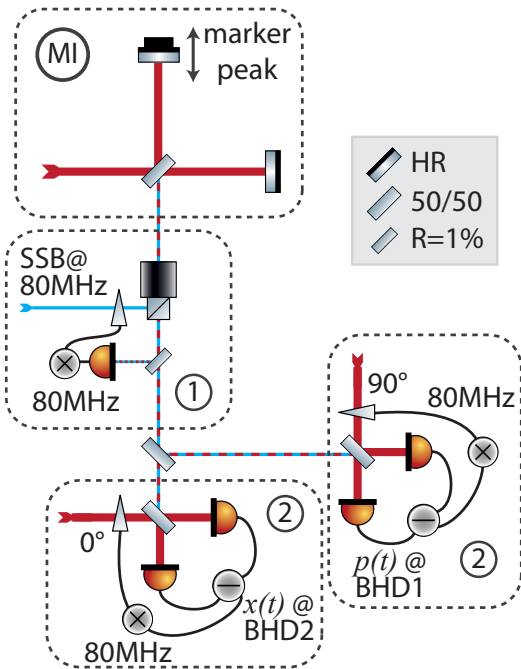


Figure 6.3: Locking scheme for the dual homodyne readout. A single sideband (SSB) at 80 MHz was reflected at the interferometer dark port and its phase was stabilized with respect to the interferometer signal ①. Afterwards the local oscillator phases at the two balanced homodyne detectors (BHD1&2) were stabilized with respect to the SSB ②. A marker peak was used to determine the readout quadratures for the detection. MI: Michelson interferometer, HR: high-reflectivity mirror.

interferometer dark port via a combination of a Faraday rotator and a polarizing beam splitter and thereby overlapped with the interferometer output signal. One percent of the output power was picked off and detected with a resonant photo detector ①. The beat signal from the two fields was demodulated and used to stabilize their relative phase shift to an arbitrary value. Afterwards the beat of the SSB with the local oscillator beams of the two balanced homodyne detectors could be used to stabilize the readout quadratures ②. The homodyne signals were demodulated at 80 MHz and employed to control phase shifters in the respective local oscillator paths. The phase for the electronic demodulation was adjusted to minimize/maximize the injected marker peak of Section 6.1.1 in the phase/amplitude quadrature detector.

6.1.3. Post-processing

The measurement data of the two balanced homodyne detectors contained the orthogonal projections of the test signals in the two quadratures. The post-processing of the data followed the description in Section 3.2. First, an analytical model for the scatter disturbance was fitted to the phase quadrature data of BHD1. Afterwards, the projection of the disturbance into the amplitude quadrature measurement was computed and subtracted from the data of BHD2.

As described in Section 3.2.1, for scatter sources that move sinusoidally with a small amplitude motion, the projections of the disturbance into the orthogonal phase and amplitude quadratures at the interferometer output reduces to

$$p_{\text{sc}} = A_{\text{p}} \sin(2\pi ft + \phi) \quad (6.1)$$

$$x_{\text{sc}} = A_{\text{x}} \sin(2\pi ft + \phi) \quad . \quad (6.2)$$

These expressions are equivalent to Equations (3.4) & (3.5), only the subscripts in the frequency f and phase ϕ of the motion have been skipped and the differing amplitudes of the quadrature components have been combined in A_{p} and A_{x} for clarity. For the disturbance peak with sideband structure, an additional modulation term needed to be inserted in the sine of Equations (6.1) & (6.2), leading to the analytic models

$$p_{\text{sc}} = A_{\text{p}} \sin(2\pi ft + \phi + m \sin(2\pi f_{\text{m}}t + \phi_{\text{m}})) \quad (6.3)$$

$$x_{\text{sc}} = A_{\text{x}} \sin(2\pi ft + \phi + m \sin(2\pi f_{\text{m}}t + \phi_{\text{m}})) \quad . \quad (6.4)$$

For fitting the model of Equation (6.1), or (6.3) respectively, to the phase quadrature data of BHD1, all parameters were supposed to be free within reasonable ranges. To find good start parameters and boundaries for the fitting, some analyzing of the phase quadrature data was done in advance. First, the power spectral density (PSD) was computed for the whole data set of 5s length. A plot of the PSD for an exemplary measurement with a modulated peak is shown in Figure 6.4. All frequency components whose amplitudes exceeded a certain threshold were declared as excess noise. The threshold was defined using the PSD of a reference shot noise measurement that was obtained by blocking the signal port of BHD1. It was set to 1.3 times the maximum

value of the shot noise measurement and is shown in red in Figure 6.4. The center of the excess noise frequency range was used as a start parameter for the main frequency f and the corresponding boundaries were set to the minimum and maximum frequency components of the excess noise.

The excess noise frequency components were grouped into peaks by combining neighboring points and taking their center frequency. The most frequently occurring distance between two adjacent peaks (within a margin of 1 Hz) was used as starting point for the frequency of the additional modulation f_m in Equation 6.3. The boundaries were set to the minimum possible peak distance (two times the resolution bandwidth) and the width of the excess noise range.

The start parameters for the amplitudes A_p and A_x were determined directly from the time domain data of the respective detectors. They were set to half of the maximum measurement value, while the minimum and maximum values were used as boundaries. The phases ϕ and ϕ_m started at 0 and were constrained by $\pm 2\pi$ and the modulation depth m started at a value of 1 and was not constrained, i.e. used infinite bounds.

The fitting of the models in Equation (6.1), or (6.3) respectively, to the time domain data of BHD1 was done using Matlab's 'lsqcurvefit' function. As already described in Section 3.2.1, the amplitudes of the two quadrature components p_{sc} and x_{sc} were different and depended on the total extra path length for the scattered light. For this reason, the amplitude A_x of the scatter disturbance in the amplitude quadrature measurement needed to be determined in a separate fit. The parameters found in the first fit were

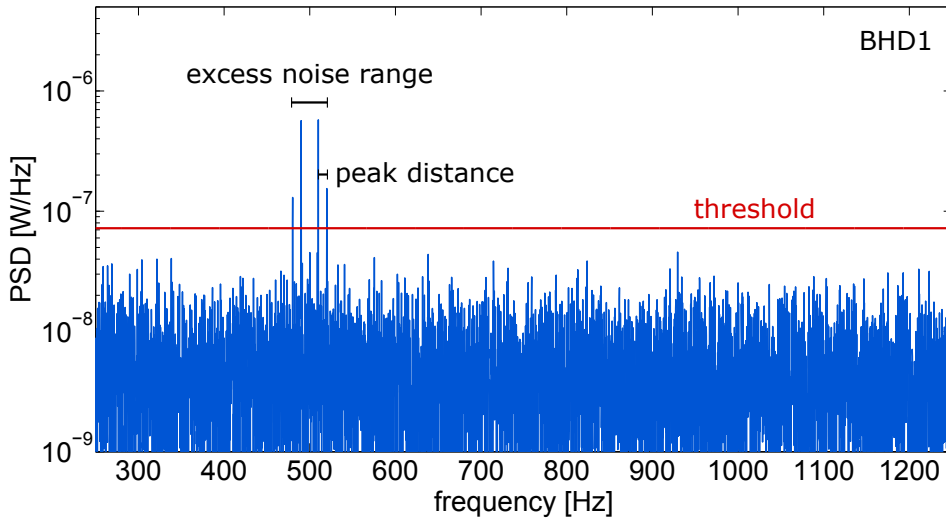


Figure 6.4.: Analyzing the scatter disturbance in the phase quadrature data of BHD1. The plot shows the power spectral density (PSD) of the measurement data from BHD1, computed for the whole data set of 5 s length. A threshold was applied to find the scatter disturbance and determine the frequency range that was polluted by this excess noise. The excess noise was analyzed to provide reasonable start parameters and boundaries for fitting the model of Equation (6.1), or (6.3) respectively, to the time domain data of BHD1.

inserted in the model for the orthogonal projection (Equation (6.2) or (6.4) respectively) and the amplitude A_x was obtained by fitting to the time domain data of BHD2 directly. Subtraction of the fitted models from the measurement data of BHD1&2 led to the results presented in the next section.

6.1.4. Subtraction of the scatter disturbance

The results for the subtraction of the monochromatic scatter disturbance are given in Figure 6.5. Shown are the averaged power spectral densities (PSD) of the original measurement data from BHD1&2 in blue and after subtraction of the fitted scatter models in red. The measurement at BHD1 contains only the disturbance signal at 500 Hz, while the measurement at BHD2 shows the disturbance and the GW-like signal at 1 kHz. The underlying noise floor in both measurements was set by optical shot noise. After subtraction of the scatter model, the disturbance clearly vanished in both measurements, while the GW-like signal and the surrounding noise floor were unaffected. The parameters obtained in the fits are given in Table 6.1 and are consistent with the injected disturbance signal.

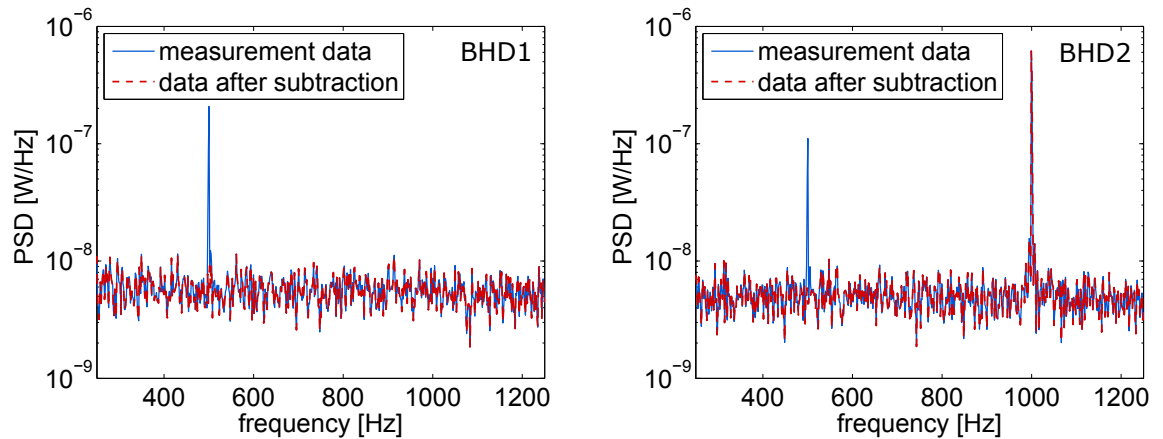


Figure 6.5.: Subtraction of the scatter disturbance – simple peak. Shown are the averaged power spectral densities (PSD) of the original measurement data from BHD1&2 in blue and after subtraction of the fitted scatter models in red. Note that the frequencies on the x-axis correspond to demodulated frequencies from the MHz regime.

A_p [mV]	f [Hz]	ϕ [rad]	A_x [mV]
0.9783	500.0146	3.9818	0.7212

Table 6.1.: Fitted parameters for the scatter peak.

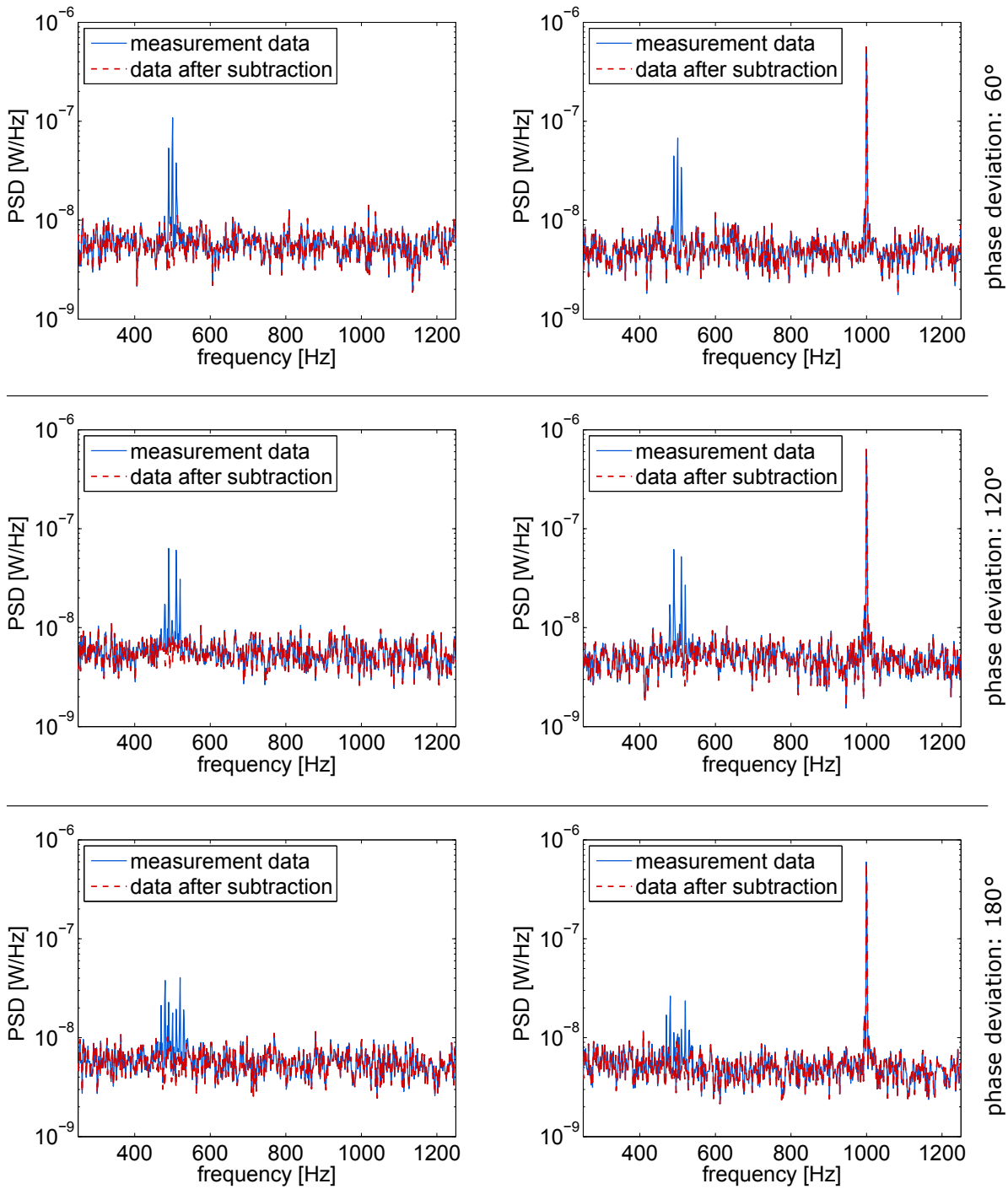


Figure 6.6.: Subtraction of the scatter disturbance – peak with surrounding sideband structure. The plots show the averaged PSD of the the original measurement data at BHD1&2 in blue and the same data after subtraction of the scatter disturbances in red. The three different measurements were performed with different modulation depths for the 10 Hz modulation, corresponding to a maximum phase deviation of 60°, 120° and 180° for the 500 Hz signal. Note that the frequencies on the x-axis correspond to demodulated frequencies from the MHz regime.

	A_p [mV]	f [Hz]	ϕ [rad]	m [rad]	f_m [Hz]	ϕ_m [rad]	A_x [mV]
ph. dev. 60°	0.9203	500.0123	3.7171	-1.0216	10.0038	2.6035	0.7956
ph. dev. 120°	-0.8357	500.0141	2.5619	2.0942	10.0019	3.0070	-0.7971
ph. dev. 180°	0.8356	500.0019	2.2331	3.0848	9.9981	2.4644	0.6156

Table 6.2.: Fitted parameters for the scatter peak with sideband structure.

The results of the subtraction for the scatter peak at 500 Hz with surrounding sideband structure from the additional phase modulation at 10 Hz are given in Figure 6.6. The plots show again the averaged PSD of the original measurement data at BHD1&2 in blue and the same data after subtraction of the scatter disturbances in red. The three different measurements were performed with different modulation depths for the 10 Hz modulation, corresponding to a maximum phase deviation of 60° , 120° and 180° for the 500 Hz signal. With increasing modulation depth, the sideband structure became broader and broader. The GW-like signal was the same in all measurements. Again, the disturbances could be completely subtracted, leading to a shot noise limited sensitivity over the whole frequency range. The parameters found in the fits of the respective measurements are given in Table 6.2. The modulation frequencies f and f_m , as well as the modulation depths m for the 10 Hz modulation, are in good agreement with the injected signal frequencies and the applied phase deviations. Note, that the modulation depths $m > 1$ in this experiment do not correspond to an actual motion of the scatter source over more than one wavelength. The 10 Hz modulation was applied to the 500 Hz signal *before* it was put on the piezo actuated mirror.

6.1.5. Discussion

In the experiments of this section I investigated scatter disturbances from a source with small amplitude motion where the motion of the source coupled linearly to the disturbance signal. The disturbances in the phase quadrature measurements could be sufficiently well described by the linearized models of Equations (6.1) and (6.3) and were completely removed from the measurement data. However, using the linearized models, the amplitude of the disturbance signals in the amplitude quadrature measurements could not be inferred from the phase quadrature models. Only an extended description, including (at least) the DC and $2f$ components could reveal the orientation of the disturbance signals in quadrature space. Determining an exact DC offset is generally difficult and the $2f$ components are supposed to be very small since they are of second order in the modulation index ($m \ll 1$ here contained in A_x and A_p). In the given analysis the amplitude of the projected disturbances had to be determined separately, from the amplitude measurement data. This procedure might be suitable if a disturbance has a distinct time-frequency behavior which can be recognized in both quadrature measurements.

6.2. Broadband scatter shoulder

This section is concerned with the case of a so-called ‘scatter shoulder’ that is produced by back-scatter sources with large amplitude motion. This type of disturbance was already introduced in Section 1.3 and is described in detail in Section 3.2.2. The experimental generation of the scatter shoulder and a GW-like reference signal with the Michelson interferometer will be described in Section 6.2.1. In Section 6.2.3 I will discuss the post-processing of the data and the results for the subtraction of the disturbance will be given in Section 6.2.4. The work presented in this section has been published in *Classical and Quantum Gravity* [59].

6.2.1. Experimental generation of the test signals

The experimental generation of the test signals is depicted in Figure 6.7. The optical setup used here was the same as the one employed in Section 6.1. Again, one scatter disturbance and one GW-like reference signal were produced in a table-top Michelson interferometer. This time, both signals had a distinct time-frequency behavior and the broadband scatter disturbance was supposed to conceal the GW-like signal. Both signals were shifted to the MHz regime and demodulated again after detection at the balanced homodyne detectors BHD1&2 in the split interferometer output. The GW-like signal

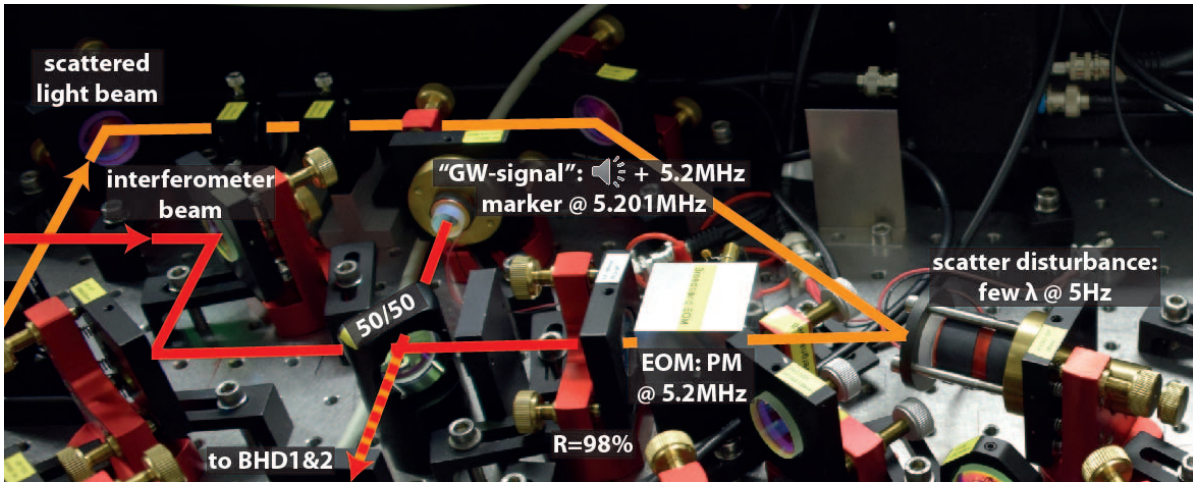


Figure 6.7.: Experimental generation of the test signals. The photo shows the table-top Michelson interferometer that was used to generate the test signals (red beam). A GW-like signal, due to a differential arm length change, was produced by modulating one piezo actuated interferometer end mirror with a sound file [60]. The scatter disturbance was generated with an external beam (orange) that was injected through the second interferometer end mirror, which had a reduced power reflectivity of $R = 98\%$. The phase of the beam was modulated over several wavelengths to produce a broadband disturbance via frequency up-conversion. PM: phase modulation, EOM: electro-optic modulator, BHD: balanced homodyne detector.

from Section 6.1, a narrow peak at (demodulated) 1 kHz, was still being generated with one of the interferometer end mirrors in this experiment but served solely as a marker to adjust the quadrature orientation of the dual homodyne readout with respect to the interferometer signal. The data were acquired and processed as described in Section 5.4.

The scatter signal

To artificially produce a scatter shoulder according to Equations (3.6)-(3.8), an external beam (orange) was injected through one of the interferometer end mirrors with a power reflectivity of $R = 98\%$. The phase of the beam was modulated with a piezo actuated mirror that had a shifting range of $30 \mu\text{m}$ at 1 kV. The piezo actuator was driven sinusoidally with roughly 300 Vpp at a frequency of 5 Hz to achieve a path length change of a few wavelengths $\lambda = 1064\text{nm}$. The large shifting range led to frequency up-conversion of the 5 Hz modulation and produced a broadband scatter shoulder that limited the sensitivity of the interferometer over a bandwidth up to about 200 Hz (demodulated frequency). The center of motion of the piezo actuated mirror was not stabilized but turned out to be sufficiently constant over the measurement time. An additional phase modulation at 5.2 MHz was imprinted by an electro-optic modulator (EOM) to shift the scatter signal into the MHz range.

The GW-like signal

The GW-like signal was produced with the same interferometer end mirror as in Section 6.1. As already mentioned above, the signal had a distinct time-frequency dependence in this experiment. I used a sound file containing about 4.5 seconds of a simulated inspiral of two neutron stars with equal masses [60] that I fed into an Agilent 33500B series waveform generator as an external modulation. The signal described a chirp that started at about 55 Hz and increased in frequency over time up to the kHz regime. It is depicted in Figure 6.8, once in time domain (left) and once in a spectrogram (right).

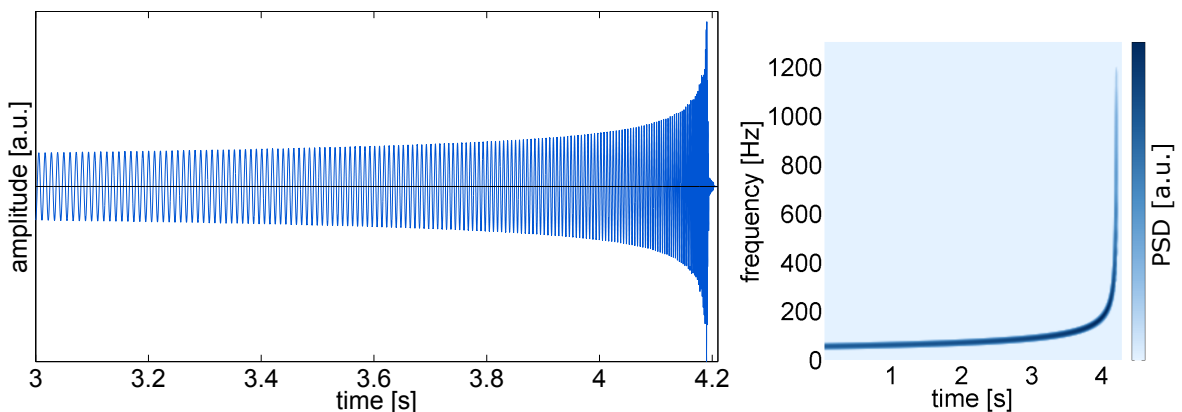


Figure 6.8.: Injected GW signal. The sound file contained about 4.5 seconds of a simulated inspiral of two neutron stars with equal masses [60]. The two plots show a segment of the signal in time domain (left) and the whole signal in a spectrogram (right).

The waveform generator shifted the audio band signal by 5.2 MHz before it was put on the piezo actuator. A natural resonance of the piezo mounted interferometer end mirror at about 5.2 MHz was exploited to generate a sufficiently large signal in this high frequency regime without producing too much electronic pick-up. In the relevant kHz range around this resonance the transfer function of the piezo was still flat, so that the injected audio band signal was not distorted in the measurement.

6.2.2. Stabilization of the dual homodyne readout

This experiment employed a simplified version of the locking scheme for the quantum-dense readout described in Section 5.3. The stabilization of the homodyne detectors was done using the phase modulated control beams of the squeezed light sources OPA1&2 which were introduced in Section 5.2. Note, that there was no squeezing produced in this experiment. As described in Section 5.3, the two control fields were overlapped on a 50/50 beam splitter and their relative phase shift was stabilized to an angle of 90° ①. The error signal for this lock was obtained by measuring the difference of both beam splitter outputs with a power pick-off of 1% each. One of the beam splitter outputs was sent to the 50/50 beam splitter in the interferometer output and overlapped with the interferometer signal while the second output was dumped in this experiment. Demodulation of the homodyne signals, each at one of the phase modulation frequencies, enabled locking the two detectors BHD1&2 into orthogonal quadratures ②. The quadrature ori-

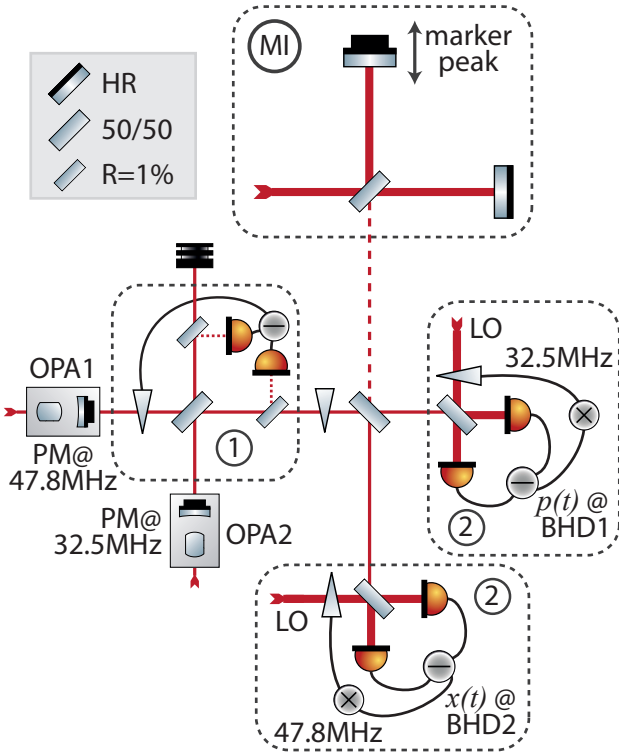


Figure 6.9: Locking scheme for the dual homodyne readout. In this setup, the phase modulated control beams of the squeezed light sources OPA1&2 were employed for the stabilization of the dual homodyne readout (no squeezing was generated). First the two fields were locked 90° out of phase ① and afterwards the readout quadratures at BHD1&2 were locked each with respect to one of the control beams ②. The phase space orientation of the readout quadratures with respect to the interferometer signal was adjusted by minimizing a marker peak in the spectrum of BHD1. MI: Michelson interferometer, HR: high-reflectivity mirror, OPA: optical parametric amplifier, PM: phase modulation, BHD: balanced homodyne detector, LO: local oscillator.

entation of the detectors with respect to the interferometer signal was not electronically stabilized in this experiment but adjusted by minimizing the injected marker peak at 1 kHz in the live spectrum of BHD1.

6.2.3. Post-processing of the scatter limited measurement data

A spectrogram plot of the scatter limited measurement data from the two detectors is shown in Figure 6.10(a). In the phase quadrature measurement of BHD1 (left) only the disturbance signal from the artificial scattering is visible. It shows up as the typical arches, already discussed in Section 3.2.2. The amplitude data of BHD2 (right) shows the scatter disturbance concealing part of the injected GW-like signal (chirp), only its ‘tail’ towards high frequencies is clearly visible. In Figure 6.10 (b) the averaged power spectral

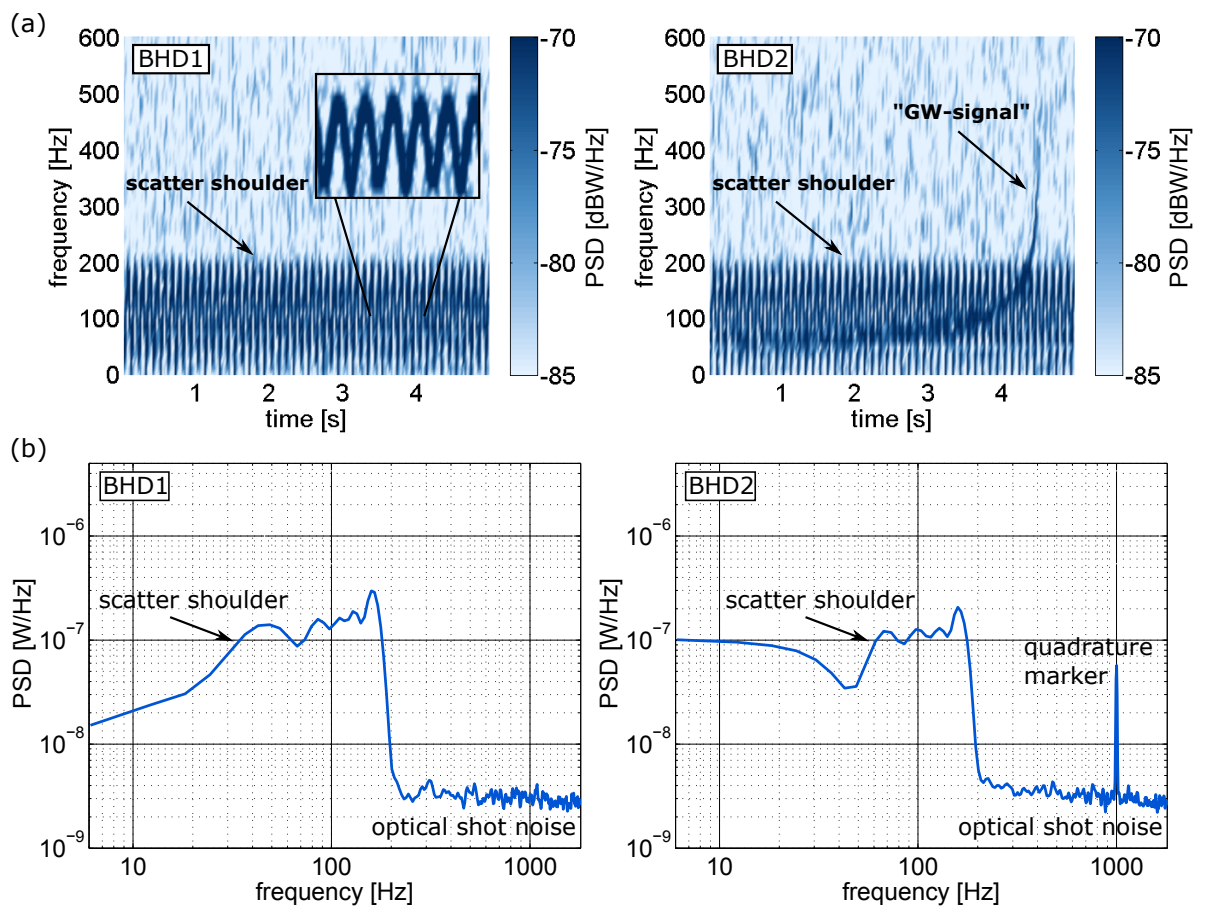


Figure 6.10.: Scatter limited data. (a) Spectrogram of the measurement data from BHD1&2. The time resolved scatter shoulder (arches) is visible in both quadrature measurements. In the amplitude data of BHD2 it is concealing the simulated gravitational-wave signal (chirp) that was injected from an audio file [60]. (b) Averaged power spectral density of the same data. The scatter shoulder is the dominant noise source for frequencies below about 200 Hz. Above, the measurements were limited by optical shot noise.

density (PSD) of the data is shown. The scatter shoulder is clearly the dominant noise source for frequencies below about 200 Hz. Above that frequency the measurements were limited by optical shot noise. The peak at 1 kHz in the spectrum of BHD2 shows the earlier mentioned marker that was used to adjust the quadratures of the dual homodyne readout. The injected GW signal can not be identified in this plot, only a slight rise of the noise floor at the edge of the scatter shoulder of BHD2 is visible.

The post-processing was done in Matlab again. For convenience, the equations of Section 3.2.1 which are relevant for fitting the scatter disturbance are given here again. For a scatter source which performs a sinusoidal motion with constant parameters, the projections of the disturbance signal in the phase and amplitude quadratures are given by

$$p_{\text{sc}}(t) = A \cdot \cos(\varphi_0 + m \sin(2\pi f_m t + \phi_m)) \quad (6.5)$$

$$x_{\text{sc}}(t) = A \cdot \sin(\underbrace{\varphi_0 + m \sin(2\pi f_m t + \phi_m)}_{\equiv \varphi(t)}) \quad (6.6)$$

with the signal amplitude A , a constant overall phase shift φ_0 which accounts for the total mean path length that the back-scattered beam traveled outside the interferometer and the modulation depth m , frequency f_m and phase ϕ_m of the scatter source motion. For large amplitude motion with $m > 1$, the Doppler shift of the back-scattered light is useful to describe the time-frequency behavior of the disturbance signal

$$f_{\text{ds}}(t) = m f_m \cos(2\pi f_m t + \phi_m) \quad . \quad (6.7)$$

To fit the scatter model of Equation (6.5) to the phase quadrature data of BHD1, a suitable set of start parameters was required in advance. I assumed no prior knowledge about the parameters of the scatter source and therefore, in a first step, I tried to reduce the set of required parameters.

The course of the arches showing up in the spectrogram of Figure 6.10 is described by the Doppler shift of Equation (6.7) and solely depends on the frequency f_m , modulation depth m and phase ϕ_m of the scatter source motion. It could therefore be used to fit these parameters separately. The spectrogram consists of a number of spectra, computed for different consecutive (overlapping) data segments at different times. Finding the frequency component with the maximal amplitude in each of these led to the black data points in Figure 6.11. A fit of the absolute value of Equation (6.7) to the data points is given by the blue trace in Figure 6.11. During the fitting process, at first, f_m was iterated from a trial frequency vector while m and ϕ_m were fitted using Matlab's 'lsqcurvefit' function in each step. The spectrogram and the corresponding maximal frequency components (black data points in Figure 6.11) were computed separately for each frequency f_m because the resolution of the spectrogram had to be adjusted to optimally resolve arches at a certain modulation frequency. The start parameters used here were $[m = 1; \phi_m = 0]$ and the boundaries were set to $[m = \pm\infty; \phi_m = \pm 2\pi]$. The fit with the minimal residual was used as a first rough estimate of the three parameters and to determine the resolution required for the spectrogram. To improve the estimate,

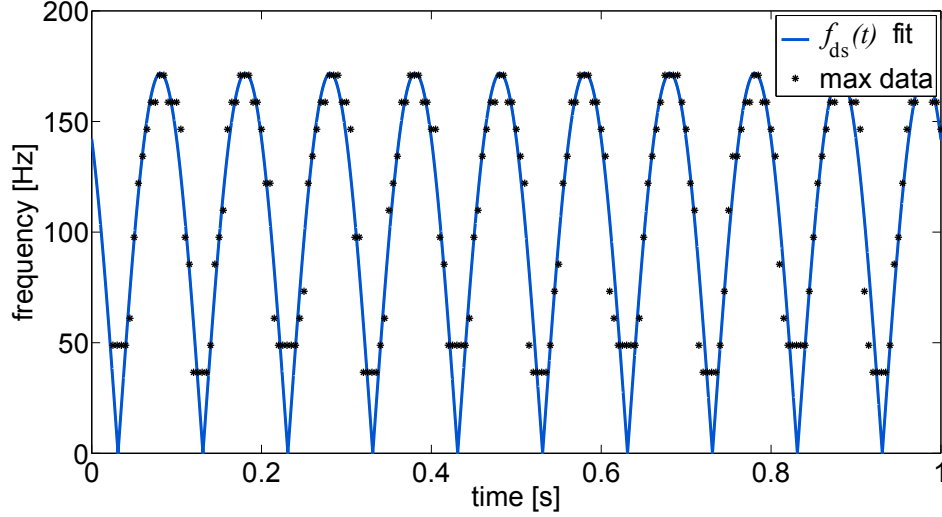


Figure 6.11.: Fitting the Doppler shift of the back-scattered light. A first estimate for a reduced parameter set $[m, f_m, \varphi_m]$ was deduced from the time dependent Doppler shift of the back-scattered light. The black dots describe the arches in the spectrogram data of BHD1 (see Figure 6.10 (a)) and the fitted Doppler shift $f_{ds}(t)$ according to Equation (6.7) is given by the solid blue trace.

m [rad]	f_m [Hz]	ϕ_m [rad]
34.4215	4.9994	-2.5097

Table 6.3.: Fitted parameters for the time dependent Doppler shift.

another fit was performed with all three parameters free. The result of this second fit is the one depicted in Figure 6.11 and returned the parameters given in Table 6.3.

As a next step, the full model of Equation (6.5) was fitted to the time series data of BHD1. To improve the speed of this fit, the data was first downsampled by averaging neighboring data points (and filtered accordingly). The reduced sample rate was set to sufficiently resolve the maximum Doppler shift frequency $f_{ds}^{max} = mf_m$ determined from the first fit. A segment of the averaged time data is displayed in gray in Figure 6.12 (a). Again, Matlab's 'lsqcurvefit' function was used for the fitting. The parameters of Table 6.3 were used as start parameters together with half of the maximum detected amplitude as starting point for the signal amplitude A and $\varphi_0 = 0$. The boundaries were set to span the whole reasonable parameter space. The result of the fit is given by the dashed black trace in Figure 6.12 (a) and the corresponding parameters are given in Table 6.4.

A [mV]	φ_0 [rad]	m [rad]	f_m [Hz]	ϕ_m [rad]
-6.3174	-0.0759	34.1784	5.0001	-2.4997

Table 6.4.: Fitted parameters for the harmonic scatter model.

Although the fit already reproduced the scatter disturbance quite well it became clear

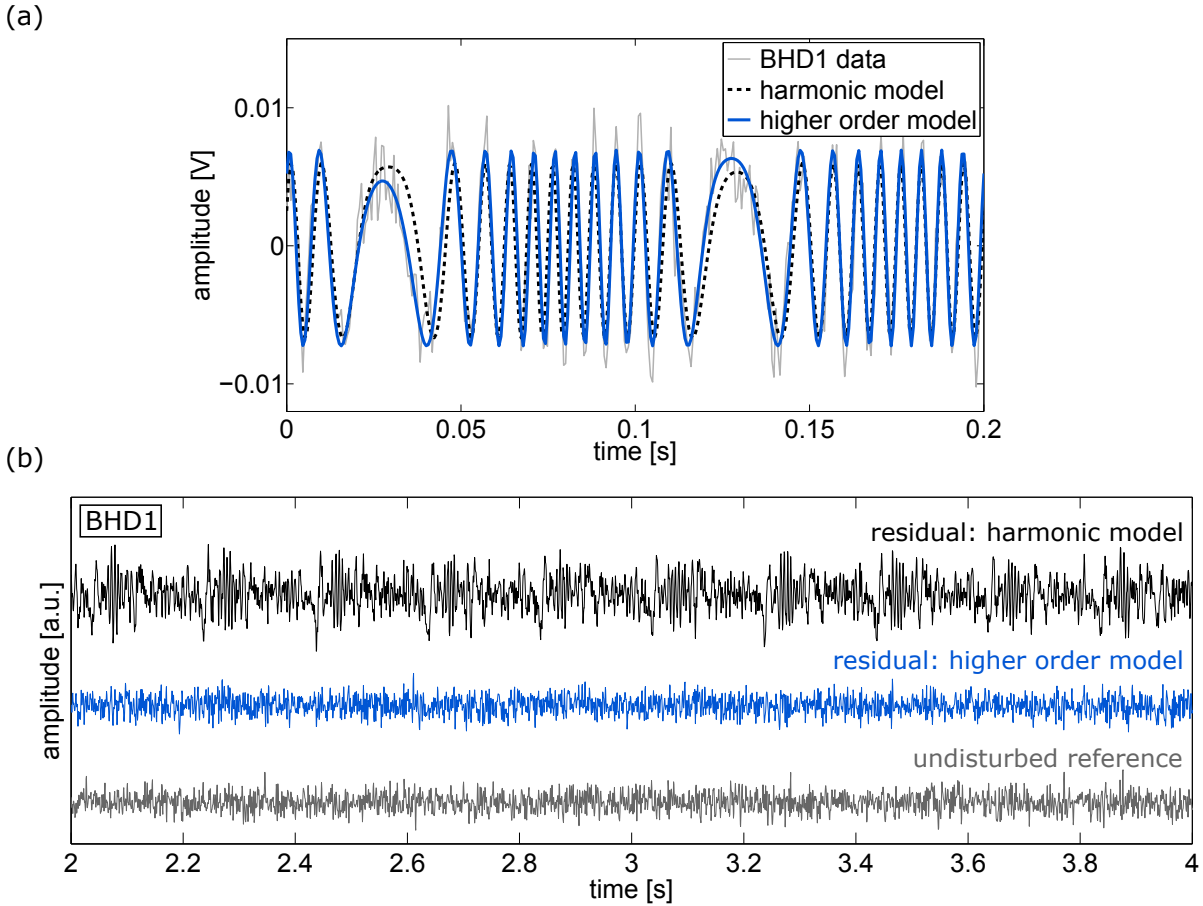


Figure 6.12.: Fitting the phase quadrature data. (a) shows an averaged segment of the time domain data measured at BHD1 (gray) overlaid with fits of the harmonic model (dashed black) and the higher order model (solid blue). (b) shows the residuals of a larger data segment after subtraction of the modeled disturbance signals (black and blue) in comparison with an undisturbed reference measurement, taken while the scattered light beam was blocked.

that the model was not perfectly matching the data. Especially around the turning points of the piezo actuator, which appear at about 0.03s and 0.13s in the plot, there was a quite strong deviation from the harmonic model of Equation 6.5. To account for the nonlinear response of the piezo to the driving sine wave, I included higher harmonics of the scatterer's oscillation frequency f_m (up to the 5th order) in the model for the time dependent phase shift in Equations (6.5) and (6.6)

$$\varphi(t) = \varphi_0 + \sum_{n=1}^5 m_n \sin(2\pi f_m t + \phi_{m,n})^n \quad . \quad (6.8)$$

I performed a second fit using this higher order model. For the higher order contributions in $\varphi(t)$ I provided different sets of randomly distributed starting phases

$\phi_{m,n>1} \in [-2\pi, 2\pi]$ and modulation depths $m_{n>1} \in [-m_1/10, m_1/10]$ and used Matlab's 'MultiStart' to run the solver from multiple start points.

All boundaries were chosen to span the whole reasonable parameter space again. The solid blue trace in Figure 6.12 (a) shows the resulting fit for the higher order model and the corresponding parameters are given in Table 6.5. The modulation depth found in the fit corresponds to a total path length change for the scattered light beam of $m_1\lambda/\pi \approx 11\lambda$ which is in line with the specifications of the piezo actuator for the applied voltage. Also the modulation frequency of 5 Hz was correctly reproduced and the higher order contributions were found to be consistent for several data sets.

	A [mV]	φ_0 [rad]	m_1 [rad]	f_m [Hz]	$\phi_{m,1}$ [rad]
	-7.0617	-0.3761	34.6087	5.0001	-2.4792

order n	2	3	4	5
m_n [rad]	0.5772	-1.1283	0.0349	0.8284
$\phi_{m,n}$ [rad]	3.1525	-1.5956	-1.0960	2.8555

Table 6.5.: Fitted parameters for the higher order scatter model.

The residuals of the fits for the harmonic (black) and the higher order model (blue) are shown in Figure 6.12 (b) for a larger segment of time domain data. The gray trace shows a reference measurement that was taken while the scattered light beam was blocked. Since the injected GW-like signal does not project into the phase quadrature measurement the reference measurement shows solely optical shot noise.

In the residual of the harmonic model there is clearly some signal remaining, while there is no structure recognizable in the residual of the higher order model. To quantify the accuracy of the subtraction I computed the average powers remaining in the residuals for the frequency range from f_m to f_{ds}^{\max} where the scatter disturbance was dominant and compared them to the band power of the reference measurement. For the computation I used Matlab's 'bandpower' function. For the higher order model the difference between the residual and the reference measurement was $2.04 \cdot 10^{-8}$ W. This difference is well explained by the different optical shot noise contributions in the two measurements since the standard deviation in band power for a set of vacuum measurements at BHD1 was determined to be $5.97 \cdot 10^{-8}$ W. For the linear model in contrast, the difference between the residual and the reference was $3.70 \cdot 10^{-6}$ W which is still about a factor of 60 larger than the standard deviation of the vacuum measurements.

At last, the projection of the disturbance into the amplitude measurement of BHD2 needed to be computed. Ideally, this would be achieved by inserting the higher order phase shift of Equation (6.8) into the model for the amplitude quadrature of Equation (6.6) with the obtained parameter set of Table 6.5. Though the signal amplitude of the scatter disturbance A should be the same in both quadrature projections, this was not the case here due to differences in the two detection paths. Also, the angle of the measured quadratures between the two detectors turned out to be not exactly 90° , which demanded for an additional constant phase parameter in Equation (6.6).

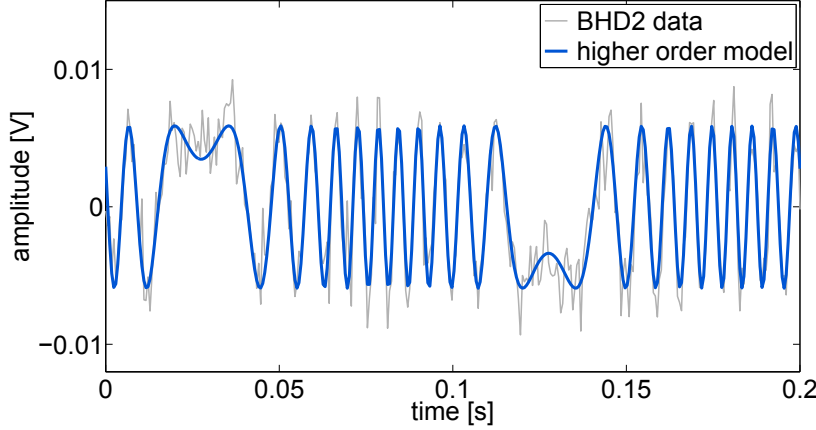


Figure 6.13.: Projection of the scatter model in the amplitude quadrature. The plot shows an averaged segment of the amplitude quadrature data measured at BHD2 (gray) overlaid with the projected, modeled disturbance signal (blue).

In contrast to the case discussed in Section 6.1, the different amplitudes of the disturbance signal at the two detectors are due to differences in the experimental setup and are not a property of the scatter disturbance. Both, the scaling and the quadrature angle between the detectors, could in principle be characterized in advance or monitored during measurements for a real GW detector. Here, the amplitude of the disturbance in the amplitude quadrature projection and the quadrature offset were fitted again using the data of BHD2 directly. All other parameters were fixed to the values given in Table 6.5. The result of this fit was $A = -5.9106 \text{ mV}$ for the amplitude and $\varphi_{\text{offset}} = -0.1909 \text{ rad} \equiv -10.9^\circ$ for the quadrature offset. The final model for the amplitude quadrature is shown in blue in Figure 6.13 together with a segment of the averaged measurement data from BHD2 (gray).

6.2.4. Subtraction of the scatter disturbance

A segment of the amplitude quadrature data of BHD2 after subtraction of the higher order model for the scatter disturbance is shown in Figure 6.14 (a) (blue), together with an undisturbed reference measurement of the amplitude quadrature (gray) that contains solely the GW-like signal. The scattered light beam was blocked in the setup during this reference measurement. In both traces the injected chirp signal is already discernible.

To give a measure for the purity of the residual data after subtraction of the disturbance I compared the band powers again. The difference of the band powers of the residual and the reference measurement on the interval $[f_m, f_{\text{ds}}^{\text{max}}]$ was $-1.02 \cdot 10^{-8} \text{ W}$ and lay well within the standard deviation of $6.13 \cdot 10^{-8} \text{ W}$ for the differences of a set of vacuum measurements at BHD2.

For comparison with the scatter limited data of Figure 6.10 the data of both detectors after subtraction of the disturbance is shown again in frequency domain in Figure 6.14 (b) and (c). Note, that all frequencies shown here correspond to demodulated fre-

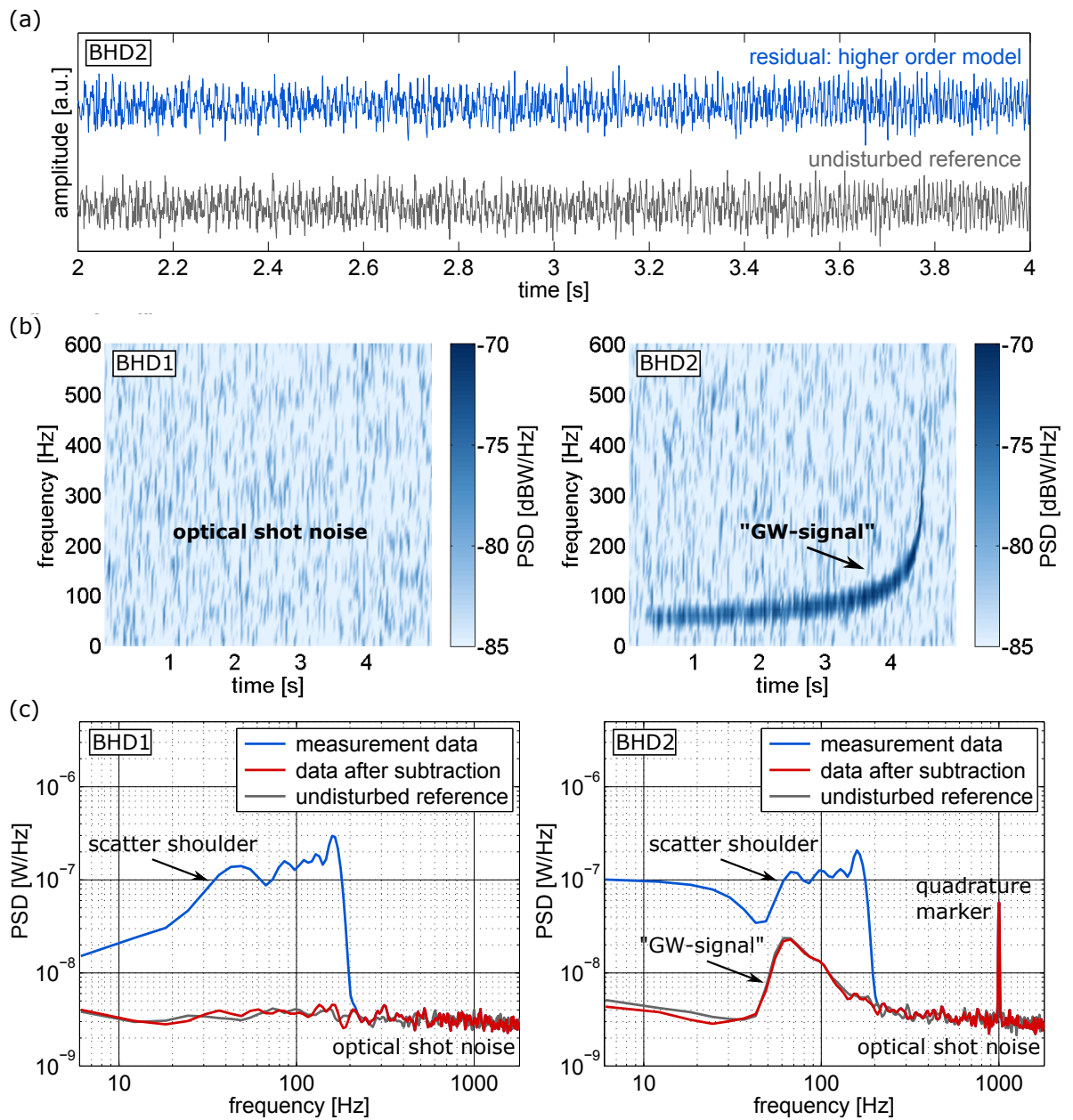


Figure 6.14.: Results after subtraction of the scatter model. (a) Residual of the amplitude quadrature measurement after subtraction of the higher order model for the scatter disturbance (blue) in comparison with an undisturbed reference measurement where the scattered light beam was blocked (gray). (b) Residual data of both quadrature measurements after subtraction of the scatter disturbance in a spectrogram. (c) Averaged power spectral density (PSD) of the residual data (red) in comparison with the original measurement data containing the disturbance (blue) and the undisturbed reference measurement (gray). Note, that all frequencies shown here correspond to demodulated frequencies from the MHz regime.

quencies from the MHz regime. In Figure 6.14 (b) the arches in the spectrogram data vanished completely and the injected GW signal could be clearly recovered in the amplitude quadrature measurement. Figure 6.14 (c) shows the averaged power spectral density (PSD) of the residual data after subtraction of the disturbance (red) in comparisons with the original measurement data containing the scatter shoulder (blue) and the above mentioned reference measurement without the scatter disturbance (gray). Also here, the shoulder completely vanished from the spectrum and the data after subtraction is in good agreement with the undisturbed reference measurement. In the frequency range below 200 Hz, where the data was dominated by the scatter disturbance, a noise reduction of more than one order of magnitude was achieved. The final sensitivity of the measurement was limited by optical shot noise over the whole frequency range.

6.2.5. Discussion

In this section I demonstrated the subtraction of a broadband scatter shoulder, which was generated by a scatter source performing a sinusoidal motion with a large amplitude motion of a few wavelengths. The disturbance signal could be successfully modeled by including higher harmonics of the scatter source motion in the sinusoidal model of Equations (6.5) and (6.6).

The fitted parameters show that the signal amplitudes in the two quadrature measurements differed quite a lot though they should in principle be the same. Their ratio was found to be about the same for the measurements of Section 6.3 and Chapter 7. Its mean value was $A_p/A_x \approx 1.15$. As already mentioned in Section 6.2.3, this was probably attributed to differences in the two detection paths, though I was not able to clarify where exactly the difference came from. Since the vacuum fluctuations measured at the two detectors differed only by about 1%, differences in the local oscillator powers or in the electronic gain of the two detectors could be ruled out as cause. A misalignment on the beam splitter in the interferometer output might have caused an unbalanced splitting of the signal. The measured amplitude ratio would correspond to a splitting ratio of about 53.5/46.5. This could not be verified due to changes in the optical setup that were made before the results of the modeling were achieved.

Another feature revealed by the fit was a quite big quadrature offset from the aimed at 90° between the two detectors. Its value was also similar for the named experiments and its mean value was $\varphi_{\text{offset}} \approx 9.2^\circ$. The reason for this offset might also lie in an imperfect splitting ratio, here, at the beam splitter where the control beams for the quadrature locks of the balanced homodyne detectors were combined (see Figure 6.9 ①). As described in Section 6.2.2 the two control beams were supposed to be stabilized to a relative phase shift of 90° with the help of the difference photo current measured in the two beam splitter outputs. For a balanced splitting, a 90° phase shift corresponds to the point where the power in both beam splitter outputs is exactly the same, independently of the powers of the individual control beams. For an unbalanced splitting however, the individual powers do play a role and could have caused the mentioned phase offset. The slightly varying values of the phase offset for the different measurements could then be attributed to small differences in the powers of the control beams.

6.3. Scatter shoulder with multiple round trips

The measurements presented in this section were chronologically performed before the measurements of the last two sections. They followed the QDM measurement [33] and used a similar cavity to produce the scatter disturbance (only with a different piezo actuator and an additional EOM in the cavity). It was my first approach to produce a scatter shoulder but the cavity effect of multiple round trips made the scatter disturbance more difficult to model and I decided to start with simpler cases shown in the last sections. The measurements were not completely optimized, the quadrature orientation of the detectors was not ideal and they were made before the implementation of the automatized sound output with triggered measurement, so there are no GW-like reference measurements without scattering available for comparison.

Nevertheless, the scatter shoulder with multiple round trips constitutes an interesting and realistic case for scatter sources. During Virgo’s second science run a scatter shoulder with a ‘double bounce’ was observed that originated from back-scattering of the optical bench behind one of the interferometer end mirrors (WEB) during high seismic activity [29]. This scenario is already quite close to the experiment presented here.

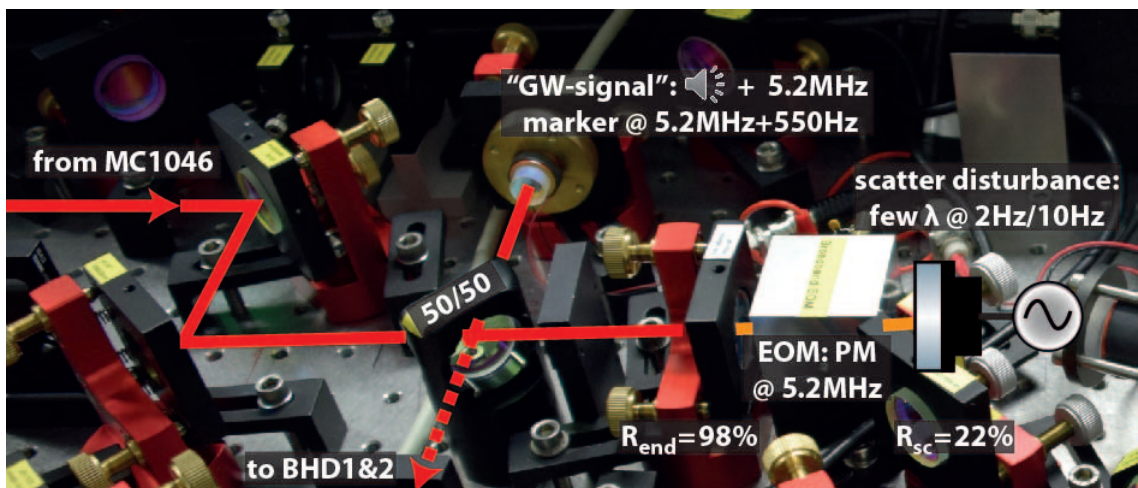


Figure 6.15.: Experimental generation of the test signals. The photo shows the table-top Michelson interferometer that was used to generate the test signals. A GW-like signal, due to a differential arm length change, was produced by modulating one piezo actuated interferometer end mirror with a sound file [60]. The scatter disturbance was generated by back-reflecting part of the light that leaked through the second interferometer end mirror, which had a reduced power reflectivity of $R_{\text{end}} = 98\%$. The back-scatter mirror had a power reflectivity of $R_{\text{sc}} = 22\%$ and was modulated over several wavelengths to produce a broadband disturbance via frequency up-conversion. The low finesse cavity formed between the end mirror and the back-scatter mirror led to multiple round trips for the back-scattered light. PM: phase modulation, EOM: electro-optic modulator, BHD: balanced homodyne detector.

6.3.1. Experimental generation of the test signals

Figure 6.15 shows the table-top Michelson interferometer again. A GW-like reference signal was generated by modulating one of the interferometer end mirrors with the same chirp signal [60] already used in Section 6.2. The marker peak for adjusting the quadrature angles of the two balanced homodyne detectors (BHD1&2) was set to a (demodulated) frequency of 550 Hz in this experiment.

Instead of an external beam, this time the small amount of light that leaked through the interferometer end mirror with power reflectivity $R_{\text{end}} = 98\%$ was used to generate the scatter disturbance. The beam was modulated using a piezo actuated mirror with a power reflectivity of $R_{\text{sc}} = 22\%$ and partially back-reflected towards the interferometer. Similarly to Section 6.2, a sinusoidal signal at low frequencies and with a shifting range of a few wavelengths λ was applied to the piezo actuated mirror. Two measurements with modulation frequencies of 2 Hz and 10 Hz respectively were performed.

The two mirrors formed a low finesse cavity ($\mathcal{F} \approx 4$) leading to multiple round trips for the scattered light beam. A measurement of the light transmitted through this cavity

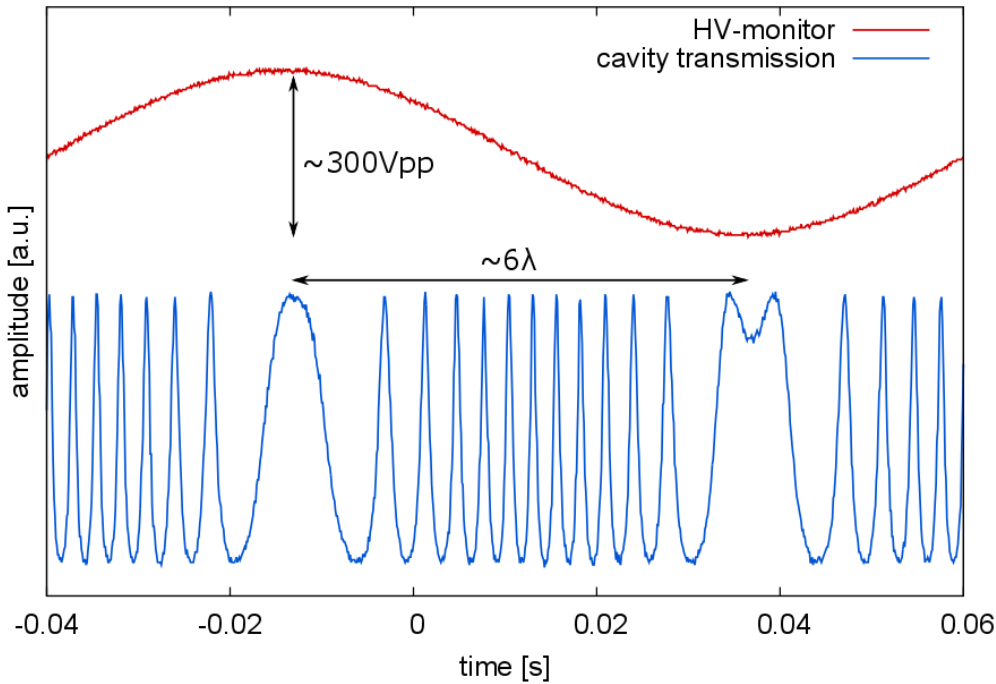


Figure 6.16.: Scatter cavity in transmission. The plot shows the output signal of the high voltage amplifier (HV) that was used to modulate the back-scatter mirror (red) and a measurement of the light that was transmitted through the back-scatter cavity during one oscillation period of the scatter source (blue).

during one oscillation period of the scatter source is shown in blue in Figure 6.16. As a reference, the red trace shows the output signal of the high voltage amplifier (HV) that was used to modulate the back-scatter mirror. Again, a voltage range of about 300 Vpp was employed, leading to a total shifting range of about 6λ , i.e. a total path length change of about 12λ for the back-scattered light from the foremost to the very back position of the back-scatter mirror.

An additional electro-optic modulator (EOM) inside the cavity shifted the scatter disturbance to the MHz regime again. The stabilization scheme for the dual homodyne readout was the same as described in Section 6.2.2.

6.3.2. Scatter limited measurement data

The scatter limited data measured at the two balanced homodyne detectors BHD1&2 is shown in Figures 6.17 and 6.18 for the scatter source moving at 2 Hz and 10 Hz respectively.

In the spectrograms of Figure 6.17 (a) the scatter disturbance at 2 Hz shows up as the typical arches again, but this time multiple rows of arches are visible. They correspond to the different round trips inside the low finesse cavity that was formed by the scatter source and the interferometer end mirror. The part of the light that stayed in the cavity saw the scatter mirror at approximately the same position (or speed respectively) again and per round trip the light was frequency shifted further and further according to the Doppler shift of Equation (6.7). In the spectrogram of the amplitude quadrature data measured at BHD2, also the quadrature marker at 550 Hz and parts of the injected GW-like signal are visible. The white background noise at both detectors was again given by optical shot noise.

In Figure 6.17 (b) the averaged power spectral density (PSD) of the data for the 2 Hz disturbance is shown (blue). Here, the different round trips appear as ‘steps’ in the scatter shoulder. The scatter disturbance was the dominant noise source up to a (demodulated) frequency of about 300 Hz, above that frequency the sensitivity was limited by optical shot noise. A reference measurement for the shot noise was taken with the signal ports of both detectors blocked and is shown in gray.

For the scatter disturbance at 10 Hz in Figure 6.18 the spectrograms in (a) do not ideally resolve the arches anymore since the frequency of the back-scattered light changes too quickly over time. The steps for the different round trips in the scatter shoulder of the averaged PSD in (b) are still visible though a slightly higher frequency resolution was chosen in these plots in order not to smear out the quadrature marker too much. The disturbance now covers the complete spectral range of the injected GW-like signal, up to the kHz regime. The otherwise limiting optical shot noise of the measurement is shown in gray again.

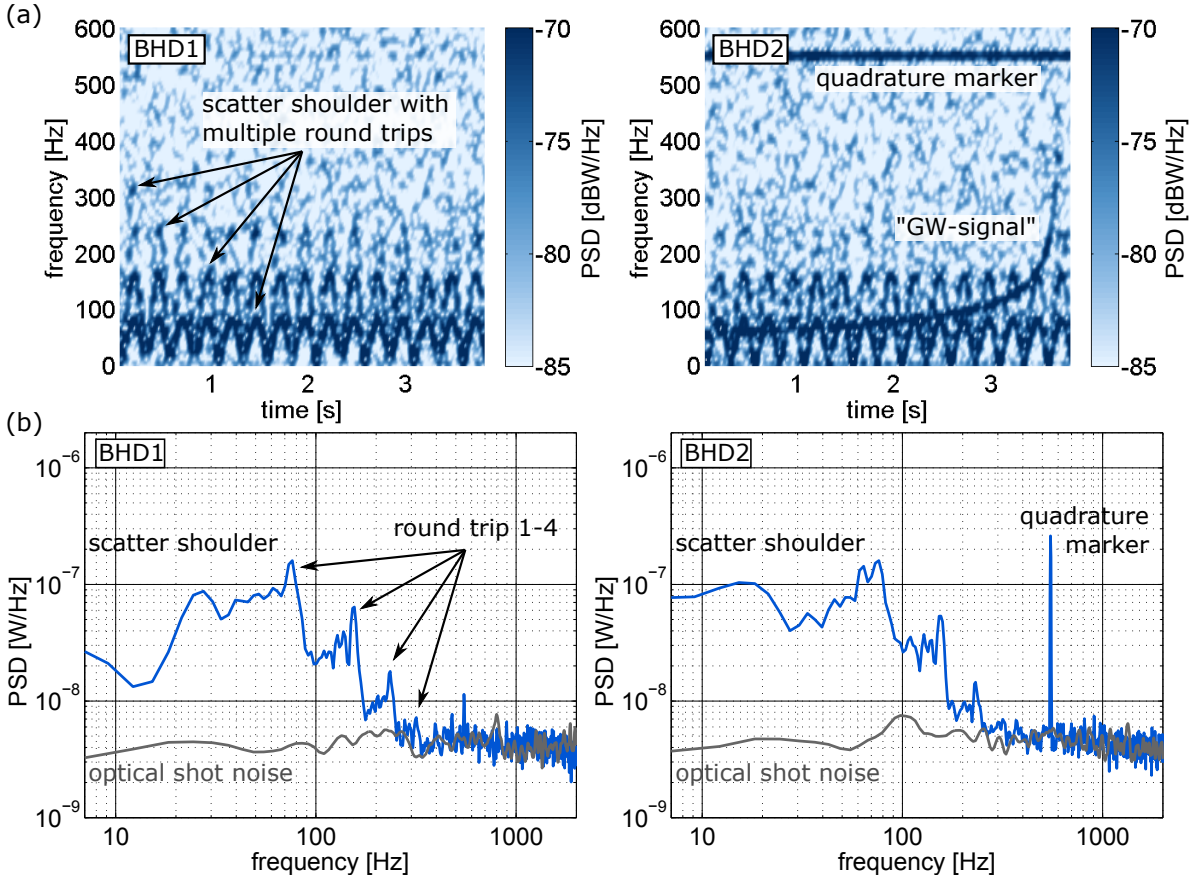


Figure 6.17.: Scatter limited measurements for the 2 Hz disturbance. (a) Spectrogram of the measurement data from BHD1&2 showing the time resolved scatter disturbance (arches) for multiple round trips of the back-scattered light between the scatter source and the interferometer end mirror. In the amplitude data of BHD2 the disturbance concealed the injected gravitational-wave signal (chirp) [60]. (b) Averaged power spectral density (PSD) of the same data (blue). The scatter shoulder was the dominant noise source for (demodulated) frequencies below about 300Hz and the different round trips show up as ‘steps’ in the shoulder. Above 300 Hz the measurements were limited by optical shot noise (gray).

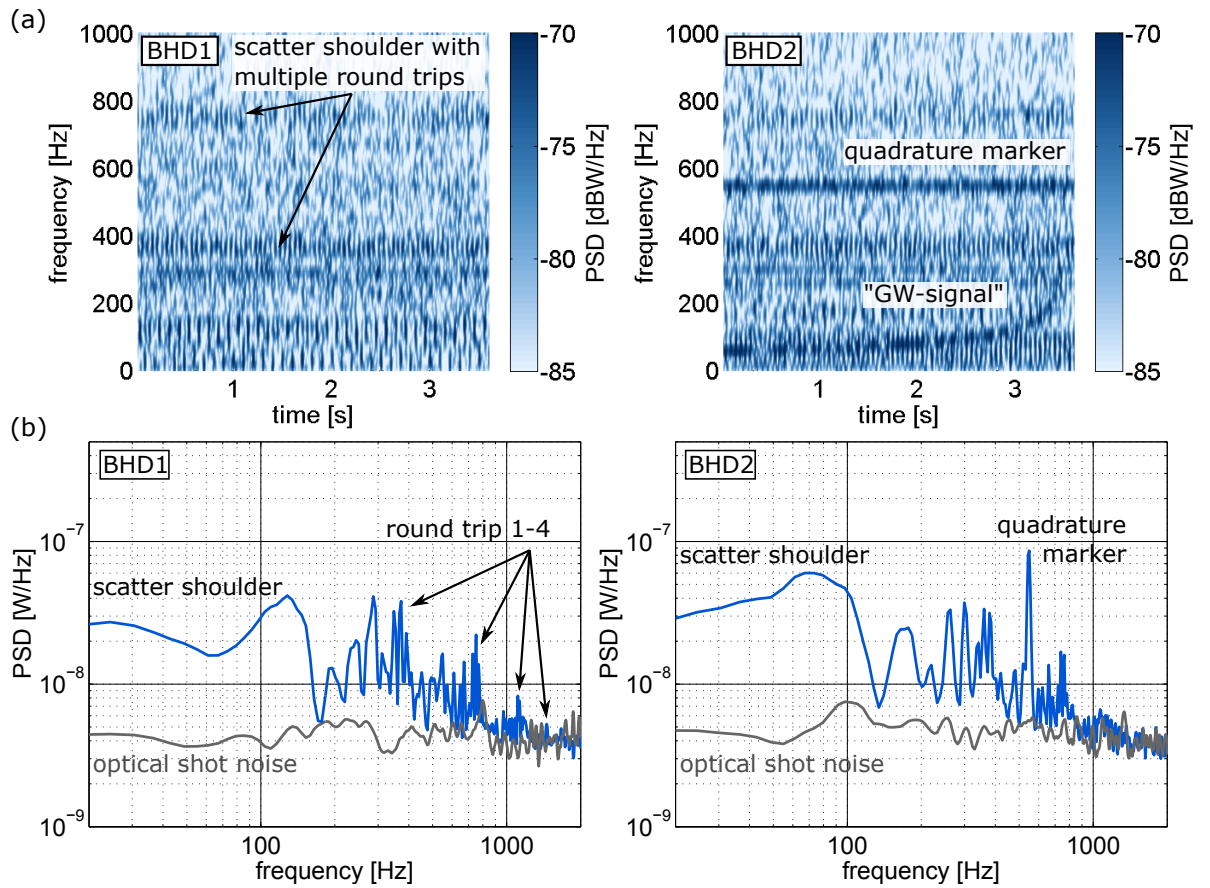


Figure 6.18.: Scatter limited measurements for the 10 Hz disturbance. (a) Spectrogram of the measurement data from BHD1&2 showing the scatter disturbance covering the whole spectral range of the injected gravitational-wave signal (chirp) [60]. (b) Averaged power spectral density (PSD) of the same data (blue) in comparison with the otherwise limiting optical shot noise in the measurement (gray).

6.3.3. Modeling and post-processing

To describe the back-scatter disturbance we are interested in the field which is back-reflected from the cavity formed by the interferometer end mirror with amplitude reflectivity ρ_{end} and the scatter mirror. All optical loss inside the cavity can be included in the effective reflectivity $\rho_{\text{sc}}^{\text{eff}}$ of the scatter mirror. The scenario is illustrated in Figure 6.19. The amplitude of the beam that first enters the cavity is denoted with A' and the phase shift due to the additional path per round trip for the scattered light is denoted with $\varphi(t)$ and depends on the motion of the scatter source/mirror. The amplitude of the scattered light beam is decreased by a factor of $\rho_{\text{sc}}^{\text{eff}}$ during each round trip. For all except the first round trip, the amplitude is further decreased by a factor ρ_{end} and an additional constant phase shift of π needs to be considered

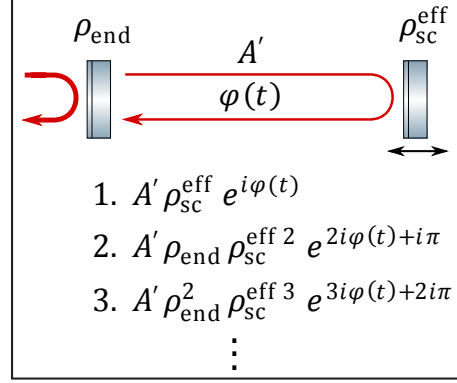


Figure 6.19.: Cavity round trips.

Summing up the fields and transmission through the interferometer end mirror leads to

$$E_{\text{sc}} = \underbrace{\sqrt{1 - \rho_{\text{end}}^2} \rho_{\text{sc}}^{\text{eff}} A'}_{=: A} \sum_{n=0}^{\infty} \underbrace{(\rho_{\text{end}} \rho_{\text{sc}}^{\text{eff}})^n}_{=: g} e^{in(\varphi(t) + \pi)} \quad . \quad (6.9)$$

Employing the geometric series for an infinite number of round trips, this simplifies to

$$E_{\text{sc}} = A e^{i\varphi(t)} / (1 - g e^{i(\varphi(t) + \pi)}) \quad . \quad (6.10)$$

The projections of the scatter disturbance in the phase quadrature and amplitude quadrature measurements are then proportional to the real and imaginary parts of E_{sc} .

In contrast to the scatter model of Equations (6.5)-(6.6), here, a shift of the mean position of the scatter source, i.e. adding a constant phase shift in $\varphi(t)$, is not equivalent to a simple rotation of the scatter signal in phase space by that same angle. Therefore, to correct for a misaligned quadrature orientation of the balanced homodyne detectors, an additional parameter φ_1 for an overall phase shift in Equation (6.10) was required.

One other thing that needed to be considered here was the EOM that was placed inside the cavity and used to shift the scatter disturbance to the MHz regime. The EOM applied a phase modulation to the scattered light beam and after demodulation during data acquisition I effectively measured the modulation of these sidebands due to the scatter source. Since the beat between the lower and upper sidebands is 90° out of phase with the carrier light this corresponds to an additional overall phase shift of $\pi/2$ in Equation (6.10) and effectively switches the models for the two quadrature projections. This effect was of course also present in the previous experiments, but was automatically compensated for by the constant part in $\varphi(t)$. In total we arrive at

$$E_{\text{sc}} = i A e^{i(\varphi(t) + \varphi_1)} / (1 + g e^{i\varphi(t)}) \quad (6.11)$$

and the models for the projection of the disturbance in the phase quadrature and amplitude quadrature measurements are given by

$$p_{\text{sc}}(t) = \frac{-A (\sin(\varphi(t) + \varphi_1) + g \sin \varphi_1)}{(1 + g \cos \varphi(t))^2 + g^2 \sin^2 \varphi(t)} \quad (6.12)$$

$$x_{\text{sc}}(t) = \frac{A (\cos(\varphi(t) + \varphi_1 + \varphi_2) + g \cos(\varphi_1 + \varphi_2))}{(1 + g \cos \varphi(t))^2 + g^2 \sin^2 \varphi(t)} \quad (6.13)$$

Note that I allowed for another small overall phase shift φ_2 in the model for the amplitude quadrature to compensate for a deviation of the quadrature angle between the two detectors from 90° . For the time dependent phase shift $\varphi(t)$ the higher order model of Equation (6.8) was used.

The fitting was done following basically the same procedure as in Section 6.2.3. At first, a reduced set of parameters was determined by fitting the time dependent Doppler shift of Equation (6.7) to the arches (of the first round trip) in the spectrogram data of the phase quadrature detector BHD1. This first fit yielded good start parameters for the modulation depth m_1 , frequency f_m and phase $\phi_{m,1}$ of the scatter source motion in $\varphi(t)$.

Afterwards, the full model of Equation (6.12) was fitted to the appropriately filtered and downsampled time series data of the phase quadrature measurement. The fit was performed using Matlab's 'lsqcurvefit' function together with 'MultiStart' to run the solver from multiple start points. I provided a set of different start parameters which were chosen similarly to the ones in Section 6.2.3 and combined with different sets of randomly distributed starting phases $\phi_{m,n>1} \in [-2\pi, 2\pi]$ and modulation depths $m_{n>1} \in [-m_1/10, m_1/10]$ for the higher order contributions in $\varphi(t)$. The two new parameters in the model of Equation (6.12) were set to start at $g = 0.5$ and $\varphi_1 = 0$. Like in Section 6.2.3 the boundaries were set to span the whole reasonable parameter space.

The results of this fit for the measurements with the 2 Hz and 10 Hz disturbances are shown in Figure 6.20 (a) and (b) respectively. The gray traces show a segment of the downsampled phase quadrature data measured at BHD1 and the blue traces show the modeled scatter disturbance for the parameters obtained in the fits. Note that the mean values of both, data and models, were subtracted to have the signals centered around zero. This was done because the data had a small dc-offset from data acquisition and the levels needed to be adjusted for the fitting.

In the end the projection of the scatter disturbance into the amplitude quadrature measurement was computed by inserting the obtained parameters into the model of Equation (6.13). Just like in Section 6.2.3 the signal amplitude A and the deviation of the quadrature angle between the two detectors φ_2 from 90° were fitted separately using the amplitude quadrature data of BHD2. A segment of the data (gray) and the resulting modeled disturbance (blue) are depicted in Figure 6.21 (a) and (b) for the 2 Hz and the 10 Hz disturbance respectively.

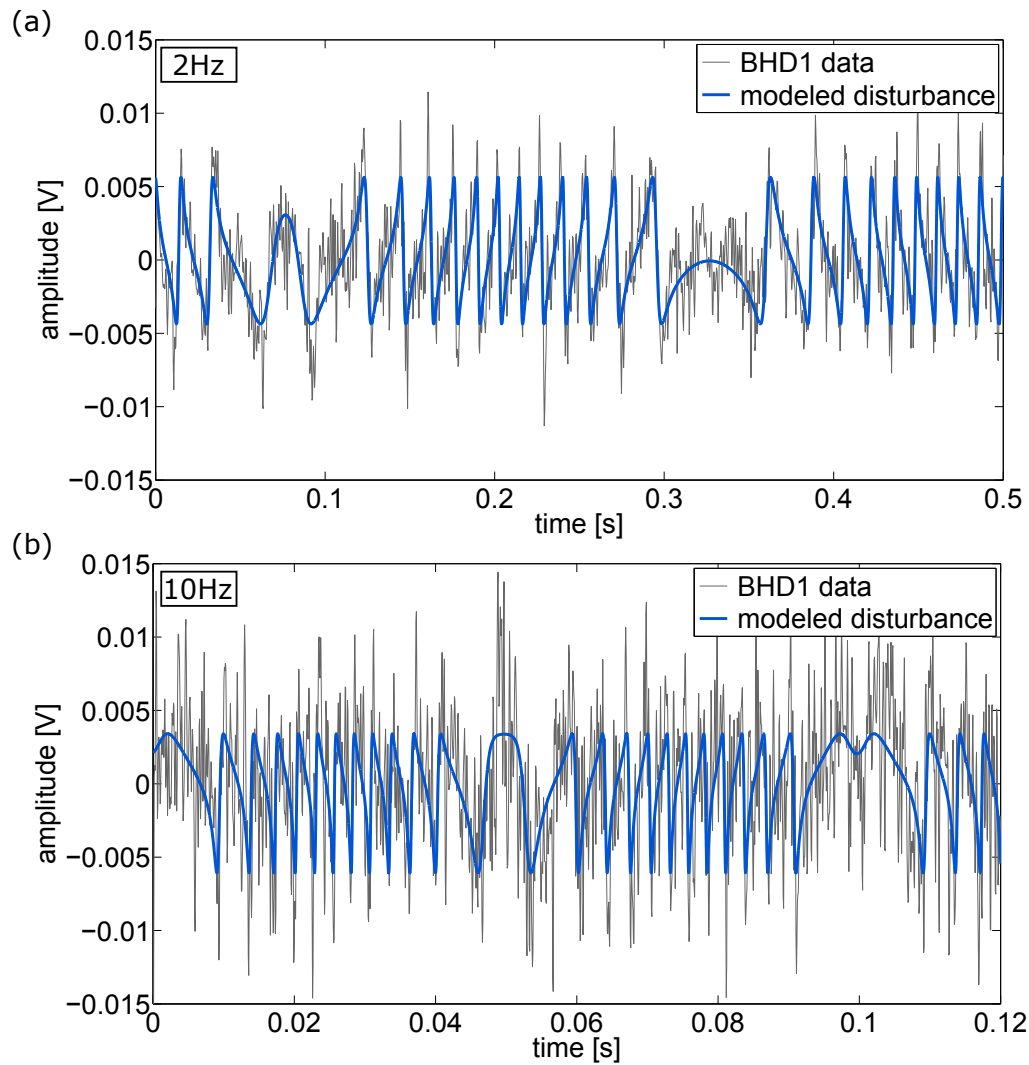


Figure 6.20.: Projection of the scatter disturbance in the phase quadrature. The plots show an averaged segment of the phase quadrature measurement data (gray) overlaid with the modeled disturbance signal obtained in the fit (blue) for the 2 Hz and 10 Hz measurements respectively. Data and models have been centered around zero by subtraction of their mean value.

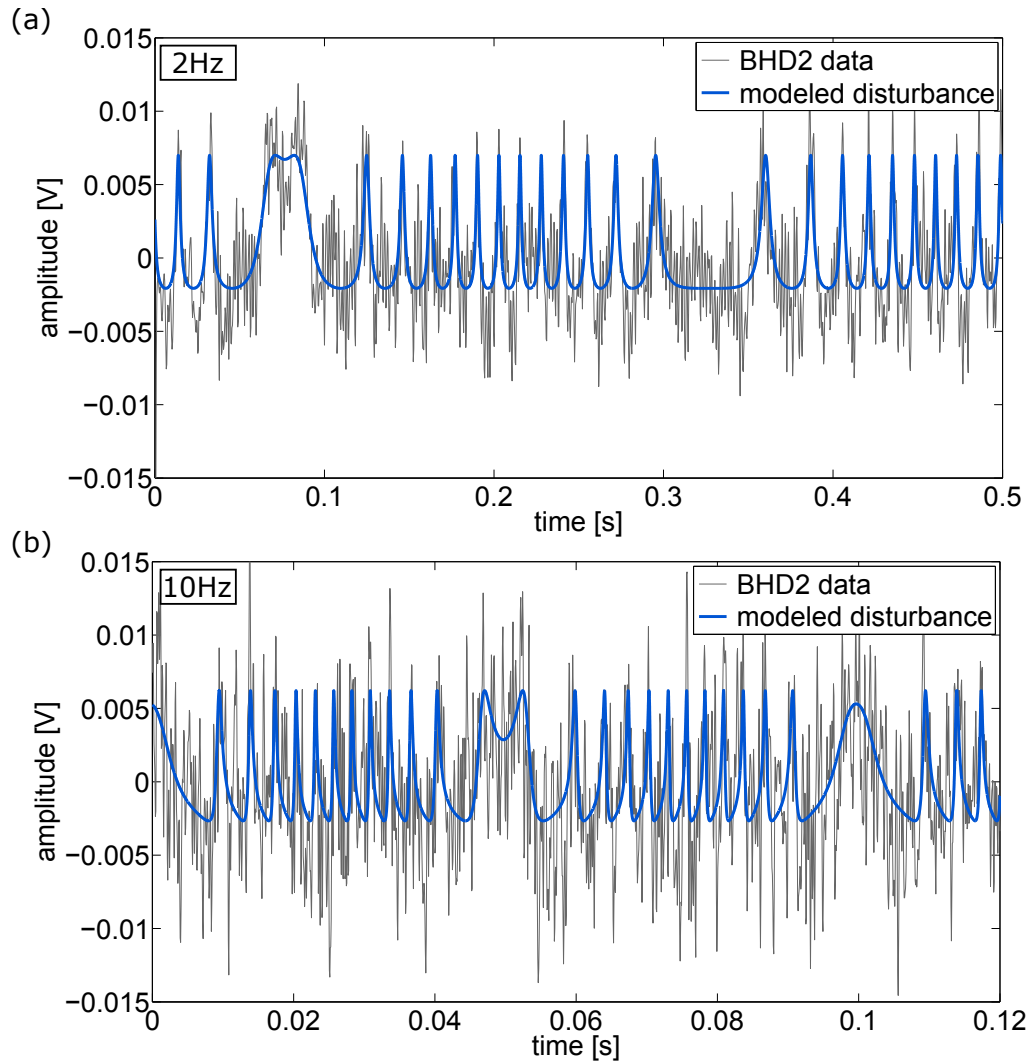


Figure 6.21.: Projection of the scatter disturbance in the amplitude quadrature. The plots show an averaged segment of the amplitude quadrature measurement data (gray) overlaid with the modeled disturbance signal obtained in the fit (blue) for the 2 Hz and 10 Hz measurements respectively. Data and models have been centered around zero by subtraction of their mean value.

6.3.4. Subtraction of the scatter disturbance

The subtraction of the 2 Hz back-scatter disturbance is shown in Figure 6.22 (a) in a spectrogram and (b) as the averaged power spectral density (PSD). In the spectrograms of the residual, for both detectors, the disturbance is not visible anymore and the injected GW-like signal could be recovered in the amplitude quadrature data of BHD2. There is also some GW-like signal and quadrature marker at 550 Hz discernible in the residual of BHD1, which shows again that the quadrature angle was not optimally aligned in this measurement.

In the averaged PSD in (b) the residual after subtraction of the modeled disturbance (red) is shown in comparison with the original measurement data (blue) and a shot noise reference measurement (gray). The scatter shoulder vanished almost completely after the subtraction. There is some residual excess noise visible in the data of BHD1 between about 50 Hz and 150 Hz which is probably mainly due to the misaligned quadrature angle, i.e. the small amount of GW-like signal that was present in the data (see Figure 6.22 (a)).

Similarly, the results for the 10 Hz disturbance are given in Figure 6.23. Also here the disturbance could be removed and the GW-like signal was recovered. The quadrature orientation of the two detectors was not optimal in this measurement either. Choosing the same resolution as in Figure 6.22 (b) the marker peak at 550 Hz in the averaged PSD of the residual of BHD1 (red) would actually be even larger than in the measurement with the 2 Hz disturbance (about $3 \cdot 10^{-8} \text{ W/Hz}$).

The corresponding parameters used in the model of the disturbance for the 2 Hz and the 10 Hz measurements are given in Table 6.6 and 6.7 respectively. Note, that A does not really correspond to its definition in Equation (6.9) since it also includes the scaling due to the interferometer transfer, detection and data acquisition parts. The parameter g describes the factor by which the amplitude of the back-scattered light changed per round trip in the cavity. The values for g found in the fits for both measurements were consistent but higher than one would expect for the given reflectivities of the interferometer end mirror $\rho_{\text{end}} \approx 0.99$ and the scatter mirror $\rho_{\text{sc}} \approx 0.47$. With $\rho_{\text{sc}}^{\text{eff}} < \rho_{\text{sc}}$ these would result in $g < 0.46$. An explanation for this could be the EOM inside the scatter cavity since it shifts more power from the carrier into the sidebands (which I effectively measure in the end) twice during each round trip. The fitted modulation depths for the 2 Hz and 10 Hz disturbance correspond to total path length changes of 12.5λ and 11.5λ respectively from the foremost to the very back position of the scatter mirror. This is consistent with the measured cavity transmission over one oscillation period shown in Figure 6.16. Also the amplitudes of the higher order contributions $m_{n>1}$ in $\varphi(t)$ were of the same order for both measurements and the modulation frequencies f_m were correctly reproduced in the fits.

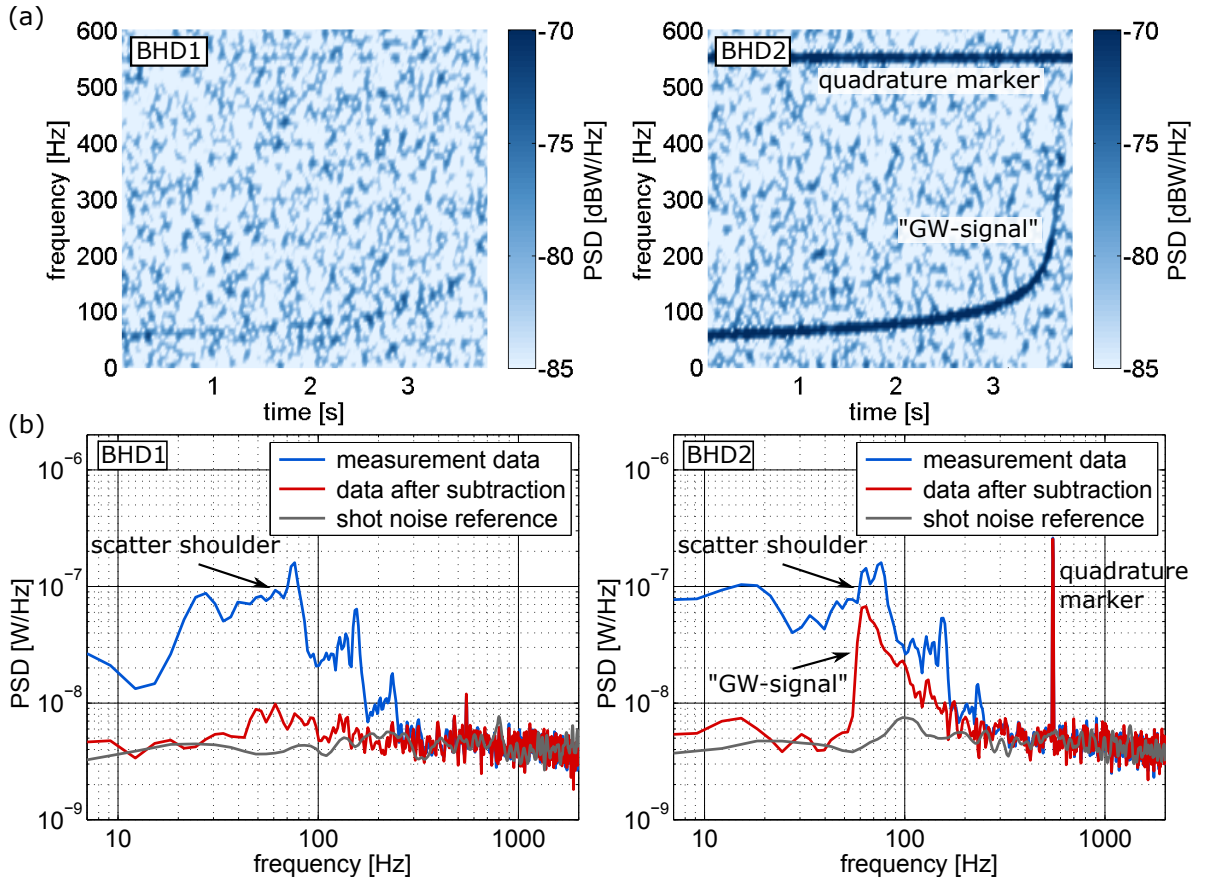


Figure 6.22.: Results after subtraction of the scatter model for the 2 Hz disturbance. (a) Phase and amplitude quadrature data after subtraction of the scatter disturbance in a spectrogram. (b) Averaged power spectral density (PSD) of the data after subtraction of the disturbance (red) in comparison with the original measurement data (blue) and a shot noise reference (gray), measured with the signal ports of the detectors blocked.

BHD1	A [mV]	g [d.u.]	φ_1 [rad]	φ_0 [rad]	m_1 [rad]	f_m [Hz]	$\phi_{m,1}$ [rad]
	3.2917	0.5840	0.1159	1.6663	39.2356	2.0000	0.6154

order n	2	3	4	5	BHD2	A [mV]	φ_2 [rad]
m_n [rad]	-0.5323	2.5655	0.1694	-0.7847		3.0033	-0.1598
$\phi_{m,n}$ [rad]	-4.8489	1.6132	-4.1450	-4.1339			

Table 6.6.: Fitted parameters for the 2 Hz disturbance and the scatter model including higher harmonics and multiple round trips.

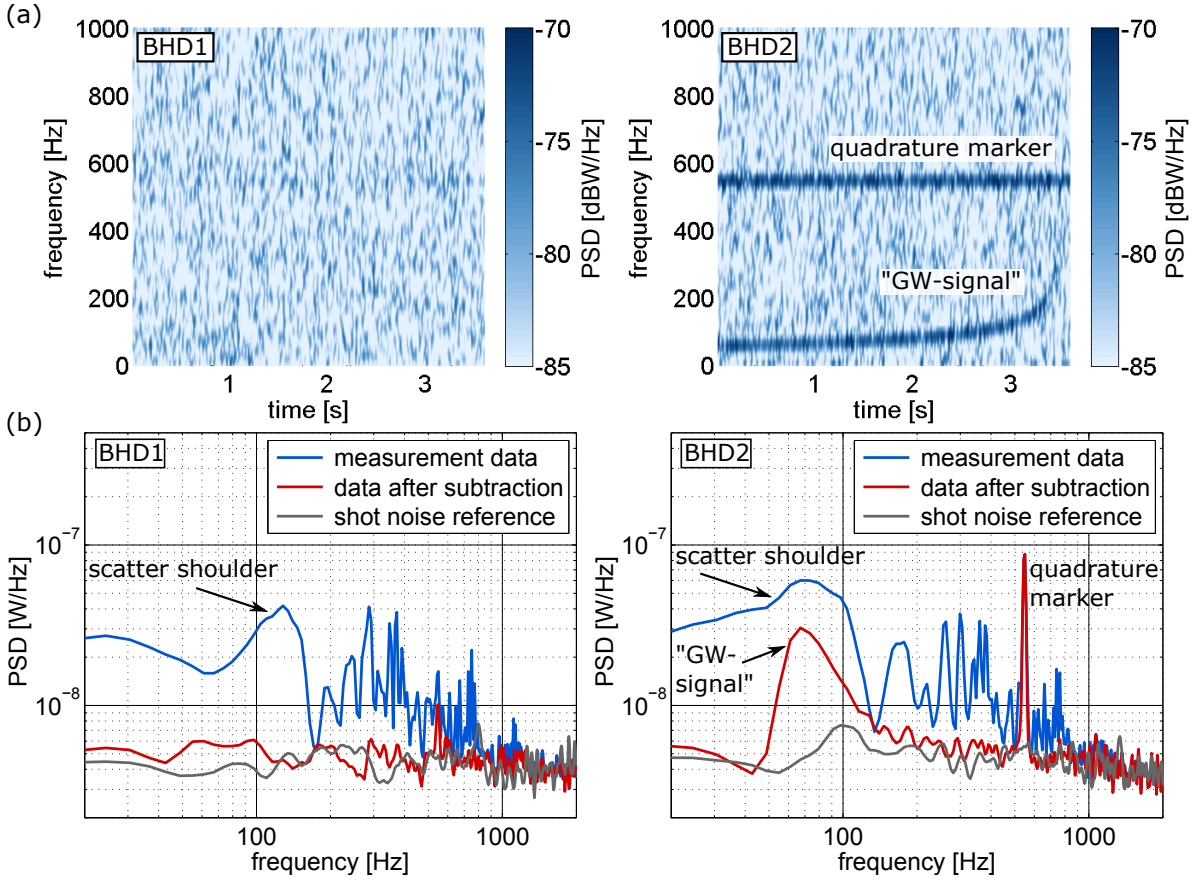


Figure 6.23.: Results after subtraction of the scatter model for the 10 Hz disturbance. (a) Phase and amplitude quadrature data after subtraction of the scatter disturbance in a spectrogram. (b) Averaged power spectral density (PSD) of the data after subtraction of the disturbance (red) in comparison with the original measurement data (blue) and a shot noise reference (gray), measured with the signal ports of the detectors blocked.

BHD1	A [mV]	g [d.u.]	φ_1 [rad]	φ_0 [rad]	m_1 [rad]	f_m [Hz]	$\phi_{m,1}$ [rad]
	3.1285	-0.5828	0.3967	-0.5945	36.1917	10.0002	1.5229

order n	2	3	4	5	BHD2	A [mV]	φ_2 [rad]
m_n [rad]	0.5000	2.5267	0.1059	-0.6773		2.7305	0.1386
$\phi_{m,n}$ [rad]	4.5646	-0.5698	0.4579	-4.0045			

Table 6.7.: Fitted parameters for the 10 Hz disturbance and the scatter model including higher harmonics and multiple round trips.

6.3.5. Discussion

The results of this section present the subtraction of a scatter shoulder with multiple round trips for the back-scattered beam. The scatter disturbance introduced here was in some sense more realistic than the disturbances of the last sections since it was produced from light that actually left the interferometer mode and was back-scattered (instead of using an external beam).

The same points discussed in Section 6.2.5 also apply for the measurements presented here. The differing signal amplitudes in the two quadratures probably originated from an unbalanced splitting of the interferometer signal. The quadrature offset between the detectors (here φ_2) can be explained by differing powers in the used control beams in connection with an unbalanced splitting at their combination (see Figure 6.9 ①).

In this experiment also the actual quadrature offsets of the two detectors from the amplitude and phase quadratures can be determined from the fitted parameters. φ_1 gives the offset in the phase quadrature measurement and the amplitude quadrature offset is determined by $\varphi_1 + \varphi_2$. The parameters in Table 6.6 show that the quadratures were not optimally met in the 2 Hz measurement but already quite well with 6.6° for the phase quadrature and -2.5° for the amplitude quadrature (here for convenience in degree). According to Table 6.7, for the 10 Hz measurement the quadrature alignment was much worse, about 22.7° for the phase quadrature and even 30.7° for the amplitude quadrature measurement. Note again, that for the same resolution bandwidth as in the 2 Hz measurement, the marker peak at 550 Hz in the residual of BHD1 (red) in Figure 6.23 (b) would be larger (about $3 \cdot 10^{-8}$ W/Hz). The quadrature orientation of the detectors with respect to the interferometer signal was not electronically stabilized but adjusted manually in this experiment and as already mentioned in the beginning of this section, the measurements were not yet optimized.

7. Application of quantum-dense metrology for subtraction of a back-scatter shoulder

In this chapter I will present the improvement of a scattered light limited measurement below the quantum shot noise by employing quantum-dense metrology (QDM). These results built on the experiences and achievements of the experiments described in Chapter 6. In Section 7.1 I will give a short overview on the setup for the two-mode-squeezing enhanced dual readout and the injected test signals. A detailed description of the complete setup is given in Chapter 5 and the test signals are fully described in Sections 3.2.2 and 6.2.1. Section 7.2 summarizes the main steps of the data post-processing which was analogous to the procedure described in Section 6.2.3. The results presented in this chapter were published in *Physical Review Letters* [43].

7.1. Experimental setup

The experiment used the complete setup described in Chapter 5 and the test signals of Section 6.2.1. As a reminder, the readout part of the setup is given again in Figure 7.1. The squeezed light generation will not be repeated here, details on this can be found in Section 5.2.

The solid red paths in Figure 7.1 show the interferometer input beam and the local oscillators for the two balanced homodyne detectors BHD1&2. For more clarity, the paths of the local oscillators were not highlighted completely but only indicated with arrowheads. The orange beam that was picked off of the interferometer input beam was used to generate the scatter disturbance. A broadband scatter shoulder was produced via frequency up-conversion by modulating a piezo actuated mirror at a frequency of 5 Hz over several wavelengths ($\lambda = 1064 \text{ nm}$). For more details on the scatter disturbance see Sections 3.2.2 and 6.2.1. The GW-like chirp signal and a quadrature marker for stabilization of the balanced homodyne detectors were again produced by modulating one of the interferometer end mirrors. A smaller signal amplitude was chosen in this setup, such that the GW-like signal stood out only slightly above the measured vacuum noise level.

Two squeezed states (white ellipses) enter the picture from the right side. They were generated by the source described in Section 5.2 and their paths are highlighted in dashed red. The two states were overlapped on a 50/50 beam splitter to create the required entangled states. For the sub-shot-noise enhancement of the dual readout one

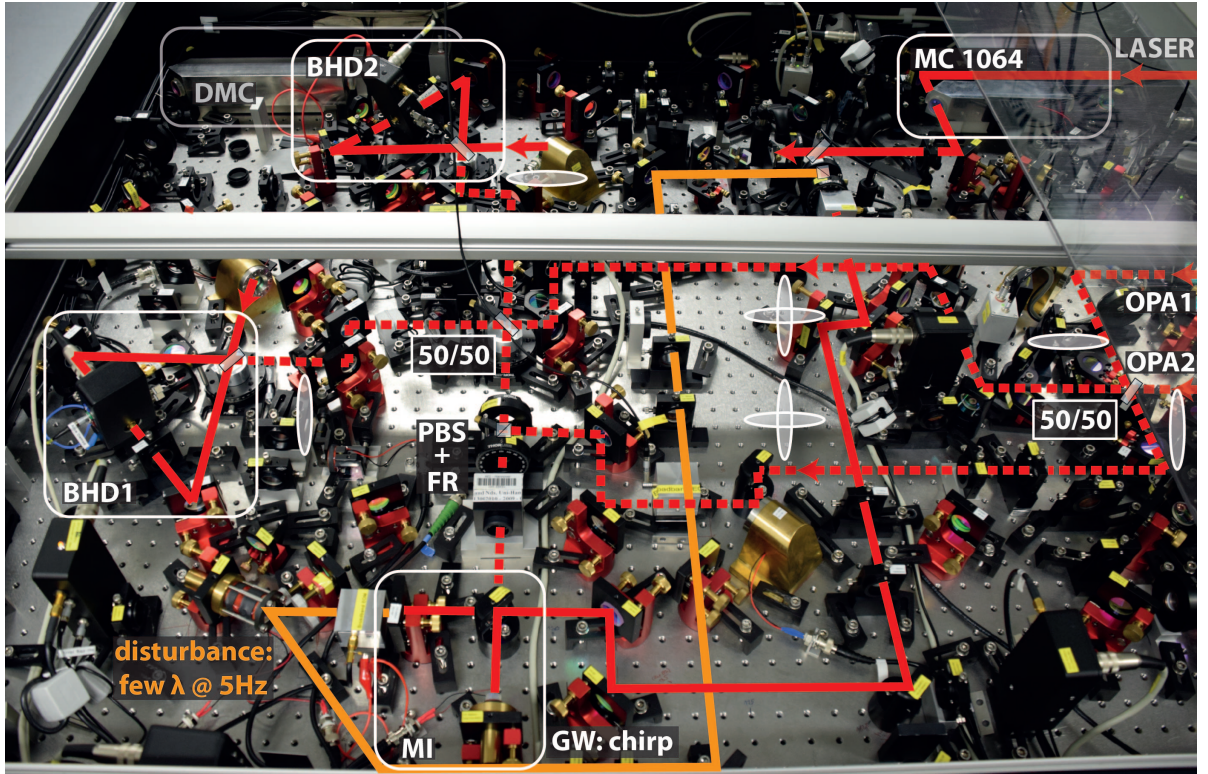


Figure 7.1.: Setup for the quantum-dense interferometer readout. Solid red: interferometer and local oscillators beams, dashed red: squeezed and entangled beams, orange: scattered light beam. Control beams and alignment paths were not highlighted. MC: mode cleaner, MI: Michelson interferometer, OPA: optical parametric amplifier, BHD: balanced homodyne detector, DMC: diagnostic mode cleaner.

of the resulting two-mode-squeezed states was reflected at the interferometer dark port via a combination of a polarizing beam splitter (PBS) and a Faraday rotator (FR) while the other one was sent directly to the 50/50 beam splitter in the interferometer output. After recombination of the two states with the right phase relation, the initial squeezed states were recovered and enabled simultaneous sub-shot-noise measurement of the phase quadrature and amplitude quadrature of the interferometer signal at BHD1&2.

Paths of the additional control beams are not highlighted in the picture. The full control scheme for the quantum-dense readout is described in Section 5.3 and the data acquisition is described in Section 5.4

7.2. Measurement and post-processing

Figure 7.2 shows the measurement data of the quantum-dense readout (blue) as an averaged power spectral density (PSD). For comparison, a measurement using solely the dual readout, without injection of the entangled states, is also given in the plot (black). This corresponds to a measurement like it was performed in Section 6.2.

The broadband scatter disturbance was the dominant noise source in both measurements for frequencies below about 200 Hz. The shape of the disturbance was slightly different for the two measurements because the center position of the scatter mirror differed for them. Above 200 Hz, the dual readout data was limited by optical shot noise, i.e. vacuum noise. In this frequency regime, the quantum-dense readout already improved over the simple dual readout. The shot noise was simultaneously squeezed in both, phase quadrature (BHD1) and amplitude quadrature (BHD2) readout, which led to an improved signal-to-noise-ratio for the injected signals.

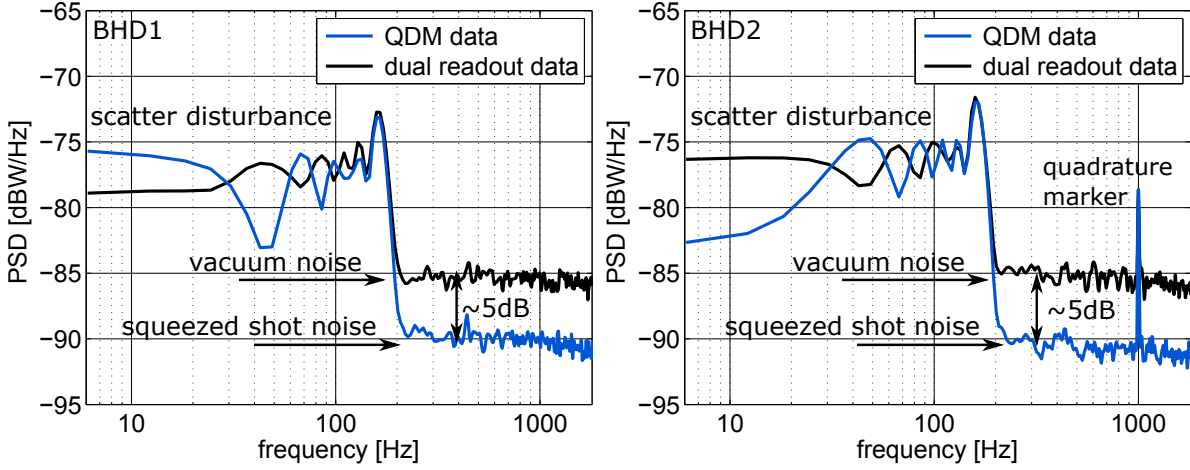


Figure 7.2.: Quantum-dense measurement with back-scatter disturbance. The plots show the averaged power spectral density (PSD) of the phase quadrature (left) and amplitude quadrature (right) data at BHD1&2. The blue traces show a measurement for the setup employing quantum-dense metrology (QDM). For comparison, the black traces show a measurement without injection of the entangled states, as performed in the experiment of Section 6.2. The shape of the disturbance slightly differed in the two measurements because of different center positions of the scatter mirror.

The post-processing of the data from the quantum-dense measurement was performed in the same way as described in Section 6.2.3. First, the parameters of the scatter disturbance were determined by fitting the scatter model of Equation (6.5) with the higher order phase shift of Equation (6.8) to the phase quadrature data of BHD1. The model assumed a sinusoidal motion of the scatter source with constant amplitude and frequency at a constant mean distance to the interferometer. Higher harmonics of the oscillation frequency up to the 5th order were included to account for the nonlinear response of the piezo actuator. The obtained fit is depicted in the upper graph in Figure 7.3 (black), together with an averaged segment of the measured time domain data of BHD1 (blue). The projection of the scatter disturbance into the amplitude measurement was computed via Equation (6.6) with the higher order phase shift of Equation (6.8). As explained in Section 6.2.3, the amplitude of the scatter disturbance in that projection and a quadrature offset φ_{offset} were fitted separately from the measurement data of BHD2 to compensate for differences in the two detection paths and an imperfect quadrature

alignment of 90° between the detectors. The projected model for the scatter disturbance (black) and an averaged segment of the amplitude quadrature measurement data (blue) are shown in the lower graph of Figure 7.3. The corresponding parameters from both fits are given in Table 7.1 and are in good agreement with the parameters found in Section 6.2.3.

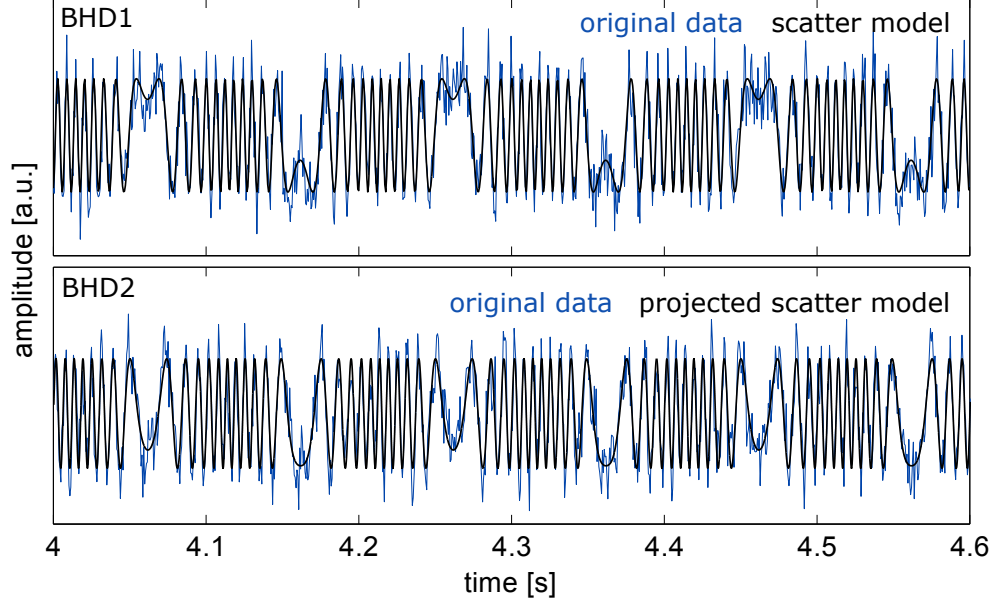


Figure 7.3.: Time domain data with fitted scatter model. The plots show an averaged segment of the time domain data measured at BHD1&2 (blue). The projections of the fitted scatter model into the phase quadrature and amplitude quadrature are overlaid in black.

BHD1	A [mV]	φ_0 [rad]	m_1 [rad]	f_m [Hz]	$\phi_{m,1}$ [rad]
	-2.6507	-1.9181	34.4181	5.0001	-3.5360

order n	2	3	4	5	BHD2	A [mV]	φ_{offset} [rad]
m_n [rad]	0.6478	-1.1678	-0.1882	0.7153		3.0255	0.1502
$\phi_{m,n}$ [rad]	3.1937	-1.7056	-0.1195	2.7145			

Table 7.1.: Fitted parameters for the scatter disturbance.

7.3. Subtraction of the scatter disturbance

The results after subtraction of the scatter disturbance are depicted in Figure 7.4 in frequency domain. Figure 7.4(a) shows the averaged power spectral density (PSD) of the quantum-dense measurement data before (blue) and after (red) subtraction of the modeled scatter disturbance. Two reference measurements are also shown in the plots

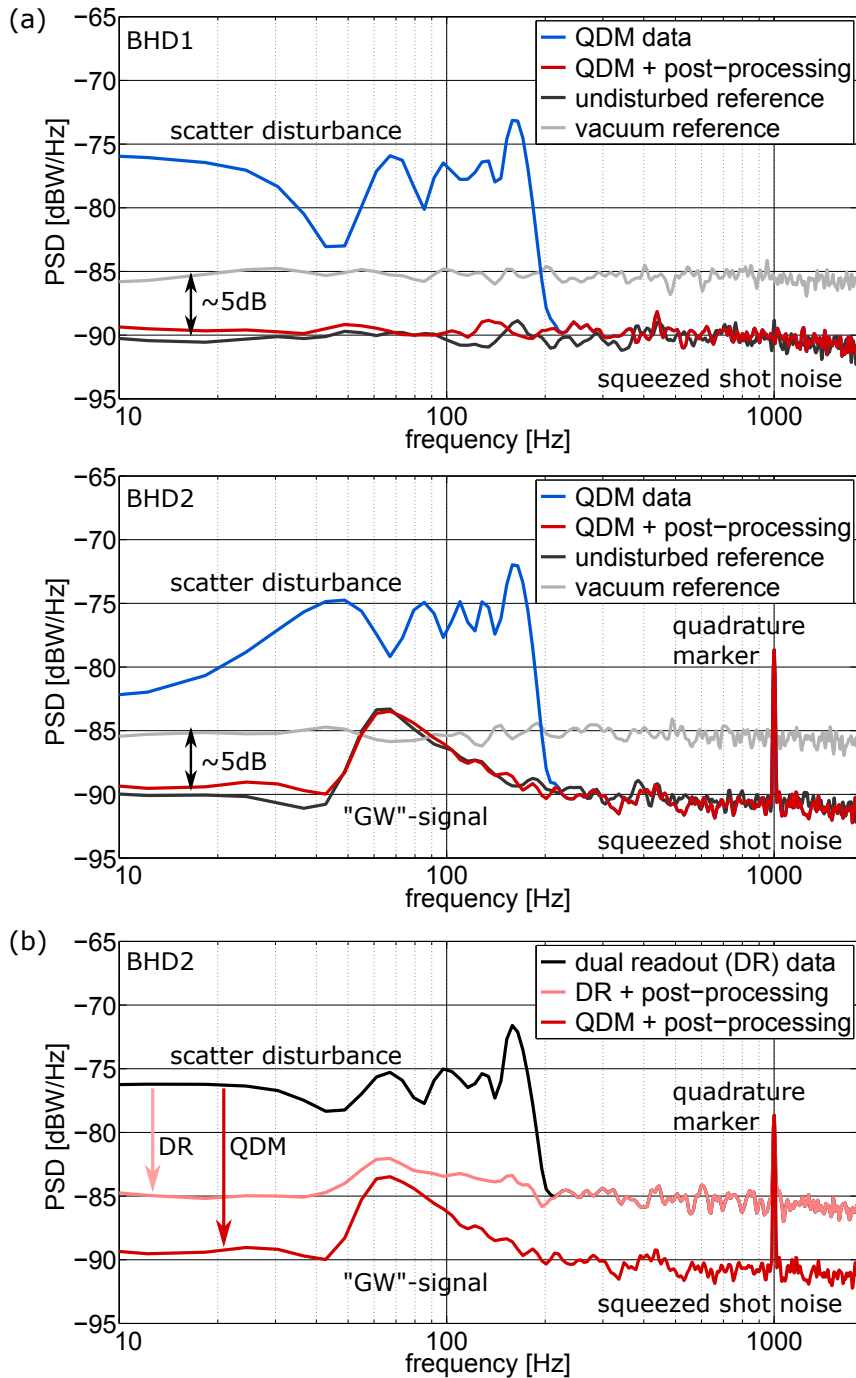


Figure 7.4.: Sensitivity improvement via QDM with data post-processing. (a) Power spectral density of the phase and amplitude quadrature data, measured with BHD1&2, before (blue) and after (red) subtraction of the modeled scatter disturbance. A measurement without scatter disturbance (dark gray) and a vacuum noise measurement (light gray) are also shown for comparison. (b) Visualization of the overall improvement through quantum-dense metrology (QDM) with respect to earlier results using the dual readout (DR) without entanglement enhancement.

(i) an undisturbed reference measurement where the scattered light beam was blocked in the setup (dark gray) and (ii) a vacuum noise reference (light gray), measured with the signal ports of the two balanced homodyne detectors blocked.

The scatter disturbance could be completely removed from the measurement data of both detectors, as becomes clear by comparison with the undisturbed reference measurement. The GW-like signal in the amplitude quadrature data of BHD2 was clearly recovered. Furthermore, sub-shot-noise sensitivity was achieved in both quadrature measurements with a nonclassical noise suppression of about 5 dB over the whole spectrum.

Figure 7.4 (b) visualizes the overall improvement of the quantum-dense measurement with respect to the results of Section 6.2 for the amplitude quadrature detector BHD2. The black trace shows again the measurement of Figure 7.2 which used solely the dual readout (DR) without injection of the entangled states. The scatter disturbance limited the sensitivity in the low-frequency regime, while the high-frequency regime was limited by optical shot noise (vacuum noise). Post-processing of the dual readout data according to Section 6.2.3 led to the pink trace in Figure 7.4 (b). The scatter disturbance could be subtracted up to the vacuum noise level and a small 'bump' in the resulting spectrum already indicates the injected GW-like signal. The application of quantum-dense metrology (QDM) with the additional data post-processing (red trace) further reduced the limiting noise floor by about 5 dB over the whole frequency range and thereby increased the signal-to-noise-ratio for the readout of the GW-like signal by the same amount.

7.4. Discussion

With the results of this chapter I could show that the novel approach for the subtraction of back-scatter disturbances can be combined with a quantum dense readout. The sensitivity for the 'scientific' amplitude readout, as well as for the scatter reference measurement of the phase quadrature, could be improved to reach a nonclassical noise suppression of about 5 dB.

In Chapter 5, I mentioned that the source for the two-mode-squeezed states was shown to produce strong EPR entanglement which corresponded to about 10 dB of squeezing for the initial states. The much lower values achieved here can be attributed to a much higher loss in the optical setup. For the entanglement measurement, the two-mode-squeezed states were detected as close as possible behind the entangling 50/50 beam splitter, i.e. using as few optical components as possible. In the setup used here, the paths to the detectors were much longer and contained many additional transmissive optics like lenses for mode matching, in total four $R = 1\%$ beam splitters to tap off power for the locking scheme, a polarising beam splitter (PBS), two $\lambda/2$ wave plates and a Faraday rotator which were passed twice for coupling one of the two-mode-squeezed states into the interferometer and 50/50 beam splitters in the interferometer and its output. Apart from that, one of the interferometer end mirrors had a reduced reflectivity of about 98% to couple in the scattered light beam. Also, if the splitting ratio achieved at the beam splitter in the interferometer output does not exactly match the

the splitting ratio of the entangling beam splitter, or the relative phase shift between the two-mode-squeezed states is not optimal for their recombination, the anti-squeezing cannot perfectly cancel and further decreases the squeezing strength. The same is true for imbalanced loss for the two-mode-squeezed states, as already described in Section 4.2. This was definitely the case here, since the loss in the interferometer path was much higher.

8. Summary and conclusion

This thesis proposes a new approach for mitigation of back-scattered light induced disturbances in interferometric gravitational-wave detectors. The approach makes use of the additional information about back-scatter disturbances that is contained in the orthogonal observable of the interferometer signal. The information is used to find an analytical description for the disturbance signal which can then be subtracted from the measurement data. A new readout scheme is required to get to this additional information. In the setup realized here, the interferometer output is equally split and the orthogonal amplitude and phase quadratures of the signal are being detected with two balanced homodyne detectors.

In the first part of my work, I set up a proof of principle experiment to test the new scheme for some exemplary scatter disturbances. These were based on a sinusoidal motion of the scatter source with constant parameters. The disturbance signals varied from a monochromatic peak in the spectrum to a broadband scatter shoulder from frequency up-conversion with multiple round trips for the back-scattered beam.

I showed that the experimentally produced disturbance signals could be sufficiently described using a sinusoidal analytic model, which included some higher harmonics contribution for the disturbances from sources with large amplitude motion. The projection of the back-scatter disturbances in the scientifically relevant amplitude quadrature could be successfully inferred from the models obtained from the phase quadrature measurement data. The disturbances could be completely subtracted from the measurement data revealing a formerly concealed artificial GW signal.

In the second part of my work, I showed that the new mitigation technique is compatible with a sub-shot-noise enhancement of the interferometer readout through squeezed states of light. Instead of a single quadrature squeezed readout as proposed by Caves [16] and employed in GEO 600 [17, 18], two-mode-squeezed states were required to simultaneously enhance both quadrature readouts and enter the regime of *quantum-dense metrology* (QDM) [33].

In a similar proof of principle setup, I used a scatter shoulder from frequency up-conversion to create a scenario where the interferometric measurement was limited by classical excess noise in the low frequency regime and by optical shot-noise at higher frequencies. Through the injection of the two-mode-squeezed states, the measurement sensitivity in the shot noise limited regime was increased, while the low frequency regime was unaffected of the enhancement. Only by employing the new approach for subtraction of the back-scatter disturbance, also the low frequency regime could be improved to sub-shot-noise sensitivity. A nonclassical noise suppression of about 5 dB was achieved in both quadrature readouts over the whole spectrum under consideration.

Though the disturbance signals generated here were quite elementary, they already reproduced the basic structures of typical back-scatter disturbances as observed in gravitational-wave detectors [25, 29]. In the LIGO data presented in Fig. 3.1 of reference [24], for example, the bump structure in the scatter shoulder is quite pronounced which might indicate that indeed a slowly varying mechanical vibration gave rise to this disturbance. Independent of this, the technique is not restricted to the simple sinusoidal model. An important next step would be to investigate how well real back-scatter disturbances, which occurred in a gravitational-wave detector, can be modeled.

For implementation of the scheme in a gravitational-wave detector some other aspects need to be considered. Due to the splitting of the interferometer output field, the signal-to-shot-noise-ratio in the relevant amplitude measurement decreases by a factor of 2. In the case of QDM, I showed that this effect can be partially compensated, leading to lower factors of about 1.6 for a realistic detector scenario with about 10 dB input squeezing and about 25% optical loss. Generally, the tapped power for the reference measurement of the phase quadrature could be reduced, which would in turn go along with a reduced quality of the scatter monitor. For the quantum-dense readout two identical unbalanced beam splitters for the generation of the two-mode-squeezing and the readout would be required to reduce the tapped power.

The scheme as proposed here recommends balanced homodyne detection, at least for the additional phase quadrature readout. This technique has not been used in gravitational-wave detectors so far, but was already suggested for future sensitivity improvements [61] and was shown to have some practical advantages with respect to the currently used *DC readout* [62]. The balanced homodyne readout requires an optical local oscillator. Recent investigations showed that the requirements for the amplitude noise of the local oscillator and its path-length stability are within manageable ranges with current technologies [63].

An implementation of the quantum-dense readout in a gravitational-wave detector imposes similar requirements on the setup as the implementation of squeezed light enhancement. For example, optical loss in the setup needs to be minimized to achieve strong nonclassical noise suppression and a coherent control scheme [57, 58] is required to avoid technical laser noise and preserve the squeezing in the detector's sensitive frequency range. The relevant experimental techniques have already been demonstrated successfully in the detector GEO 600 [17, 18].

In conclusion, the scheme presented here offers a new way to reduce noise from back-scattered light in gravitational-wave detectors. It allows to achieve sub-shot noise sensitivity in a measurement which was initially limited by strong classical excess noise. The implementation of the required quantum-dense readout will become technically feasible as soon as balanced homodyne detection has been demonstrated for gravitational-wave detectors. In future gravitational-wave detectors, the scheme could provide an essential extension to standard mitigation techniques like beam dumping and vibration isolation of potential sources when those reach their technical limitations.

Appendices

A. LabView program

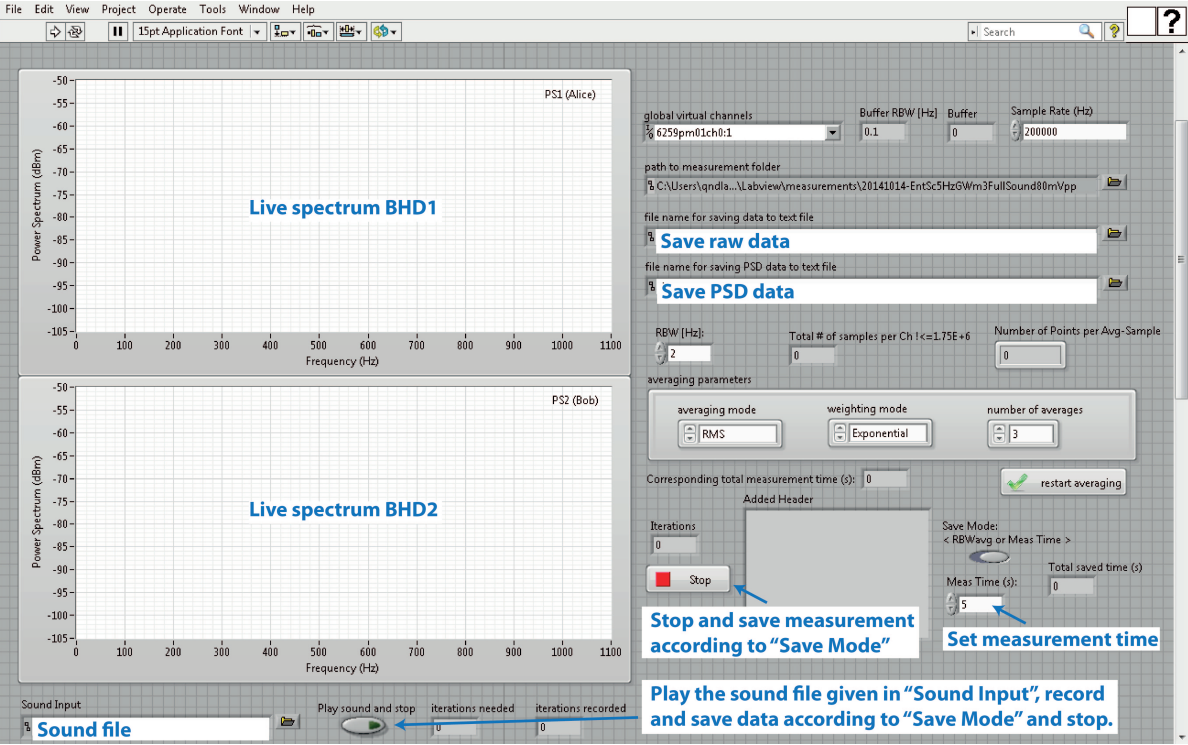


Figure A.1.: LabView user interface

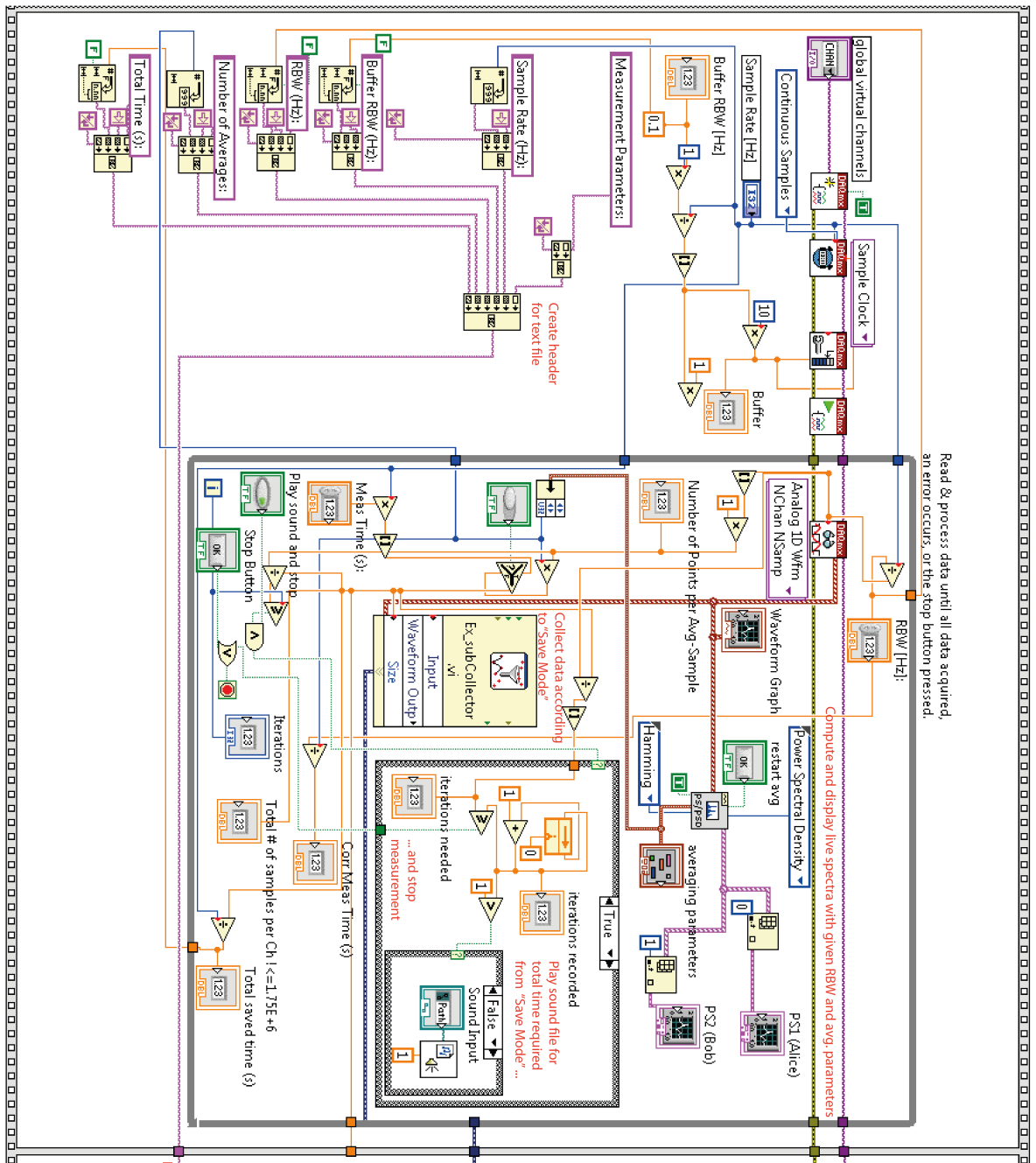


Figure A.2.: LabView block diagram part 1

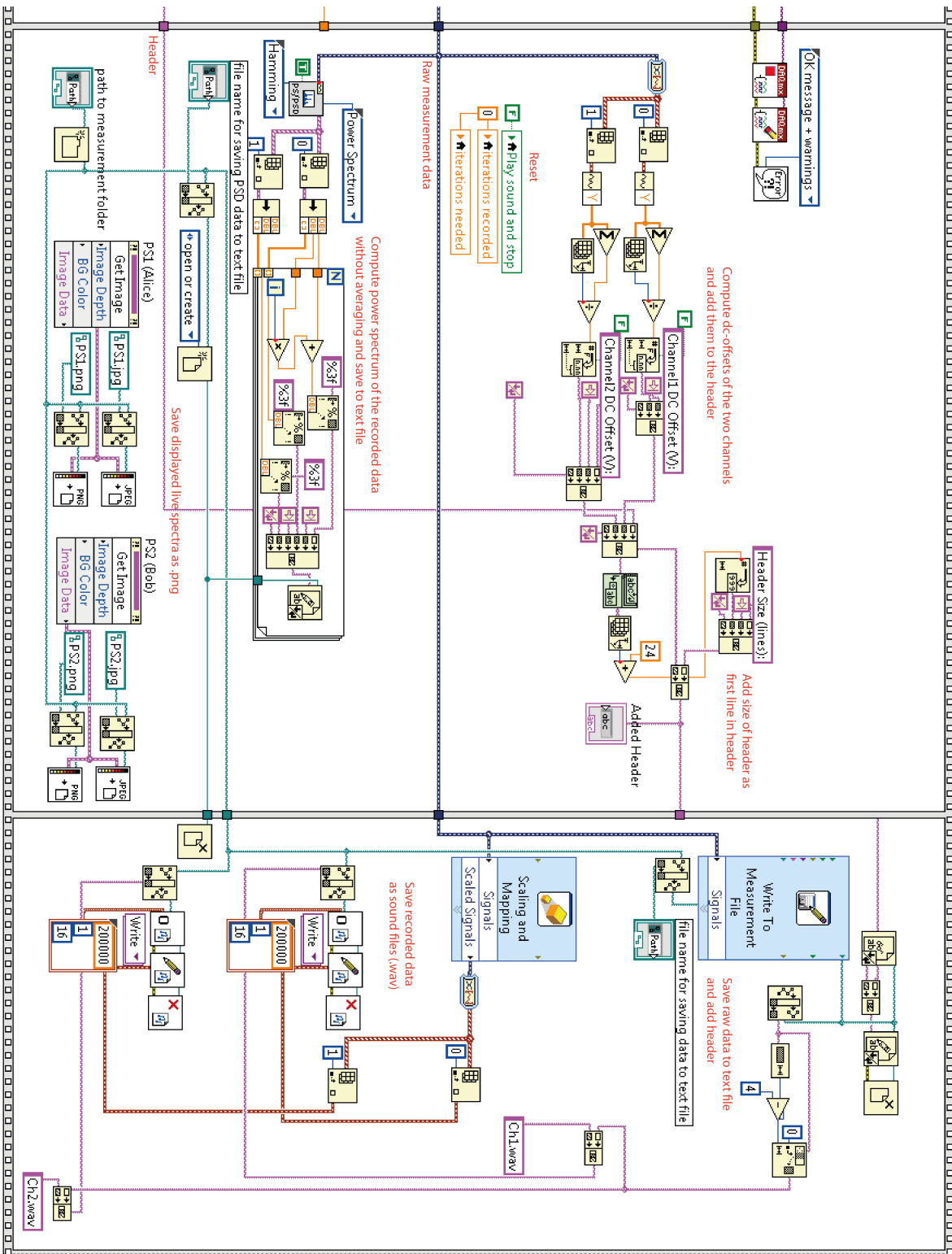


Figure A.3.: LabView block diagram part 2

B. Matlab scripts

Import LabView data

```
function [timedata ,det1 ,det2 ,sampleFrequency] = LabViewDataImport(
    fileToRead)

% Imports data from fileToRead with columns [timedata or empty,data1 ,data2
    ]
% and returns timedata , data1&2 (with removed dc-offset) and the sample
% frequency

% open fileToRead
fid=fopen(fileToRead);

% determine number of header lines
linenum = 1; % number of headerlines information is in first line
line1=textscan(fid , '%s %d' , 1, 'delimiter' , '\t' , 'headerlines' ,...
    linenum-1); % returns string and number of headerlines

% set delimiter and number of header lines
DELIMITER = '\t';
HEADERLINES = line1{2};

% import fileToRead
newData = importdata(fileToRead , DELIMITER, HEADERLINES);

% read sample frequency and total measurement time from header
header=newData.textdata;
for l = 1:HEADERLINES;
    sr = strfind(header{l}, 'Sample Rate (Hz):');
    if sr==1; % sample rate
        Fs = textscan(header{l}, '%s %f' , 1, 'delimiter' , '\t');
    end
    tt = strfind(header{l}, 'Total Time (s):');
    if tt==1; % total measurement time
        tmt = textscan(header{l}, '%s %f' , 1, 'delimiter' , '\t');
    end
end

% sample frequency
sampleFrequency = Fs{2};

% create time column
timedata = [0:1/sampleFrequency:tmt{2}-(1/sampleFrequency)]';
```

```

% timedata=newData.data(:,1); % if there is a time column in fileToread

% create data vectors with removed dc-offset
det1 = newData.data(:,2)-mean(newData.data(:,2));
det2 = newData.data(:,3)-mean(newData.data(:,3));

```

Fit and subtract (modulated) peak

```

%% fit (modulated) peak

clear all
close all

% number the figures
figNum = 0;

% set paths for data files and file names
measdataPath = 'path to data\';
dataFile= 'filename1.txt';

% set paths for vacuum reference files and file names
vacuumrefPath = 'path to vacuum reference data\';
vacFile = 'filename2.txt';

% make directory to save figures
mkdir([measdataPath, 'figures']);

%% import or load measurement data

% % import LabView text file
% display('import measurement data')
% [timedata,det1,det2,sampleFrequency] = ...
%     LabViewDataImport([measdataPath,dataFile]);
% % save data
% save([measdataPath,'timedata.mat'],'timedata');
% save([measdataPath,'det1.mat'],'det1');
% save([measdataPath,'det2.mat'],'det2');
% save([measdataPath,'sampleFrequency.mat'],'sampleFrequency');

% load data as created by LabViewDataImport.m
display('load measurement data')

load([measdataPath,'timedata.mat']);
load([measdataPath,'sampleFrequency']);
load([measdataPath,'det1.mat']);
load([measdataPath,'det2.mat']);

%% import or load vacuum reference data

```

```

%% import LabView text file
% display('import vacuum reference data')
% [~,vac1,vac2,~] = LabViewDataImport([vacuumrefPath,vacFile]);
%% save data
% save([vacuumrefPath,'vac1.mat'],'vac1');
% save([vacuumrefPath,'vac2.mat'],'vac2');

% load vacuum reference data as created by LabViewDataImport.m
display('load vacuum reference data')

load([vacuumrefPath,'vac1.mat']);
load([vacuumrefPath,'vac2.mat']);

%% plot time domain data
display('plot time domain data')

centerTime = timedata(ceil(length(timedata)/2));
lambdaSignal = 1/500; % signal wavelength (only used here for plotting)

figNum = figNum+1; figure(figNum);
plot(timedata,det1,timedata,det2);
xlim([centerTime-(5*lambdaSignal),centerTime+(5*lambdaSignal)]);
title('time domain data');
xlabel('time [s]'); ylabel('amplitude [V]');
legend('BHD1','BHD2');

%% compute psd
display('compute psd')

window = ones(1,length(det1));

[m1aSpec,F] = pwelch(det1>window,[],[],sampleFrequency,'onesided');
[m2aSpec,~] = pwelch(det2>window,[],[],sampleFrequency,'onesided');

%% plot psd
display('plot psd')

figNum = figNum+1; figure(figNum);
semilogy(F,m1aSpec,F,m2aSpec);
xlim([10,2000]);
title('power spectral density (without windowing or averaging)');
xlabel('frequency [Hz]'); ylabel('PSD [W/Hz]');
legend('BHD1','BHD2');

%% find excess noise in BHD2 data
display('find excess noise')

% define threshold as factor*max of vacuum measurement

```

```

window = ones(1,length(det1));
[v1aSpec,Fvac] = pwelch(vac1>window,[],[],sampleFrequency,'onesided');
threshold = 1.3*max(v1aSpec(Fvac<2000)); % cut search above 2000Hz

% find excess noise frequencies
excessNoiseInd = find(m2aSpec(F<2000)>threshold);
excessNoiseFrequencies = F(excessNoiseInd);
%(optional: use smoothed (sgolayfilt) data)
% excessNoiseInd = find(sgolayfilt(m2aSpec(F<2000),12,21)>threshold);

% set excess noise frequency range for later bounds
freqRange = [min(excessNoiseFrequencies),max(excessNoiseFrequencies)];
% maxLambdaSignal = 1/min(excessNoiseFrequencies);

% group excess noise frequencies to peaks by grouping neighboring points:
freqStep = F(2)-F(1);
% initialize some parameters
peakInd = 1;
% initialize to maximum possible length
peakFrequencies = zeros(1,length(excessNoiseFrequencies));
peakFrequencies(1) = excessNoiseFrequencies(1);
peakWidth = ones(1,length(excessNoiseFrequencies));
% group frequencies
for exNInd = 1:length(excessNoiseFrequencies)-1;

    if(excessNoiseFrequencies(exNInd+1)-...
        excessNoiseFrequencies(exNInd)==freqStep)
        peakFrequencies(peakInd) = peakFrequencies(peakInd) + ...
            excessNoiseFrequencies(exNInd+1);
        peakWidth(peakInd) = peakWidth(peakInd)+1;
    else
        peakInd = peakInd+1;
        peakFrequencies(peakInd) = excessNoiseFrequencies(exNInd+1);
    end

end

% set center frequencies as peak frequencies, reduce length
peakFrequencies = peakFrequencies(1:peakInd)./peakWidth(1:peakInd);

%% define center peak and find mean most frequent distance of the peaks
display('determine center frequency and peak distances')

centerFrequency = sum(peakFrequencies)/length(peakFrequencies);

diffPeakFrequencies = diff(peakFrequencies);

step = 1; % in Hz
binVector = min(diffPeakFrequencies):step:max(diffPeakFrequencies);
[counts, bins] = histc(diffPeakFrequencies,binVector);

```

```

[~,maxCountBinIndex]=max(counts);
meanPeakDistance = mean(diffPeakFrequencies(bins==maxCountBinIndex));

if isnan(meanPeakDistance);
    meanPeakDistance=0;
end

%% plot PSD of BHD2 data and threshold
display('plot PSD of BHD2 data and threshold')

figNum = figNum+1; figure(figNum);
semilogy(F,m2aSpec,F,ones(1,length(F))*threshold,'r');
xlim([250,1250]); ylim([1e-9,0.5e-5])
xlabel('frequency [Hz]');
ylabel('PSD [W/Hz]');
legend('BHD2 data','threshold')

%% fit BHD2 data with (modulated) sine
% fit with modulated sine and all parameters free
display('fit BHD2 data and subtract model')

% set fit options
opts2=optimset('Display','off','MaxFunEvals',10000,'MaxIter',10000,...
    'TolFun',1e-9,'TolX',1e-9);

if length(peakFrequencies)==1; % simple peak
    % define model for scatter signal at BHD2
    signal2 = @(x,xdata) x(1)*sin(x(2)*2*pi*xdata+x(3));
    % set boundaries
    p02 = [max(det2)/2,centerFrequency,0];
    lb2 = [min(det2),freqRange(1),-2*pi];
    ub2 = [max(det2),freqRange(2),2*pi];
else % modulated peak
    % define model for scatter signal at BHD2
    signal2 = @(x,xdata) x(1)*sin(x(2)*2*pi*xdata + x(3) + ...
        (x(4)*sin(x(5)*2*pi*xdata + x(6))) );
    % set boundaries (centerFrequency,meanPeakDistance)
    p02 = [max(det2)/2,centerFrequency,0,1,meanPeakDistance,0];
    lb2 = [min(det2),0,-2*pi,-Inf,2*freqStep,-2*pi];
    ub2 = [max(det2),2000,2*pi,Inf,2000,2*pi];
end

% define optimization problem
problem2 = createOptimProblem('lsqcurvefit','x0',p02,'objective',...
    signal2,'xdata',timedata,'ydata',det2,'lb',lb2,'ub',ub2,...
    'options',opts2);

% use multiple start points to find global minimum
ms = MultiStart;

% run the fit

```

```

params2 = run(ms, problem2, 1);
save([measdataPath, 'params2.mat'], 'params2');

%% subtract fit from Bobs measurement data

subtrData2 = det2-signal2(params2, timedata);

%% plot time data, fit and subtraction
display('plot subtracted BHD2 time domain data')

figNum = figNum+1; figure(figNum);

BHD2sub=plot(timedata, det2, timedata, subtrData2, timedata, ...
    signal2(params2, timedata));
xlim([0, 0.2]);
legend('measurement data BHD2', 'subtracted data', 'scatter model BHD2')
title('time domain data');
xlabel('time [s]'); ylabel('amplitude [V]');
legend('BHD2 data', 'data after subtraction', 'modeled disturbance');
saveas(gcf, [measdataPath, 'figures\'', 'SubtrTimeDomainBHD2.fig']);

%% compute spectrum of subtracted data
display('compute psd of BHD2 data after subtraction')

window = hanning(length(subtrData2)/10);

[subtrData2Spec, F1] = pwelch(subtrData2, window, [], [], ...
    sampleFrequency, 'onesided');
[m2aSpec2, ~] = pwelch(det2, window, [], [], sampleFrequency, 'onesided');

%% plot spectra of measurement and subtracted data
display('plot spectra of BHD2 data after subtraction')

figNum = figNum+1; figure(figNum);
semilogy(F1, m2aSpec2, F1, subtrData2Spec, 'r—');
xlabel('frequency [Hz]'); ylabel('PSD [W/Hz]');
xlim([250, 1250]); ylim([1e-9, 1e-6]);
legend('BHD2 data', 'data after subtraction');
saveas(gcf, [measdataPath, 'figures\'', 'SubtrBHD2Spec.fig']);

%% fit amplitude for Alice data
display('fit BHD1 data and subtract model')

% set fit options
opts1=optimset('Display', 'off', 'MaxFunEvals', 10000, 'MaxIter', 10000, ...
    'TolFun', 1e-9, 'TolX', 1e-9);

```

```

if length(peakFrequencies)==1; % simple peak
    % define scatter model for BHD1 data (fit amplitude (x) and take
    % frequency and phase of BHD2 fit (pp) )
    signal1 = @(x,xdata,pp) x*sin(pp(1)*2*pi*xdata+pp(2));
    % set boundaries
    p01 = max(det1)/2;
    lb1 = min(det1);
    ub1 = max(det1);
else % modulated peak
    % define scatter model for BHD1 data (fit amplitude (x) and take
    % frequency and phase of BHD2 fit (pp) )
    signal1 = @(x,xdata,pp) x*sin(pp(1)*2*pi*xdata + pp(2) + ...
        (pp(3)*sin(pp(4)*2*pi*xdata + pp(5))) );
    % set boundaries
    p01 = max(det1)/2;
    lb1 = min(det1);
    ub1 = max(det1);
end

% define optimization problem
problem1 = createOptimProblem('lsqcurvefit','x0',p01,...
    'objective',@(a,b)signal1(a,b,params2(2:end)), 'xdata',timedata,...
    'ydata',det1,'lb',lb1,'ub',ub1,'options',opts1);

% use multiple start points to find global minimum
ms = MultiStart;

% run the fit
params1 = run(ms,problem1,1);
save([measdataPath,'params1.mat'],'params1');

%% subtract fit from Alices measurement data

subtrData1 = det1-signal1(params1,timedata,params2(2:end));

%% plot time data, fit and subtraction
display('plot subtracted BHD1 time domain data')

figNum = figNum+1; figure(figNum);
BHD1sub = plot(timedata,det1,timedata,subtrData1,timedata,...
    signal1(params1,timedata,params2(2:end)));
xlim([0,0.2]);
legend('BHD1 data','data after subtraction','modeled disturbance')
saveas(gcf,[measdataPath,'figures\','SubtrTimeDomainBHD1.fig']);

%% compute spectrum of subtracted BHD1 data
display('compute spectra of subtracted BHD1 data')

window = hanning(length(subtrData1)/10);

```

```

[subtrData1Spec,F1] = pwelch(subtrData1,window,[],[],...
    sampleFrequency,'onesided');
[m1aSpec2,~] = pwelch(det1,window,[],[],sampleFrequency,'onesided');

%% plot spectra of measurement and subtracted data

display('plot spectra of subtracted BHD1 data')

figNum = figNum+1; figure(figNum);
semilogy(F1,m1aSpec2,F1,subtrData1Spec,'r—');
xlabel('frequency [Hz]'); ylabel('PSD [W/Hz]');
xlim([250,1250]); ylim([1e-9,1e-6])
legend('BHD2 data','data after subtraction');

saveas(gcf,[measdataPath,'figures\','SubtrBHD1Spec.fig']);

```

Fit and subtract scatter shoulder (with multiple round-trips)

```

% fit scatter shoulder (with multiple round-trips)

clear all; close all;
fignum = 0; % to number the figures

measdata = 'data filename.txt';
vacuumref = 'vacuum reference filename.txt';

%% create folder to save plots
[pathstr,name,~] = fileparts(measdata);
plotpath = [pathstr,'\',name,'Plots\'];
mkdir(plotpath);

%% import or load measurement data

%% import LabView text file
% display('import measurement data')
% [timedata,det1,det2,sampleFrequency] = LabViewDataImport(measdata);
%% save data
% save([pathstr,'timedata.mat'],'timedata');
% save([pathstr,'det1.mat'],'det1');
% save([pathstr,'det2.mat'],'det2');
% save([pathstr,'sampleFrequency.mat'],'sampleFrequency');

% load data as created by LabViewDataImport.m
display('load measurement data')

load([pathstr,'timedata.mat']);

```



```

load ([pathstr, 'sampleFrequency']);
load ([pathstr, 'det1.mat']);
load ([pathstr, 'det2.mat']);

%% import or load vacuum reference data

%% import LabView text file
% display('import vacuum reference data')
% [~,vac1,vac2,~] = LabViewDataImport(vacuumref);
%% save data
% save([pathstr, 'vac1.mat'], 'vac1');
% save([pathstr, 'vac2.mat'], 'vac2');

% load vacuum reference data as created by LabViewDataImport.m
display('load vacuum reference data')

load ([pathstr, 'vac1.mat']);
load ([pathstr, 'vac2.mat']);

%% provide start parameters for modulation depth m, frequency fm
% and phase phim

trialFrqs = [ ]; % set trial frequency vector
[m, fm, phim] = FitArches(timedata, det2, sampleFrequency, trialFrqs);

%% filter and downsample data for fitting

nrt=3; % number of additional round trips to consider for the
% back-scattered beam (for lp-filtering)

% use averaged data:
% wavelength corresponding to max Doppler shift frequency
lambdamdl = sampleFrequency/((nrt+1)*m*fm);
% number of neighbouring points to average, chosen to be a 10th of the
% shortest expected wavelength
navpt = round(lambdamdl/10);
% Nyquist frequency
fny = floor(0.5*sampleFrequency/navpt);

% design filter
lpFilt = designfilt('lowpassiir', 'FilterOrder', 10, ...
    'PassbandFrequency', 0.5*fny, 'PassbandRipple', 0.001, ...
    'SampleRate', sampleFrequency);
% this way more than 60dB suppression at fny=0.5*fs_new;
% fs_new=sampleFrequency/navpt; and PassbandFreq ~ 2.5*f_maxDopplerShift;

% fvtool(lpFilt); % display filter

filtdet1 = filtfilt(lpFilt, det1);
filtdet2 = filtfilt(lpFilt, det2);

```

```

filtvac1 = filtfilt(lpFilt,vac1);
filtvac2 = filtfilt(lpFilt,vac2);

datalength = length(filtDET1);
% initialize averaged data vectors:
aad = zeros(1,floor(datalength/NAVPT));
abd = zeros(1,floor(datalength/NAVPT));
atd = zeros(1,floor(datalength/NAVPT));
n = 0; % initialize index

while n*NAVPT < datalength-NAVPT; % rest of data skipped
    aad(n+1) = sum(filtDET1(1+(n*NAVPT):(n+1)*NAVPT))/NAVPT;
    abd(n+1) = sum(filtDET2(1+(n*NAVPT):(n+1)*NAVPT))/NAVPT;
    atd(n+1) = timedata(1+(n*NAVPT)+round(NAVPT/2));
%     avac1(n+1) = sum(filtvac1(1+(n*NAVPT):(n+1)*NAVPT))/NAVPT;
%     avac2(n+1) = sum(filtvac2(1+(n*NAVPT):(n+1)*NAVPT))/NAVPT;
    n = n+1;
end

%% optional: choose shorter data segment for fitting

t1 = 0; t2 = timedata(end);
Iseg = atd>t1 & atd<t2; % time segment to use
atdSegment = atd(Iseg);
% remove dc-offset again
dataSegmentB = abd(Iseg)-mean(abd(Iseg));
dataSegmentA = aad(Iseg)-mean(aad(Iseg));

%% set parameters for higher order model and multistart fit of BHD2 data

clear sparam

% define multiple sets of start parameters
% sparam = [signal amplitude ,g, phi_0 ,m, fm, phim, m2, phim2 ,...
% ... (up to 5th order), quadrature offset]
sparam = zeros(18,15);
% set fixed start parameters for all sets
sparam(:,[2,4,5,15]) = repmat([0.5 ,m, fm, 0],18,1);
% combine different start values for A, phi0, phim
sparam(:,[1,3,6]) = combvec([max(det2)/2,max(det2)/2],[-pi/2,0,pi/2],...
    [phim-pi, phim, phim+pi])';
% set random phases for higher orders between a and b and
% random amplitudes between c and d
a = -2*pi; b = 2*pi;
c = -0.1*m; d = 0.1*m;
for in=8:2:14;
    sparam(:,in)=(b-a).*rand(size(sparam,1),1) + a;
    sparam(:,in-1)=(d-c).*rand(size(sparam,1),1) + c;
end
% create custom start point set
tpoints = CustomStartPointSet(sparam);

```

```

% set boundaries
lb=[min(det2),0,-2*pi,0,0,-2*pi,-Inf,-2*pi,-Inf,-2*pi,-Inf,...
    -2*pi,-Inf,-2*pi,-pi/2,-Inf];
ub=[max(det2),1,2*pi,Inf,Inf,2*pi,Inf,2*pi,Inf,2*pi,Inf,2*pi,...
    Inf,2*pi,pi/2,Inf];

% set fit options
opts=optimset('Display','off','MaxFunEvals',100000,...
    'TolFun',10^-11,'TolX',10^-11);

%% fit for higher order model to BHD2 data, using multistart

% create optimization problem
problem = createOptimProblem('lsqcurvefit','objective',...
    @(a,b)sinmodNlInf(a,b),'xdata',atdSegment,'ydata',dataSegmentB,...
    'x0',sparam(1,:),'lb',lb,'ub',ub,'options',opts);
% (sinmodNlInf: model with higher harmonics and multiple round-trips)

% run fit using MultiStart
ms = MultiStart;
[xNL,resnorm,exitflag,output,solutions] = run(ms,problem,tpoints);
% (solutions(1,1).X0{1,1} = start point for best solution)

%% save fitted parameters to mat file
% save([pathstr,'\xNL.mat'],'xNL')

%% compute BHD2 model
bobmod = sinmodNlInf(xNL,timedata);

% compute bandpower of BHD2 data after subtraction
bpbob = bandpower(det2(timedata>t1 & timedata<t2)-bobmod(timedata>t1 &...
    timedata<t2),sampleFrequency,[xNL(5) (nrt+1)*xNL(4)*xNL(5)]);

%% plot averaged BHD2 time domain data with fit

fignum = fignum+1; figure(fignum);

td1=plot(atd,abd-mean(abd),timedata,bobmod);
xlim([0,0.2]); ylim([-0.015,0.015])

set(td1(1),'Color',[0.4,0.4,0.4]);
set(td1(2),'Color',[0,85,212]/255,'LineWidth',2)
legend('BHD1 data','modeled disturbance')

xlabel('time [s]')
ylabel('amplitude [V]');

```

```

%% plot raw or subtracted BHD2 data in spectrogram

timeres = 1/(4*xNL(5));
timeresdl = round(timeres*sampleFrequency);
noverlap=round(0.9*timeresdl);
NFFT = [];

% raw data:
% [~,F,T,PAmeas] = spectrogram(det2,hanning(timeresdatalength),...
% noverlap,NFFT,sampleFrequency);

% subtracted data:
[~,F,T,PAmeas] = spectrogram(det2-bobmod,...
    hanning(timeresdl),noverlap,NFFT,sampleFrequency);

fignum = fignum+1; figure(fignum);
surf(T,F,10*log10(PAmeas));
xlim([(timeres/2),t2-(timeres/2)]);
ylim([0 1000]); zlim([-180,-60]);
xlabel('time [s]'); ylabel('frequency [Hz]');
% contourmap('MyColorMap',[-85:0.2:-70]);
% colormap(flipud(colormap));

w=colorbar;
zlab = get(w,'ylabel');
set(zlab,'String','PSD [dBW/Hz]');
shading interp
view(0,90);

% saveas(gcf,[plotpath,'tspecAmeas.eps'],'eps');
% saveas(gcf,[plotpath,'tspecAmeas.fig']);

%% fit higher order model to BHD1 data

% set start parameters [signal amplitude, quadrature offset]
sparam2 = [xNL(1),0];
% set boundaries
lb2=[min(det1),-2*pi];
ub2=[max(det1),2*pi];

% set fit options
opts=optimset('Display','off','MaxFunEvals',100000,...
    'TolFun',10^-11,'TolX',10^-11);

% create optimization problem
problem = createOptimProblem('lsqcurvefit','objective',...
    @(a,b)cosmodNlInfA(xNL,b,a),'xdata',atdSegment,'ydata',dataSegmentA,...
    'x0',sparam2,'lb',lb2,'ub',ub2,'options',opts);
% (cosmodNlInfA: model with higher harmonics and multiple round-trips)

% run fit using MultiStart

```

```

ms = MultiStart;
[xNLa, fval2, exitflag2, output2, solutions2] = run(ms, problem, 5);
% (solutions(1,1).X0{1,1} = start point for best solution)

%% compute BHD1 model

alicemod = cosmodNlInfA(xNL, timedata, xNLa);

%% compute bandpower
bpalice = bandpower(det1(timedata>t1 & timedata<t2)-alicemod...
    (timedata>t1 & timedata<t2), sampleFrequency, ...
    [xNL(5) (nrt+1)*xNL(4)*xNL(5)]);

%% plot averaged BHD1 time domain data with fit

fignum = fignum+1; figure(fignum);
td2=plot(atd, aad-mean(aad), timedata, alicemod);
xlim([0, 0.2]); ylim([-0.015, 0.015])

set(td2(1), 'Color', [0.4, 0.4, 0.4]);
set(td2(2), 'Color', [0, 85, 212]/255, 'LineWidth', 2)
legend('BHD2 data', 'modeled disturbance')

xlabel('time [s]')
ylabel('amplitude [V]');

% save found fit parameters to mat file
% save('DataMatFiles\2HzFullxNLQuadCorFilterInf.mat', 'xNLa')

%% plot raw or subtracted alice data in spectrogram

timeres = 1/(4*xNL(5));
timeresdl = round(timeres*sampleFrequency);
noverlap=round(0.9*timeresdl);
NFFT = [];

% raw data:
% [~, F, T, PAmeas] = spectrogram(det1, hanning(timeresdatalength), ...
% noverlap, NFFT, sampleFrequency);

% subtracted data:
[~, F, T, PAmeas] = spectrogram((det1-mean(det1))-alicemod, ...
    hanning(timeresdl), noverlap, NFFT, sampleFrequency);

fignum = fignum+1; figure(fignum);
surf(T, F, 10*log10(PAmeas));
xlim([(timeres/2), t2-(timeres/2)]);
ylim([0 1000]); zlim([-180, -60]);
xlabel('time [s]'); ylabel('frequency [Hz]');
% contourmap('MyColorMap', [-85:0.2:-70]);

```

```

% colormap( flipud( colormap ) );

w=colorbar;
zlab = get(w, 'ylabel');
set(zlab, 'String', 'PSD [dBW/Hz]');
shading interp
view(0,90);

% saveas(gcf, [plotpath, 'tspecAmeas.eps'], 'epsc');
% saveas(gcf, [plotpath, 'tspecAmeas.fig']);

%% compute averaged spectra for the data segment used in the fit

% set datalength for required RBW != 2*f_sc
lambdamdl = round(sampleFrequency/xNL(5));
adl = round(lambdamdl/2);
noverlap = [];
NFFT = [];

% compute averaged spectra with pwelch function
% measurement data
[shAmeas, fsh] = pwelch(det1(timedata>t1 & timedata<t2), ...
    hanning(adl), noverlap, NFFT, sampleFrequency, 'onesided');
[shBmeas, ~] = pwelch(det2(timedata>t1 & timedata<t2), ...
    hanning(adl), noverlap, NFFT, sampleFrequency, 'onesided');
% model
[shAmod, ~] = pwelch(alicemod(timedata>t1 & timedata<t2), ...
    hanning(adl), noverlap, NFFT, sampleFrequency, 'onesided');
[shBmod, ~] = pwelch(bobmod(timedata>t1 & timedata<t2), ...
    hanning(adl), noverlap, NFFT, sampleFrequency, 'onesided');
% measurement data with model subtracted
[shAsub, ~] = pwelch(det1(timedata>t1 & timedata<t2)-alicemod...
    (timedata>t1 & timedata<t2), hanning(adl), noverlap, NFFT, ...
    sampleFrequency, 'onesided');
[shBsub, ~] = pwelch(det2(timedata>t1 & timedata<t2)-bobmod...
    (timedata>t1 & timedata<t2), hanning(adl), noverlap, NFFT, ...
    sampleFrequency, 'onesided');
% vacuum references
[shAvac, ~] = pwelch(vac1(timedata>t1 & timedata<t2), ...
    hanning(adl), noverlap, NFFT, ...
    sampleFrequency, 'onesided');
[shBvac, ~] = pwelch(vac2(timedata>t1 & timedata<t2), ...
    hanning(adl), noverlap, NFFT, ...
    sampleFrequency, 'onesided');

%% plot averaged spectra for BHD1

fignum = fignum+1; fas = figure(fignum);

```

```

has = loglog(fsh,shAmeas,fsh,shAsub,fsh2,smooth(shAvac));
set(has(1),'Color',[0,85,212]/255)
set(has(2),'Color',[212,0,0]/255);
set(has(3),'Color',[0.4,0.4,0.4]);

xlim([2*xNL(5) 2000]);
ylim([2e-9,0.5e-6]);
legend('measurement data','data after subtraction',...
       'shot noise reference')

grid on; set(gca,'GridLineStyle','-');
xlabel('frequency [Hz]');
ylabel('PSD [W/Hz]');

%% plot averaged spectra for BHD2

fignum = fignum+1; fbs = figure(fignum);

hbs = loglog(fsh,shBmeas,fsh,shBsub,fsh2,smooth(shBvac));
set(hbs(1),'Color',[0,85,212]/255)
set(hbs(2),'Color',[212,0,0]/255);
set(hbs(3),'Color',[0.4,0.4,0.4]);

xlim([2*xNL(5) 2000]);
set(gca,'XTickLabel',[100,1000]);
ylim([1e-9,0.5e-6]);
legend('measurement data','data after subtraction',...
       'shot noise reference')

grid on; set(gca,'GridLineStyle','-');
xlabel('frequency [Hz]');
ylabel('PSD [W/Hz]');

```

Fit Doppler shift to arches in spectrogram data

```

function [m,fm,phim] = FitArches(timedata,det2,sampleFrequency,trialFrqs)
% determine reduced paramter set [m,fm,phim] from Doppler shift in
% spectrogram data

%% define Doppler shift models

% model for the time dependent Doppler shift: % y = [m,phim] frq=fm
modfdst=@(y,ydata,frq) abs(y(1)*frq*cos(2*pi*frq*ydata+y(2)));

% model for the time dependent Doppler shift: % y = [m,fm,phim]
modfdstAll=@(y,ydata) abs(y(1)*y(2)*cos(2*pi*y(2)*ydata+y(3)));

%% fit m, fm and phim from BHD2 spectrogram max frequency components

```

```

% set boundaries for [A,phim]
lb = [0,-2*pi];
ub = [Inf,2*pi];

% set start parameters for [A,phim]
sparam = [1,0];

% set fit options to suppress output
opts=optimset('Display','off');

% search frequency with minimum resnorm for the [A,phim] fit:

% initialize parameters
spar=zeros(length(trialFrqs),length(sparam));
meansqrResnorm=zeros(1,length(trialFrqs));

for fri=1:length(trialFrqs);
    % set time/frequency resolution for computation of time dependent
    % spectra
    timeres = 1/(4*trialFrqs(fri));
    timeresdl = round(timeres*sampleFrequency);
    noverlap = round(0.9*timeresdl);
    [~,f,time,psbds] = spectrogram(det2,hamming(timeresdl),...
        noverlap,[],sampleFrequency);
    % find max frequency components
    [~,I] =max(psbds,[],1);
    fdst = f(I)';
    % fit Doppler shift to arches
    [spar(fri,:),~,residual] = lsqcurvefit(@(a,b)...
        modfdst(a,b,trialFrqs(fri)),sparam,time,fdst,lb,ub,opts);
    meansqrResnorm(fri)=mean(sqrt(residual.^2));
end

%% find minimum for meansqrResnorm(fm)

[mi,fI] = findpeaks(-meansqrResnorm,'sortstr','descend');
if isempty(mi)
    error('No minimum found. Refine search.')
end

%% plot resnorm(frv) to check the computed frequency
% figure;
% plot(trialFrqs,meansqrResnorm)

%% fit again with all three parameters free

% set new start parameters
m = spar(fI(1),1);
fm = trialFrqs(fI(1));
phim = spar(fI(1),2);

```



```

% compute time dependent doppler frequency again with adjusted resolution
timeres = 1/(4*fm); % in seconds
timeresdl = round(timeres*sampleFrequency);
noverlap = round(0.9*timeresdl);
[~,f,time,psbds] = spectrogram(det2,hamming(timeresdl),noverlap,...
    [],sampleFrequency);

% find max frequency components
 [~,I] =max(psbds,[],1);
fdst = f(I)';

% remove outliers with more than one standard deviation/2 distance from
% the fitted model
I2 = abs(modfdst([m,phim],time,fm) - fdst) < 0.5*std(fdst);
fdst2 = excludedata(time,fdst,'indices',I2);

% set boundaries for [A,fm,phim]
lb2 = [-Inf,0.1,-2*pi];
ub2 = [Inf,Inf,2*pi];

% fit again with all three parameters free
[spar2,~] = lsqcurvefit(@modfdstAll(a,b),[m,fm,phim],...
    time(fdst2),fdst(fdst2),lb2,ub2,opts);

% set new start parameters
m = spar2(1);
fm = spar2(2);
phim = spar2(3);

%% plot fit

figure;
arches = plot(timedata,modfdst([m,phim],timedata,fm),'-',time,...
    fdst,'*', 'LineWidth',2);
set(arches(1),'Color',[0,85,212]/255)
set(arches(2),'Color','k');
xlim([0,1]); %ylim([0,max(fdst)+30]);

xlabel('time [s]'); ylabel('frequency [Hz]')
legend(' {\it f} - {\fontsize{8} ds}(t) fit ', ' max data ');

```

Higher order models for infinite round-trips

```
function mod=sinmodNlInf(x, xdata)

% psi with higher harmonics up to 5th order
psi = x(3) + (x(4)*sin(2*pi*x(5)*xdata+x(6)) + ...
    (x(7)*sin(2*pi*x(5)*xdata+x(6)-(x(8))).^2) + ...
    (x(9)*sin(2*pi*x(5)*xdata+x(6)-(x(10))).^3) + ...
    (x(11)*sin(2*pi*x(5)*xdata+x(6)+x(12)).^4) + ...
    (x(13)*sin(2*pi*x(5)*xdata+x(6)+x(14)).^5) );

% model for infinite round-trips
mod = -x(1)*((sin(psi+x(15))+x(2)*sin(x(15)))) ./ ...
    ((1+(x(2)*cos(psi)).^2+(x(2)*sin(psi)).^2));

mod = mod-mean(mod); % center around zero

function mod=cosmodNlInfA(x, xdata, y)
% fit y and use x from other quadrature fit

psi = x(3) + (x(4)*sin(2*pi*x(5)*xdata+x(6)) + ...
    (x(7)*sin(2*pi*x(5)*xdata+x(6)-(x(8))).^2) + ...
    (x(9)*sin(2*pi*x(5)*xdata+x(6)-(x(10))).^3) + ...
    (x(11)*sin(2*pi*x(5)*xdata+x(6)+x(12)).^4) + ...
    (x(13)*sin(2*pi*x(5)*xdata+x(6)+x(14)).^5) );

% model for infinite round-trips
mod = y(1)*(((cos(psi+x(15)+y(2))+x(2)*cos(x(15)+y(2)))) ./ ...
    ((1+(x(2)*cos(psi)).^2+(x(2)*sin(psi)).^2) ));

mod = mod-mean(mod); % center around zero
```

C. Cancellation of lateral displacement noise of three-port gratings for coupling light to cavities

Here I present experimental results which were off topic with the rest of my work. The content of this section corresponds to a publication in *Optics Letters* [36].

Abstract Reflection gratings enable light coupling to optical cavities without transmission through substrates. Gratings that have three ports and are mounted in second-order Littrow configuration even allow the coupling to high-finesse cavities using low diffraction efficiencies. In contrast to conventional transmissive cavity couplers, however, the phase of the diffracted light depends on the lateral position of the grating, which introduces an additional noise coupling. Here we experimentally demonstrate that this kind of noise cancels out once both diffracted output ports of the grating are combined. We achieve the same signal-to-shot-noise ratio as for a conventional coupler. From this perspective, 3-port grating couplers in second-order Littrow configuration remain a valuable approach to reducing optical absorption of cavity coupler substrates in future gravitational wave detectors.

C.1. Introduction

Coupling light to an optical cavity is usually realized via partially transmissive mirrors. 3-port reflection gratings represent a practical alternative, which does not require light transmission through substrate material [64–74]. This avoids light absorption in substrates and consequently even allows opaque substrates. Due to this advantage reflection gratings were considered as optical components in gravitational-wave detectors already 20 years ago [75]. Fig. C.1 shows an example how (a) conventional couplers to arm cavities in a Michelson interferometer can be replaced with (b) weak diffraction efficiency gratings in second-order Littrow configuration [65–67, 70–74]. Unfortunately it turned out that lateral grating displacements that are parallel to its surface and perpendicular to the grating’s grooves cause phase shifts on the diffracted light field and thus introduce a new noise coupling [72, 76]. This contrasts a conventional mirror that is displaced parallel to its surface. It thus seems that gratings need to have a better isolation from environmental disturbances than conventional mirrors [77].

In this work we experimentally show that the unwanted lateral-displacement-to-phase coupling in grating interferometers can be canceled by an appropriate combination of

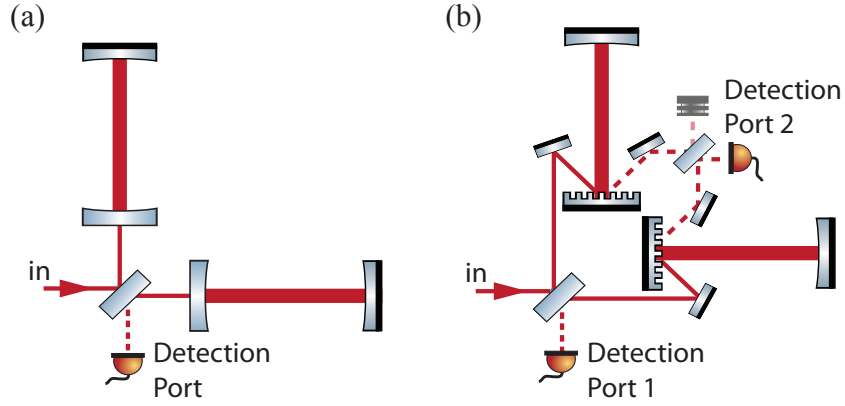


Figure C.1.: Michelson interferometers with arm resonators. (a) Michelson-type laser interferometer with conventional, transmissively coupled Fabry-Perot arm cavities. (b) Equivalent interferometer topology with arm cavities that are diffractively coupled in second-order Littrow configuration. Here, the phase signal that is acquired in an arm cavity couples out via two ports of the grating. We show that summing up the photo-electric currents as shown not only recovers the full signal-to-shot-noise ratio but also cancels out phase noise due to lateral grating motions.

detection ports. We realize a simplified setup in which a phase-modulated light beam is sent under normal incidence to a grating, whose position is continuously changed perpendicular to its grooves and to the optical axis of the incident light. We detect the phase modulations in the \pm first diffraction orders and demonstrate that summing up the photo-electric currents not only retains the full signal-to-shot-noise ratio but also cancels out phase noise due to the lateral grating motion.

C.2. Experimental setup

The schematic of the experimental setup is depicted in Fig. C.2. Our 3-port diffraction grating had a size of 10 mm x 10 mm and was realized on a quartz substrate with a size of 1" x 1" x 0.25". The grating was realized using electron beam lithography to define the grating pattern into a resist layer. Afterwards this pattern was transferred by an inductively-coupled plasma etching process (ICP) into a chromium and subsequently into the uppermost silica layer. The first-order diffraction efficiencies at normal incidence were measured to be about 4.8% at 1064 nm. The normal incidence light beam had a power of 7 mW, which resulted in 0.34 mW in the $m = \pm 1$ diffraction orders. The input light was modulated at a frequency of 710 kHz by an electro-optic modulator (EOM), which served as a scientific phase signal corresponding to a ‘gravitational-wave’-signal. Two balanced homodyne detectors (BHD1&2) measured the phase quadrature amplitudes of the first-order diffracted outputs. Each BHD was stabilized to this quadrature by using the difference of its photo diodes’ DC voltage as an error signal and by feeding back to a piezo-actuated mirror in the path of the local oscillator beam (DC-lock). The unity gain frequencies for these locks were far below the frequencies of the injected sig-

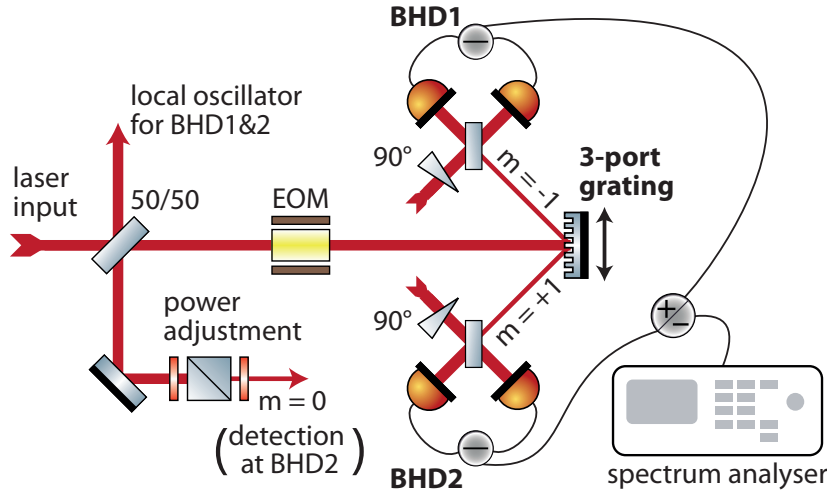


Figure C.2.: Experimental setup. We performed a phase measurement of the $m = \pm 1$ diffraction orders of a 3-port grating with two balanced homodyne detectors (BHD1&2). The sum and difference of both signals were acquired with a spectrum analyzer. The position of the grating was modulated in the lateral direction, using a piezo actuator. An electro-optic modulator (EOM) periodically shifted the phase of the incident light, serving as a reference ‘gravitational-wave’-signal. Part of the zero order diffracted light was picked off at a 50/50 beam splitter and (optionally) detected with BHD2 to confirm the lateral displacement of the grating.

nals and the signs for the quadratures were chosen in such a way that the radio-frequency EOM signal added when combining the BHD photo currents. The BHDs’ local oscillator powers were 10 mW. The individual BHD photo currents, as well as their sum (or difference) were analyzed with a spectrum analyzer. The grating was piezo actuated and modulated in the lateral direction at a frequency of about 683 kHz in order to produce the disturbance phase signal under investigation here. The frequency of about 683 kHz was selected because the piezo-actuated grating including its mount showed a pure lateral displacement in this case; any motion in direction of the incident laser beam was not visible, i.e. was far below the shot-noise level of our setup.

Fig. C.3 shows the individual measurements of the $m = \pm 1$ diffraction orders at the respective detectors BHD1&2 (solid green lines). The disturbances from the lateral grating displacement and the scientific EOM signals are clearly visible. The broadband noise floor in our measurements was given by optical shot-noise. The transfer functions of the BHDs were almost identical and produced a marginal slope on the otherwise white shot noise. To confirm that the grating signal was solely due to lateral displacement, we also analyzed the zero order diffraction. The result is shown in Fig. C.3 (bottom, dashed orange line). This measurement was done by picking off part of the zero order diffracted beam at a 50/50 beam splitter in the input path, adjusting the power to the same level as in the $m = \pm 1$ diffraction orders and detecting it with BHD2 (via flip mirror). The measurement confirms that the grating signal vanished in zero order diffraction while the

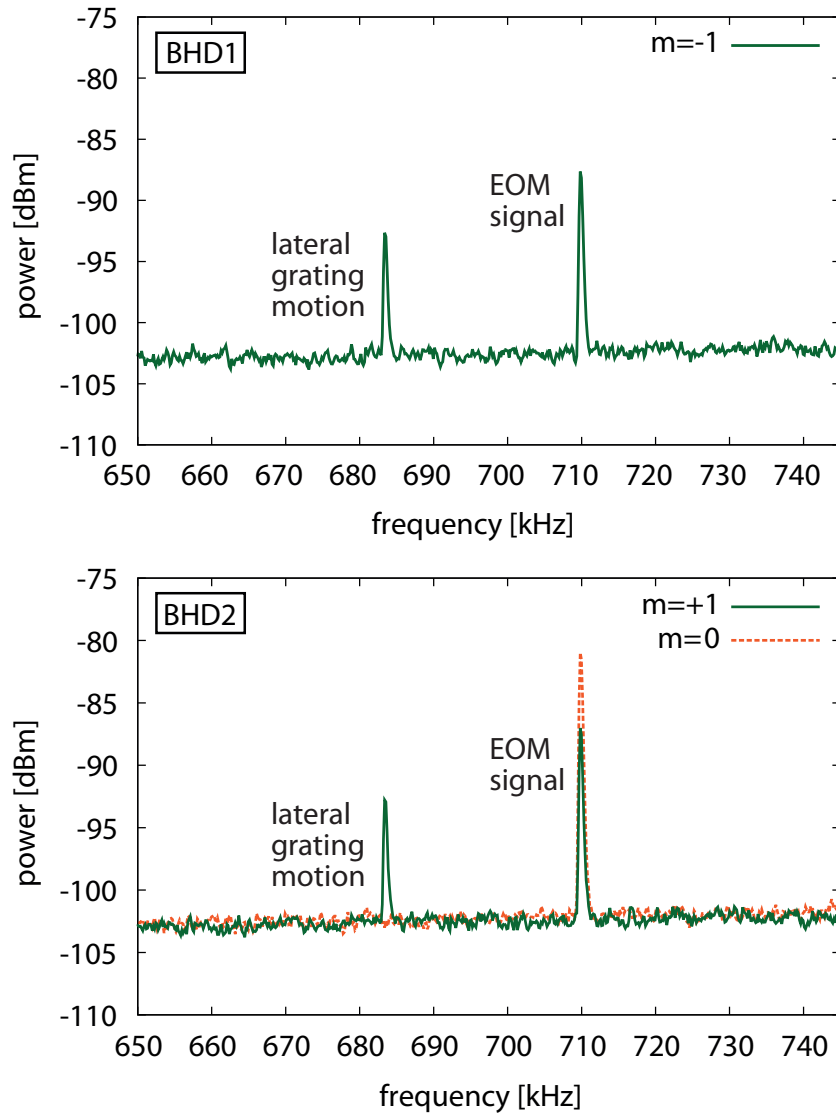


Figure C.3.: Individual diffraction orders. Shown are the power spectra of the $\pm 1^{\text{st}}$ diffraction orders (solid green) and the 0^{th} order (dashed orange) as measured by BHD1&2, respectively. During all these measurements the grating was laterally displaced at a frequency of about 683 kHz and a phase modulation at 710 kHz was imprinted on the input light by an electro-optic modulator (EOM). The disturbance from the grating displacement is clearly visible in the measurements on the $\pm 1^{\text{st}}$ diffraction orders. As expected it is not present in the 0^{th} order. (resolution bandwidth (RBW): 300 Hz; video bandwidth (VBW): 10 Hz; averaged 16 times).

reference EOM-signal was clearly visible. As expected, the measured EOM-signal was in fact about 6 dB larger than in the first-order diffracted outputs, because the zero order light passed the EOM twice. The modulations during the passages were approximately in phase because the wavelength of the kHz-signal was much larger than the optical path

between the grating and the EOM. The modulation amplitude was therefore doubled and in the depicted power spectrum thus resulted in a factor of 4 or 6 dB accordingly.

C.3. Measurement results

In Fig. C.4 the sum (red) and difference (blue) of the two homodyne measurements are depicted. Since the optical shot-noise measured at the two detectors is uncorrelated, it adds up in variance and the noise floor was increased by 3 dB in these measurements. As expected, the phase modulation from the lateral displacement of the grating cancels in the sum of the outputs while the amplitude of the scientific signal from the EOM adds up.

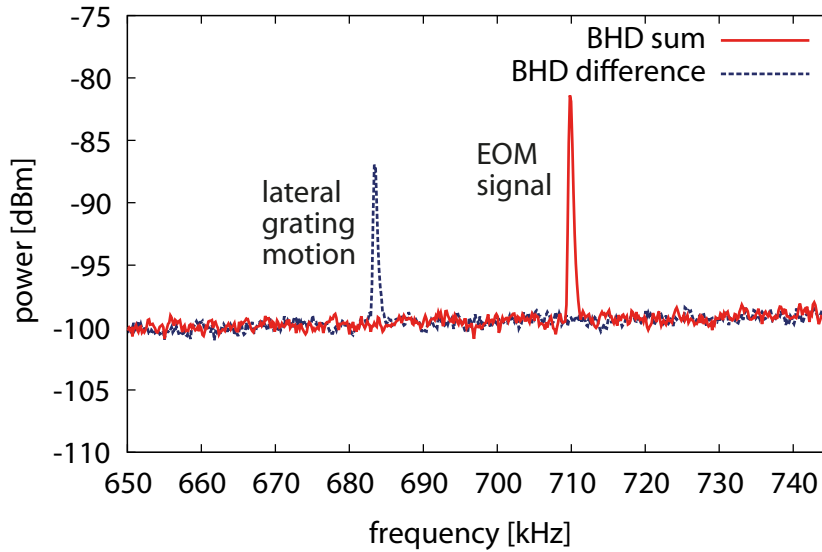


Figure C.4.: Combination of the $\pm 1^{\text{st}}$ diffraction orders. Shown are the spectra of the sum (red) and difference (blue) of the $m = \pm 1$ diffraction orders, measured by BHD1&2. The disturbance signal that was produced by lateral displacement of the grating clearly vanished in the *sum*, corresponding to a cancellation of the lateral-displacement-to-phase coupling of the grating. As expected, the phase modulation imprinted on the incident beam by the EOM increased by 6 dB in this case. On the contrary, the difference photo current shows an increase of the disturbance signal and a completely vanished scientific phase signal. As expected for shot-noise limited measurements, the shot-noise level increased by 3 dB in either case.

C.4. Conclusion

In conclusion, using a simplified setup, we have experimentally demonstrated the cancellation of interferometric disturbance signals that result from lateral displacements of gratings. We considered the case in which a 3-port reflection grating mounted in

second order Littrow configuration served as a cavity coupler, which corresponded to an arrangement that is potentially interesting for future gravitational wave detectors (Fig. C.1 (b)). When the output ports were combined in a way that optimized the signal-to-shot-noise, the disturbance signals from lateral grating displacements canceled completely with respect to the shot noise of our setup. Our result suggests that phase noise from lateral displacement of 3-port gratings can be canceled to a high degree and that no additional demands on the suspensions are required, as long as both diffracted outputs are being detected.

Bibliography

- [1] A. Einstein, “Die Grundlage der allgemeinen Relativitätstheorie,” *Annalen der Physik*, vol. 49, pp. 769–822, 1916.
- [2] J. A. Wheeler, *Geons, Black Holes, and Quantum Foam: A Life in Physics*. W. W. Norton & Company, 1998, ch. The Force of Gravity, p. 235.
- [3] A. Einstein, *Sitzungsberichte der preuss. Akademie der Wissenschaften*, vol. 1, p. 688, 1916.
- [4] ———, “Über Gravitationswellen,” *Sitzungsberichte der preuss. Akademie der Wissenschaften*, vol. 1, pp. 154–167, 1918.
- [5] R. A. Hulse and J. H. Taylor, “Discovery of a pulsar in a binary system,” *Astrophys. J.*, vol. 195, 1975.
- [6] J. H. Taylor and J. M. Weisberg, “A new test of general relativity - Gravitational radiation and the binary pulsar PSR 1913+16,” *Astrophys. J.*, vol. 253, p. 908, 1982.
- [7] The LIGO Scientific Collaboration, “Observation of Gravitational Waves from a Binary Black Hole Merger,” *Phys. Rev. Lett.*, vol. 116, p. 061102, Feb 2016. [Online]. Available: <http://link.aps.org/doi/10.1103/PhysRevLett.116.061102>
- [8] ———, “Advanced LIGO,” *Classical and Quantum Gravity*, vol. 32, no. 7, p. 074001, 2015. [Online]. Available: <http://stacks.iop.org/0264-9381/32/i=7/a=074001>
- [9] F. Acernese et al., “Advanced Virgo: a second-generation interferometric gravitational wave detector,” *Classical and Quantum Gravity*, vol. 32, no. 2, p. 024001, 2015. [Online]. Available: <http://stacks.iop.org/0264-9381/32/i=2/a=024001>
- [10] C. Affeldt, K. Danzmann, K. L. Dooley, H. Grote, M. Hewitson, S. Hild, J. Hough, J. Leong, H. Lück, M. Prijatelj, S. Rowan, A. Rüdiger, R. Schilling, R. Schnabel, E. Schreiber, B. Sorazu, K. A. Strain, H. Vahlbruch, B. Willke, W. Winkler, and H. Wittel, “Advanced techniques in GEO 600,” *Classical and Quantum Gravity*, vol. 31, no. 22, p. 224002, 2014. [Online]. Available: <http://stacks.iop.org/0264-9381/31/i=22/a=224002>
- [11] Y. Aso, Y. Michimura, K. Somiya, M. Ando, O. Miyakawa, T. Sekiguchi, D. Tatsumi, and H. Yamamoto, “Interferometer design of the KAGRA gravitational

- wave detector,” *Phys. Rev. D*, vol. 88, p. 043007, 2013. [Online]. Available: <https://journals.aps.org/prd/abstract/10.1103/PhysRevD.88.043007>
- [12] The LIGO Scientific Collaboration, “GW150914: The Advanced LIGO Detectors in the Era of First Discoveries,” *Phys. Rev. Lett.*, vol. 116, p. 131103, Mar 2016. [Online]. Available: <http://link.aps.org/doi/10.1103/PhysRevLett.116.131103>
- [13] C. M. Caves, “Quantum-mechanical radiation pressure fluctuations,” *Phys. Rev. Lett.*, vol. 45, pp. 75–79, 1980.
- [14] R. Schnabel, “Squeezed states of light and their applications in laser interferometers,” arXiv:1611.03986v1 [quant-ph], 2016.
- [15] D. V. Martynov for the LIGO Scientific Collaboration, “Sensitivity of the Advanced LIGO detectors at the beginning of gravitational wave astronomy,” *Phys. Rev. D*, vol. 93, p. 112004, Jun 2016. [Online]. Available: <http://link.aps.org/doi/10.1103/PhysRevD.93.112004>
- [16] C. M. Caves, “Quantum-mechanical noise in an interferometer,” *Phys. Rev. D*, vol. 23, p. 1693, 1981.
- [17] The LIGO Scientific Collaboration, “A gravitational wave observatory operating beyond the quantum shot-noise limit,” *Nat. Phys.*, vol. 7, no. 12, pp. 962–965, Dec. 2011. [Online]. Available: <http://dx.doi.org/10.1038/nphys2083>
- [18] H. Grote, K. Danzmann, K. L. Dooley, R. Schnabel, J. Slutsky, and H. Vahlbruch, “First Long-Term Application of Squeezed States of Light in a Gravitational-Wave Observatory,” *Phys. Rev. Lett.*, vol. 110, p. 181101, May 2013. [Online]. Available: <http://link.aps.org/doi/10.1103/PhysRevLett.110.181101>
- [19] The LIGO Scientific Collaboration, “Enhanced sensitivity of the LIGO gravitational wave detector by using squeezed states of light,” *Nat. Phot.*, vol. 7, no. 8, pp. 613–619, Aug. 2013. [Online]. Available: <http://dx.doi.org/10.1038/nphoton.2013.177>
- [20] E. Oelker, L. Barsotti, S. Dwyer, D. Sigg, and N. Mavalvala, “Squeezed light for advanced gravitational wave detectors and beyond,” *Opt. Express*, vol. 22, no. 17, pp. 21 106–21 121, Aug 2014. [Online]. Available: <http://www.opticsexpress.org/abstract.cfm?URI=oe-22-17-21106>
- [21] The LIGO Scientific Collaboration, “Instrument science white paper,” 2015. [Online]. Available: <https://dcc.ligo.org/LIGO-T1400316/public>
- [22] “Einstein gravitational wave Telescope conceptual design study,” 2011. [Online]. Available: <https://tds.virgo-gw.eu/ql/?c=7954>
- [23] H. Billing, K. Maischberger, A. Rüdiger, R. Schilling, L. Schnupp, and L. Winkler, “An argon laser interferometer for the detection of gravitational radiation,” *J. Phys. E: Sci. Instrum.*, vol. 12, p. 1043, 1979.

- [24] S. Hild, “Beyond the First Generation: Extending the Science Range of the Gravitational Wave Detector GEO 600,” Ph.D. dissertation, University of Hannover, 2006.
- [25] M. Bassan, Ed., *Advanced Interferometers and the Search for Gravitational Waves*, ser. Astrophysics and Space Science Library. Springer International Publishing Switzerland, 2014, vol. 404.
- [26] D. J. Ottaway, P. Fritschel, and S. J. Waldman, “Impact of upconverted scattered light on advanced interferometric gravitational wave detectors,” *Opt. Express*, vol. 20, pp. 8329–8336, 2012.
- [27] R. Schilling, L. Schnupp, W. Winkler, H. Billing, K. Maischberger, and A. Rudiger, “A method to blot out scattered light effects and its application to a gravitational wave detector,” *Journal of Physics E: Scientific Instruments*, vol. 14, no. 1, p. 65, 1981. [Online]. Available: <http://stacks.iop.org/0022-3735/14/i=1/a=018>
- [28] H. Lück, J. Degallaix, H. Grote, M. Hewitson, S. Hild, B. Willke, and K. Danzmann, “Opto-mechanical frequency shifting of scattered light,” *Journal of Optics A: Pure and Applied Optics*, vol. 10, no. 8, p. 085004, 2008. [Online]. Available: <http://stacks.iop.org/1464-4258/10/i=8/a=085004>
- [29] I. Fiori et al., “Noise from scattered light in Virgo’s second science run data,” *Class. Quantum Gravity*, vol. 27, p. 194011, 2010.
- [30] B. Canuel, E. Genin, G. Vajente, and J. Marque, “Displacement noise from back scattering and specular reflection of input optics in advanced gravitational wave detectors,” *Opt. Express*, vol. 21, no. 9, pp. 10 546–10 562, May 2013. [Online]. Available: <http://www.opticsexpress.org/abstract.cfm?URI=oe-21-9-10546>
- [31] D. V. Martynov, “Lock Acquisition and Sensitivity Analysis of Advanced LIGO Interferometers,” Ph.D. dissertation, California Institute of Technology, 2015. [Online]. Available: <http://resolver.caltech.edu/CaltechTHESIS:05282015-142013480>
- [32] T. B. (for the LIGO Scientific Collaboration and the Virgo Collaboration), “A powerful veto for gravitational wave searches using data from Virgo’s first scientific run,” *Class. Quantum Grav.*, vol. 26, p. 204003, 2009.
- [33] S. Steinlechner, J. Bauchrowitz, M. Meinders, H. Müller-Ebhardt, K. Danzmann, and R. Schnabel, “Quantum-dense metrology,” *Nat. Phot.*, vol. 7, pp. 626–630, 2013.
- [34] M. Meinders, “Quantendichtes Ausleseverfahren zur Identifizierung von parasitären Interferenzen in einem Michelson-Interferometer,” Master’s thesis, Leibniz Universität Hannover, 2012.

- [35] S. Steinlechner, “Quantum metrology with squeezed and entangled light for the detection of gravitational waves,” Ph.D. dissertation, Leibniz Universität Hannover, 2013.
- [36] M. Meinders, S. Kroker, A. P. Singh, E.-B. Kley, A. Tünnermann, K. Danzmann, and R. Schnabel, “Cancellation of lateral displacement noise of three-port gratings for coupling light to cavities,” *Opt. Lett.*, vol. 40, no. 9, pp. 2053–2055, May 2015. [Online]. Available: <http://ol.osa.org/abstract.cfm?URI=ol-40-9-2053>
- [37] C. C. Gerry and P. L. Knight, *Introductory Quantum Optics*. Cambridge University Press, 2005.
- [38] A. Einstein, B. Podolsky, and N. Rosen, “Can Quantum-Mechanical Description of Physical Reality Be Considered Complete?” *Phys. Rev.*, vol. 47, p. 777, 1935.
- [39] E. Schrödinger, “Die gegenwärtige Situation in der Quantenmechanik,” *Naturwissenschaften*, vol. 23, pp. 807–812, 1935, 10.1007/BF01491891. [Online]. Available: <http://dx.doi.org/10.1007/BF01491891>
- [40] R. Horodecki, P. Horodecki, M. Horodecki, and K. Horodecki, “Quantum entanglement,” *Rev. Mod. Phys.*, vol. 81, pp. 865–942, Jun 2009. [Online]. Available: <http://link.aps.org/doi/10.1103/RevModPhys.81.865>
- [41] M. D. Reid, P. D. Drummond, W. P. Bowen, E. G. Cavalcanti, P. K. Lam, H. A. Bachor, U. L. Andersen, and G. Leuchs, “Colloquium : The Einstein-Podolsky-Rosen paradox: From concepts to applications,” *Rev. Mod. Phys.*, vol. 81, pp. 1727–1751, Dec 2009. [Online]. Available: <http://link.aps.org/doi/10.1103/RevModPhys.81.1727>
- [42] M. D. Reid, “Demonstration of the Einstein-Podolsky-Rosen paradox using nondegenerate parametric amplification,” *Phys. Rev. A*, vol. 40, pp. 913–923, Jul 1989. [Online]. Available: <http://link.aps.org/doi/10.1103/PhysRevA.40.913>
- [43] M. Ast, S. Steinlechner, and R. Schnabel, “Reduction of Classical Measurement Noise via Quantum-Dense Metrology,” *Phys. Rev. Lett.*, vol. 117, p. 180801, 2016. [Online]. Available: [arXiv:1607.00130](https://arxiv.org/abs/1607.00130)
- [44] S. Suzuki, H. Yonezawa, F. Kannari, M. Sasaki, and A. Furusawa, “7 dB quadrature squeezing at 860 nm with periodically poled KTiOPO,” *Applied Physics Letters*, vol. 89, no. 6, p. 061116, 2006. [Online]. Available: <http://scitation.aip.org/content/aip/journal/apl/89/6/10.1063/1.2335806>
- [45] A. Franzen, B. Hage, J. DiGuglielmo, J. Fiurášek, and R. Schnabel, “Experimental Demonstration of Continuous Variable Purification of Squeezed States,” *Phys. Rev. Lett.*, vol. 97, p. 150505, Oct 2006. [Online]. Available: <http://link.aps.org/doi/10.1103/PhysRevLett.97.150505>

- [46] S. Dwyer, L. Barsotti, S. S. Y. Chua, M. Evans, M. Factourovich, D. Gustafson, T. Isogai, K. Kawabe, A. Khalaidovski, P. Lam, M. Landry, N. Mavalvala, D. E. McClelland, G. D. Meadors, C. M. Mow-Lowry, R. Schnabel, R. M. S. Schofield, N. Smith-Lefebvre, M. Stefszky, C. Vorvick, and D. Sigg, “Squeezed quadrature fluctuations in a gravitational wave detector using squeezed light,” *Optics express*, vol. 21, no. 16, pp. 19 047–60, aug 2013. [Online]. Available: <http://www.ncbi.nlm.nih.gov/pubmed/23938820>
- [47] H. Vahlbruch, M. Mehmet, S. Chelkowski, B. Hage, A. Franzen, N. Lastzka, S. Goßler, K. Danzmann, and R. Schnabel, “Observation of Squeezed Light with 10 dB Quantum-Noise Reduction,” *Phys. Rev. Lett.*, vol. 100, p. 033602, 2008.
- [48] L. Schnupp, “Presentation at the European Collaboration Meeting on Interferometric Detection of Gravitational Waves,” Sorrent, 1988.
- [49] S. Steinlechner, J. Bauchrowitz, T. Eberle, and R. Schnabel, “Strong Einstein-Podolsky-Rosen steering with unconditional entangled states,” *Phys. Rev. A*, vol. 87, p. 022104, 2013.
- [50] J. Bauchrowitz, “Messung und graphische Darstellung von Ein- und Zwei-Modengequetschten Zuständen des Lichts,” Ph.D. dissertation, Leibniz Universität Hannover, 2013.
- [51] E. D. Black, “An introduction to Pound-Drever-Hall laser frequency stabilization,” *Am. J. Phys.*, vol. 69, no. 1, pp. 79–87, January 2001.
- [52] L.-A. Wu, H. J. Kimble, J. L. Hall, and H. Wu, “Generation of Squeezed States by Parametric Down Conversion,” *Phys. Rev. Lett.*, vol. 57, pp. 2520 – 2523, 1986.
- [53] L.-A. Wu, M. Xiao, and H. J. Kimble, “Squeezed states of light from an optical parametric oscillator,” *J. Opt. Soc. Am. B*, vol. 4, p. 1465, 1987.
- [54] J. A. Armstrong, “Interactions between light waves in a nonlinear dielectric,” *Phys. Rev.*, vol. 127, p. 1918, 1962.
- [55] M. M. Fejer, G. A. Magel, D. H. Jundt, and R. L. Byer, “Quasi-phase-matched second harmonic generation: Tuning and tolerances,” *IEEE J. Quantum Elect.*, vol. 28, pp. 2631–2654, 1992.
- [56] S. C. Kumar, G. K. Samanta, and M. Ebrahim-Zadeh, “High-power, single-frequency, continuous-wave second-harmonic-generation of ytterbium fiber laser in PPKTP and MgO:sPPLT,” *Opt. Express*, vol. 17, pp. 13 711–13 726, 2009.
- [57] H. Vahlbruch, S. Chelkowski, B. Hage, A. Franzen, K. Danzmann, and R. Schnabel, “Coherent Control of Vacuum Squeezing in the Gravitational-Wave Detection Band,” *Phys. Rev. Lett.*, vol. 97, p. 011101, 2006.

- [58] H. Vahlbruch, A. Khalaidovski, N. Lastzka, C. Gräf, K. Danzmann, and R. Schnabel, “The GEO 600 squeezed light source,” *Class. Quantum Grav.*, vol. 27, p. 084027, 2010.
- [59] M. Meinders and R. Schnabel, “Sensitivity improvement of a laser interferometer limited by inelastic back-scattering, employing dual readout,” *Class. Quantum Grav.*, vol. 32, p. 195004, 2015.
- [60] Simulated sound of binary neutron stars from the research group of Professor Scott A. Hughes at MIT. [Online]. Available: http://gmunu.mit.edu/sounds/comparable_sounds/comparable_sounds.html
- [61] H. J. Kimble, Y. Levin, A. B. Matsko, K. S. Thorne, and S. P. Vyatchanin, “Conversion of conventional gravitational-wave interferometers into quantum nondemolition interferometers by modifying their input and/or output optics,” *Phys. Rev. D*, vol. 65, p. 022002, Dec 2001. [Online]. Available: <http://link.aps.org/doi/10.1103/PhysRevD.65.022002>
- [62] P. Fritschel, M. Evans, and V. Frolov, “Balanced homodyne readout for quantum limited gravitational wave detectors,” *Opt. Express*, vol. 22, no. 4, pp. 4224–4234, Feb 2014. [Online]. Available: <http://www.opticsexpress.org/abstract.cfm?URI=oe-22-4-4224>
- [63] S. Steinlechner, B. W. Barr, A. S. Bell, S. L. Danilishin, A. Gläfke, C. Gräf, J. Hennig, E. A. Houston, S. H. Huttner, S. S. Leavey, D. Pascucci, B. Sorazu, A. Spencer, K. A. Strain, J. Wright, and S. Hild, “Local-oscillator noise coupling in balanced homodyne readout for advanced gravitational wave detectors,” *Phys. Rev. D*, vol. 92, p. 072009, Oct 2015.
- [64] K. X. Sun and R. L. Byer, “All-reflective Michelson, Sagnac, and Fabry-Perot interferometers based on grating beam splitters,” *Opt. Lett.*, vol. 23, pp. 567–569, 1997.
- [65] A. Bunkowski, O. Burmeister, P. Beyersdorf, K. Danzmann, and R. Schnabel, “Low-loss grating for coupling to a high-finesse cavity,” *Opt. Lett.*, vol. 29, p. 2342, 2004.
- [66] A. Bunkowski, O. Burmeister, K. Danzmann, and R. Schnabel, “Input-output relations for a 3-port grating coupled Fabry-Perot cavity,” *Opt. Lett.*, vol. 30, pp. 1183–1185, 2005.
- [67] T. Clausnitzer, E.-B. Kley, A. Tünnermann, A. Bunkowski, O. Burmeister, K. Danzmann, R. Schnabel, S. Gliech, and A. Duparré, “Ultra low-loss low-efficiency diffraction gratings,” *Opt. Express*, vol. 13, no. 12, pp. 4370–4378, 2005.
- [68] D. Friedrich, O. Burmeister, A. Bunkowski, T. Clausnitzer, S. Fahr, E.-B. Kley, A. Tünnermann, K. Danzmann, and R. Schnabel, “Diffractive beam splitter characterization via a power-recycled interferometer,” *Opt. Lett.*, vol. 33, pp. 101–103, 2008.

- [69] A. Bunkowski, O. Burmeister, T. Clausnitzer, E.-B. Kley, A. Tünnermann, K. Danzmann, and R. Schnabel, “Optical characterization of ultrahigh diffraction efficiency gratings,” *Appl. Opt.*, vol. 45, no. 23, pp. 5795–5799, 2006.
- [70] —, “Demonstration of three-port grating phase relations,” *Opt. Lett.*, vol. 31, no. 16, pp. 2384–2386, 2006.
- [71] O. Burmeister, M. Britzger, A. Thüring, D. F. F. Brückner, K. Danzmann, and R. Schnabel, “All-reflective coupling of two optical cavities with 3-port diffraction gratings,” *Optics Express*, vol. 18, pp. 9119–9132, 2010.
- [72] B. W. Barr, M. P. Edgar, J. Nelson, M. V. Plissi, S. H. Huttner, B. Sorazu, K. A. Strain, O. Burmeister, M. Britzger, D. Friedrich, R. Schnabel, K. Danzmann, J. Hallam, A. Freise, T. Clausnitzer, F. Brückner, E.-B. Kley, and A. Tünnermann, “Translational, rotational and vibrational coupling into phase in diffractively-coupled optical cavities,” *Opt. Lett.*, vol. 36, p. 2746, 2011.
- [73] M. Britzger, D. Friedrich, S. Kroker, F. Brückner, O. Burmeister, E. B. Kley, A. Tünnermann, K. Danzmann, and R. Schnabel, “Diffractively coupled Fabry-Perot resonator with power-recycling,” *Optics Express*, vol. 16, pp. 14964–14975, 2011.
- [74] M. Britzger, M. H. Wimmer, A. Khalaidovski, D. Friedrich, S. Kroker, F. Brückner, E.-B. Kley, A. Tünnermann, K. Danzmann, and R. Schnabel, “Michelson interferometer with diffractively-coupled arm resonators in second-order Littrow configuration,” *Opt. Exp.*, vol. 20, p. 25400, 2012.
- [75] *Concepts for Extending the Ultimate Sensitivity of Interferometric Gravitational Wave Detectors Using Non-Transmissive Optics with Diffractive or Holographic Coupling*, vol. -. Proceedings of the Seventh Marcel Grossman Meeting on recent developments in theoretical and experimental general relativity, gravitation, and relativistic field theories. Proceedings of the Meeting held at Stanford University, 24-30 July 1994, 1996.
- [76] S. Wise, V. Quetschke, A. J. Deshpande, G. Mueller, D. H. Reitze, D. B. Tanner, B. F. Whiting, Y. Chen, A. Tünnermann, E. Kley, and T. Clausnitzer, “Phase Effects in the Diffraction of Light: Beyond the Grating Equation,” *Phys. Rev. Lett.*, vol. 95, no. 1, p. 013901, 2005. [Online]. Available: <http://link.aps.org/abstract/PRL/v95/e013901>
- [77] A. Freise, A. Bunkowski, and R. Schnabel, “Phase and alignment noise in grating interferometers,” *New Journal of Physics*, vol. 9, p. 433, 2007.

Acknowledgments

I acknowledge support from the Deutsche Forschungsgemeinschaft (DFG) (Sonderforschungsbereich Transregio 7 and RTG1991) and from the International Max Planck Research School for Gravitational Wave Astronomy (IMPRS-GW).

Utilized Resources

Following programs were employed in this work: *Adobe Illustrator* and *Inkscape* with the *Component Library* by Alexander Franzen were used for schematic drawings of optical setups. *Matlab* was used for all plots and data analyses performed in this work. *LabView* was used for data acquisition and processing. *JamMT* by Nico Latzka was used for simulating optical beam paths. *Eagle* was used for designing electronic circuits. *FilterPro* was used for designing electronic filters. This document was generated using *MiKTeX* and the *TeXnicCenter* environment.

Curriculum Vitae

Name Melanie Ast, née Meinders
Address Hahnenstraße 6
30167 Hannover
E-mail melanie-ast@gmx.net
Born 14.01.1985 in Wittmund, Germany

Academic History

2015 - now Institute for laser physics, Universität Hamburg
Doctoral studies Physics

2012 - 2015 Institute for gravitational physics,
Gottfried Wilhelm Leibniz Universität Hannover
Doctoral studies in Physics

2011 - 2012 Institute for gravitational physics,
Gottfried Wilhelm Leibniz Universität Hannover
Diploma thesis in Physics:
“Quantendichtes Ausleseverfahren zur Identifizierung von
parasitären Interferenzen in einem Michelson-Interferometer”

2005 - 2011 Gottfried Wilhelm Leibniz Universität Hannover
Diploma studies in Physics

1997 - 2004 Alexander-von-Humboldt-Schule, Wittmund
Higher education entrance qualification (Abitur)

List of Publications

- [1] M. Ast, S. Steinlechner, and R. Schnabel, “Reduction of classical measurement noise via quantum-dense metrology,” *Physical Review Letters*, vol. 117, no. 18, p. 180801, 2016.
- [2] M. Meinders and R. Schnabel, “Sensitivity improvement of a laser interferometer limited by inelastic back-scattering, employing dual readout,” *Classical and Quantum Gravity*, vol. 32, no. 19, p. 195004, 2015.
- [3] M. Meinders, S. Kroker, A. P. Singh, E.-B. Kley, A. Tünnermann, K. Danzmann, and R. Schnabel, “Cancellation of lateral displacement noise of three-port gratings for coupling light to cavities,” *Optics Letters*, vol. 40, no. 9, pp. 2053–2055, 2015.
- [4] S. Ast, M. Ast, M. Mehmet, and R. Schnabel, “Gaussian entanglement distribution with gigahertz bandwidth,” *Optics Letters*, vol. 41, no. 21, pp. 5094–5097, 2016.
- [5] S. Steinlechner, J. Bauchrowitz, M. Meinders, H. Müller-Ebhardt, K. Danzmann, and R. Schnabel, “Quantum-dense metrology,” *Nature Photonics*, vol. 7, no. 8, pp. 626–630, 2013.

Publications as a member of the LIGO Scientific Collaboration

(More than 1000 co-authors)

- [6] B. Abbott,..., M. Ast,..., “Observation of gravitational waves from a binary black hole merger,” *Physical Review Letters*, vol. 116, no. 6, p. 061102, 2016.
- [7] B. Abbott,..., M. Ast,..., “GW151226: Observation of gravitational waves from a 22-solar-mass binary black hole coalescence,” *Physical Review Letters*, vol. 116, no. 24, p. 241103, 2016.
- [8] B. Abbott,..., M. Ast,..., “Astrophysical implications of the binary black hole merger GW150914,” *The Astrophysical Journal Letters*, vol. 818, no. 2, p. L22, 2016.
- [9] B. Abbott,..., M. Ast,..., “Localization and broadband follow-up of the gravitational-wave transient GW150914,” arXiv preprint arXiv:1602.08492, 2016.
- [10] B. Abbott,..., M. Ast,..., “GW150914: The Advanced LIGO Detectors in the Era of First Discoveries,” *Physical Review Letters*, vol. 116, no. 13, p. 131103, 2016.

- [11] B. Abbott,..., M. Ast,..., “GW150914: Implications for the stochastic gravitational-wave background from binary black holes,” *Physical Review Letters*, vol. 116, no. 13, p. 131102, 2016.
- [12] B. Abbott,..., M. Ast,..., “Binary black hole mergers in the first Advanced LIGO observing run,” *Physical Review X*, vol. 6, no. 4, p. 041015, 2016.
- [13] B. Abbott,..., M. Ast,..., “The rate of binary black hole mergers inferred from Advanced LIGO observations surrounding GW150914,” arXiv preprint arXiv:1602.03842, 2016.
- [14] B. Abbott,..., M. Ast,..., “GW150914: First results from the search for binary black hole coalescence with Advanced LIGO,” *Physical Review D*, vol. 93, no. 12, p. 122003, 2016.
- [15] B. Abbott,..., M. Ast,..., “Characterization of transient noise in Advanced LIGO relevant to gravitational wave signal GW150914,” *Classical and Quantum Gravity*, vol. 33, no. 13, p. 134001, 2016.
- [16] B. Abbott,..., M. Ast,..., “Observing gravitational-wave transient GW150914 with minimal assumptions,” *Physical Review D*, vol. 93, no. 12, p. 122004, 2016.
- [17] B. Abbott,..., M. Ast,..., “An improved analysis of GW150914 using a fully spin-precessing waveform model,” arXiv preprint arXiv:1606.01210, 2016.
- [18] B. Abbott,..., M. Ast,..., “All-sky search for long-duration gravitational wave transients with initial LIGO,” *Physical Review D*, vol. 93, no. 4, p. 042005, 2016.
- [19] B. Abbott,..., M. Ast,..., “Upper limits on the rates of binary neutron star and neutron-star-black-hole mergers from Advanced LIGO’s first observing run,” arXiv preprint arXiv:1607.07456, 2016.
- [20] B. Abbott,..., M. Ast,..., “The basic physics of the binary black hole merger GW150914,” *Annalen der Physik*, 2016.
- [21] B. Abbott,..., M. Ast,..., “Tests of General Relativity with GW150914,” *Physical Review Letters*, vol. 116, no. 22, p. 221101, 2016.
- [22] B. Abbott,..., M. Ast,..., “Comprehensive All-sky Search for Periodic Gravitational Waves in the Sixth Science Run LIGO Data,” arXiv preprint arXiv:1605.03233, 2016.
- [23] B. Abbott,..., M. Ast,..., “Search for transient gravitational waves in coincidence with short duration radio transients during 2007-2013,” arXiv preprint arXiv:1605.01707, 2016.
- [24] B. Abbott,..., M. Ast,..., “Directly comparing GW150914 with numerical solutions of Einstein’s equations for binary black hole coalescence,” arXiv preprint arXiv:1606.01262, 2016.

- [25] B. Abbott,..., M. Ast,..., “Supplement: The Rate of Binary Black Hole Mergers Inferred from Advanced LIGO Observations Surrounding GW150914,” arXiv preprint arXiv:1606.03939, 2016.
- [26] B. Abbott,..., M. Ast,..., “Exploring the Sensitivity of Next Generation Gravitational Wave Detectors,” arXiv preprint arXiv:1607.08697, 2016.
- [27] B. Abbott,..., M. Ast,..., “A First Targeted Search for Gravitational-Wave Bursts from Core-Collapse Supernovae in Data of First-Generation Laser Interferometer Detectors,” arXiv preprint arXiv:1605.01785, 2016.
- [28] J. Aasi,..., M. Ast,..., “Search of the Orion spur for continuous gravitational waves using a loosely coherent algorithm on data from LIGO interferometers,” *Physical Review D*, vol. 93, no. 4, p. 042006, 2016.
- [29] J. Aasi,..., M. Meinders,..., “First low frequency all-sky search for continuous gravitational wave signals,” *Physical Review D*, vol. 93, no. 4, p. 042007, 2016.
- [30] J. Aasi,..., M. Meinders,..., “Advanced LIGO,” *Classical and Quantum Gravity*, vol. 32, no. 7, p. 074001, 2015.
- [31] J. Aasi,..., M. Meinders,..., “Searches for continuous gravitational waves from nine young supernova remnants,” *The Astrophysical Journal*, vol. 813, no. 1, p. 39, 2015.
- [32] J. Aasi,..., M. Meinders,..., “Directed search for gravitational waves from Scorpius X-1 with initial LIGO data,” *Physical Review D*, vol. 91, no. 6, p. 062008, 2015.
- [33] J. Aasi,..., M. Meinders,..., “Narrow-band search of continuous gravitational-wave signals from Crab and Vela pulsars in Virgo VSR4 data,” *Physical Review D*, vol. 91, no. 2, p. 022004, 2015.
- [34] J. Aasi,..., M. Meinders,..., “Improved upper limits on the stochastic gravitational-wave background from 2009–2010 Ligo and Virgo data,” *Physical Review Letters*, vol. 113, no. 23, p. 231101, 2014.
- [35] J. Aasi,..., M. Meinders,..., “Implementation of an-statistic all-sky search for continuous gravitational waves in Virgo VSR1 data,” *Classical and Quantum Gravity*, vol. 31, no. 16, p. 165014, 2014.
- [36] J. Aasi,..., M. Meinders,..., “The NINJA-2 project: detecting and characterizing gravitational waveforms modelled using numerical binary black hole simulations,” *Classical and Quantum Gravity*, vol. 31, no. 11, p. 115004, 2014.
- [37] J. Aasi,..., M. Meinders,..., “First all-sky search for continuous gravitational waves from unknown sources in binary systems,” *Physical Review D*, vol. 90, no. 6, p. 062010, 2014.

- [38] J. Aasi,..., M. Meinders,..., “Search for gravitational waves associated with γ -ray bursts detected by the interplanetary network,” *Physical Review Letters*, vol. 113, no. 1, p. 011102, 2014.
- [39] J. Aasi,..., M. Meinders,..., “Search for gravitational wave ringdowns from perturbed intermediate mass black holes in LIGO-Virgo data from 2005–2010,” *Physical Review D*, vol. 89, no. 10, p. 102006, 2014.
- [40] J. Aasi,..., M. Meinders,..., “Search for gravitational radiation from intermediate mass black hole binaries in data from the second LIGO-Virgo joint science run,” *Physical Review D*, vol. 89, no. 12, p. 122003, 2014.
- [41] J. Aasi,..., M. Meinders,..., “Methods and results of a search for gravitational waves associated with gamma-ray bursts using the GEO 600, LIGO, and Virgo detectors,” *Physical Review D*, vol. 89, no. 12, p. 122004, 2014.
- [42] M. Aartsen,..., M. Meinders,..., “Multimessenger search for sources of gravitational waves and high-energy neutrinos: Initial results for LIGO-Virgo and IceCube,” *Physical Review D*, vol. 90, no. 10, p. 102002, 2014.
- [43] F. Acernese,..., M. Meinders,..., “Concepts and research for future detectors,” *General Relativity and Gravitation*, vol. 46, no. 5, pp. 1–20, 2014.